The Precision of the Tracking System in Search of Solar Axions

Julia Vogel

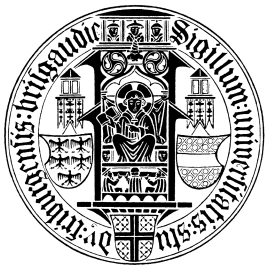

Fakultät für Mathematik und Physik
Albert-Ludwigs-Universität Freiburg

The Precision of the Tracking System in Search of Solar Axions

Diplomarbeit
vorgelegt
von
Julia Vogel

Fakultät für Mathematik und Physik
Albert-Ludwigs-Universität
Freiburg im Breisgau

Dezember 2005

Zusammenfassung

Die Quantenchromodynamik (QCD) konfrontiert die Physiker mit überraschenden Fragen. Nachdem Experimente bestätigen konnten, dass die CP-Symmetrie in der elektroschwachen Theorie, nämlich beim Zerfall des neutralen Kaons, verletzt ist, wurde dies auch von der QCD erwartet. Aber bis heute gibt es dafür keine experimentelle Bestätigung. Verbunden mit diesem sogenannten CP-Problem ist ein (noch) hypothetisches Teilchen: das Axion.
Falls es existiert, könnten Axionen sowohl im frühen Universum entstanden sein als auch noch heutzutage im Kern von Sternen wie unserer Sonne produziert werden. Reliktaxionen aus dem frühen Universum sind ein vielversprechender Kandidat für die Dunkle Materie, die 20-30% der Dichte unseres Universums ausmacht.

Nachdem mit Hilfe der Astrophysik und der Kosmologie der Massenbereich, in dem Axionen existieren können, auf ein Fenster von μeV bis zu einigen zehn meV eingeschränkt werden konnte, haben mehrere Experimente versucht, Axionen nachzuweisen. Verschiedene Methoden wurden auf der Jagd nach dem Axion angewendet; die meisten machen sich den sogenannten Primakoff-Effekt zunutze, der eine Umwandlung von Axionen zu Photonen in Gegenwart von starken elektromagnetischen Feldern ermöglicht. Diesen Effekt nutzen zum Beispiel die Helioskope zum Nachweis von Axionen, die in unserer Sonne produziert werden.

Das CERN Axion Solar Telescope (CAST) der Europäischen Organisation für Kernforschung CERN (Conseil Européen pour la Recherche Nucléaire) in Genf ist eines dieser Helioskope. Es benutzt einen Prototypmagneten des neuen Beschleunigers und Speicherrings am CERN (Large Hadron Collider, LHC). Der supraleitende Magnet ist auf einer beweglichen Plattform befestigt und kann somit der Sonne jeden Tag für etwa 2×90 Minuten folgen.
Das Experiment verfügt über drei verschiedenen Röntgendetektoren: eine Zeitprojektionskammer (Time Projection Chamber, TPC), einen MICROMEGAS-Detektor (MICROMEsh GAseous Structure) und einen CCD-Detektor (Charge Coupled Device). Mit jedem Detektor versucht man entweder morgens oder abends (je nach Position am Experiment) Photonen, die aus dem Primakoff-Effekt resultieren, nachzuweisen.

Da die meisten Axionen im Kern der Sonne (10-20% des Sonnendurchmessers) produziert werden, ist eine hohe Präzision der Nachführung des Magneten unerläßlich. Eine speziell dafür entwickelte Software (Tracking Mode) steuert den über 40 Tonnen schweren Aufbau derart, dass er der wahren Position der Sonne so exakt wie möglich folgt. Die Abweichung soll zu jeder Zeit weniger als 0.02° betragen.
Zweimal im Jahr ist eine optische Überprüfung des solaren Trackings möglich, indem man die Sonne durch ein Fenster beim Experiment direkt beobachtet. Dazu wird eine Kamera parallel zur Magnetachse ausrichtet und die Sonne während der Nachführung gefilmt. Ein zusätzliches Programm (Filming Mode) berechnet die Refraktion der Photonen in der Erdatmosphäre und richtet den Magneten auf die scheinbaren Koordinaten der Sonne aus.

Diese Arbeit beschreibt die Verbesserung eines existierenden Systems für das Filmen der Sonne mit dem Ziel, die Präzision der optischen Überprüfung des solaren Trackings so zu erhöhen, dass sie der Genauigkeit des Nachführens entspricht und somit beweiskräftige Aussagen möglich werden, ob und wie genau der CAST-Magnet auf das Zentrum der Sonne gerichtet ist.

Im März 2005 wurde ein neuer Aufbau getestet und erste Aufnahmen der Sonne gemacht. Die Auflösung der verwendeten CCD-Kamera war wesentlich höher als die der bis dahin benutzten Webcam. Für September 2005 wurde zusätzlich ein stabilerer und gleichzeitig flexiblerer Aufbau verwendet. Die Stabilität war erforderlich, um Vibrationen zu dämpfen, während die Beweglichkeit die Ausrichtung des Aufbaus mit der Magnetachse vereinfacht. Nicht nur der Aufbau, sondern auch die Analyse der Bilder wurde für Herbst 2005 verbessert und weitgehend automatisiert.

Die Analyse der erhaltenen Daten im Frühjahr ergab, dass der Magnet im Rahmen einer Genauigkeit der Ordnung 0.03° auf den Kern der Sonne zeigte. Dabei betrug die Abweichung der Magnetausrichtung vom Sonnenzentrum in x- und y-Richtung (gewählt in Richtung der Sonnenbewegung):

$$\begin{aligned}\bar{x}_{\text{Spring 2005}} &= -0.018^\circ \pm 0.002^\circ(\text{stat.}) \pm 0.026^\circ(\text{syst.}),\\ \bar{y}_{\text{Spring 2005}} &= -0.020^\circ \pm 0.001^\circ(\text{stat.}) \pm 0.028^\circ(\text{syst.}).\end{aligned}$$

Für September 2005 wurde die Präzision weiter verbessert und die Sonne konnte erneut gefilmt werden. Auch diese Bilder ergaben, dass der CAST-Magnet mit einer Genauigkeit von nun bis zu 0.02° auf das solare Zentrum ausgerichtet war. Diese Genauigkeit entspricht der Präzision, die für die Nachführung des Magneten gefordert wird. Die Abweichungen der Magnetausrichtung vom Sonnenzentrum für die ersten beiden Tage des Filmens im September waren in x- und y-Richtung:

$$\begin{aligned}\bar{x}_{23.9.05} &= -0.026^\circ \pm 0.001^\circ(\text{stat.}) \pm 0.080^\circ(\text{syst.}),\\ \bar{y}_{23.9.05} &= -0.011^\circ \pm 0.001^\circ(\text{stat.}) \pm 0.027^\circ(\text{syst.});\end{aligned}$$

$$\begin{aligned}\bar{x}_{24.9.05} &= -0.020^\circ \pm 0.001^\circ(\text{stat.}) \pm 0.030^\circ(\text{syst.}),\\ \bar{y}_{24.9.05} &= -0.027^\circ \pm 0.001^\circ(\text{stat.}) \pm 0.023^\circ(\text{syst.}).\end{aligned}$$

Für den dritten Tag mussten mehrere Bilder überlagert werden, weil Äste eine freie Sicht auf die Sonne verhinderten. Das Ergebnis dieser Analyse läßt sich zusammenfassen als:

$$\begin{aligned}x_{28.9.05} &= -0.014^\circ \pm 0.019^\circ(\text{syst.}),\\ y_{28.9.05} &= -0.004^\circ \pm 0.019^\circ(\text{syst.}).\end{aligned}$$

Somit ist der CAST-Magnet innerhalb der Präzision des Filmens, die vergleichbar mit der Genauigkeit der Nachführung ist, auf den Sonnenmittelpunkt ausgerichtet. Allerdings deuten alle Daten darauf hin, dass der Magnet etwas zu hoch und zu weit nach rechts zeigt, und somit der Sonne um ungefähr 10 s im Tracking voraus ist. Diese Diskrepanz der Ordnung 0.02° liegt jedoch innerhalb der Fehler des Filmens.

Contents

Chapter 1

Introduction

> In physics, you don't have to go around making trouble for yourself - nature does it for you.
>
> **Frank Wilczek**, Winner of the Nobel Prize in Physics 2004.

Quantum Chromodynamics (QCD), the theory of strong interactions, confronts physicists with puzzling questions. This theory is expected to violate the so-called Charge-Parity-Symmetry (CP-Symmetry). For physical laws, C-Symmetry is a symmetry under charge-conjugation transformation, while P-Symmetry refers to parity transformations. A combination of both was initially expected to be conserved, but it was found to be violated in the Kaon decay [1]. Thus the electroweak theory violates CP-Symmetry, and also QCD was expected to do so, but up to now no experiment was able to observe the non-conservation of the CP-Symmetry in QCD. This so-called CP-Problem is where the axion, a still hypothetical particle, comes into play:
R. Peccei and H. Quinn formulated a solution to explain CP-conservation by introducing an additional symmetry, the Peccei-Quinn-Symmetry. When it is spontaneously broken, the resulting particle is an axion, which obtained its name by F. Wilczek, who always thought, probably with a smile, that this name - originally a washing powder brand - sounded like a great name for an elementary particle [2].

If they exist, axions could have been created in the very early universe. But they can as well originate from cores of stars like our Sun nowadays. As survivors produced after the Big Bang, they are a promising candidate to contribute to the Dark Matter, which accounts for 20-30% of the density of the universe.
In order to prove or rule out the existence of the axion, several constraints from astrophysics and cosmology have been applied. Like this, the mass range, in which axions are still likely to exist, could be narrowed down to a window reaching from μeV up to some meV. In several experiments, it has been attempted to detect axions in and close to the remaining mass regions. Different methods have been applied in the quest for the postulated particle. Most of them, however, make use of the so-called Primakoff effect, which allows for a conversion

of axions into photons in the presence of a strong electromagnetic field. One possible kind of experiment employing this effect are the helioscopes, waiting for axions produced in the closest axion source available: the core of the Sun.

The CERN Axion Solar Telescope (CAST) of the European Organization for Nuclear Research CERN (Conseil Européen pour la Recherche Nucléaire) in Geneva, Switzerland, is one of these helioscopes. It utilizes a prototype of the Large Hadron Collider (LHC) magnets with a length of 9.26 m and a magnetic field of up to 9 T. Since it is mounted on a movable platform, the CAST magnet is able to follow the Sun for about 90 minutes during sunrise and sunset each day.
In this experiment three different X-ray detectors are used. A Time Projection Chamber (TPC) is waiting for the appearance of photons from axion-to-photon conversion arriving during sunset, while in the morning a MICROMEGAS (MICROMEsh GAseous Structure) detector and a Charge Coupled Device (CCD) are used to prove the appearance of an axion by detecting an X-ray photon. Between the magnet and the CCD, an X-ray focussing device is installed. It was originally designed for the German X-ray satellite mission ABRIXAS and it is able to improve the signal-to-background ratio by a factor of about 200.
Since most of the axions produced inside the Sun are expected to emerge from its core, a high precision of the solar tracking is essential. A software, especially designed to guide the magnet to follow the Sun with a deviation of less than 0.02° at any time of tracking, is used to accomplish this.
Twice a year, it is possible to observe directly the Sun through a window in the experimental area and thus perform an optical crosscheck of the tracking system. By using a camera aligned with the magnet axis and an additional routine of the tracking software, the so-called filming mode, the Sun can be filmed during tracking. The filming mode program calculates the refraction of photons coming from the Sun in the atmosphere of the Earth and adds the necessary correction to the usual tracking coordinates, thus directing the magnet to point at the apparent position of the Sun.

This work describes the improvement of the system for the solar filming in order to reach a precision of this optical crosscheck, which is of the order of the tracking accuracy, such that conclusive statements can be provided on whether and how exactly CAST is actually pointing to the Sun.
Chapter 2 will provide an introduction to general axion theory, including the theoretical background of its postulation, properties axions are supposed to have, the limits that can be put on its mass and coupling constant by astrophysics and cosmology as well as possible ways to detect the postulated particles. In Chapter 3, a closer look at axions coming from the Sun and their detection in magnetic fields will be taken. Following this, the CAST experiment is presented in more detail in Chapter 4. The improvements of the system to film the Sun as well as its first application in Spring 2005 and the analysis of the obtained images of the Sun can be found in Chapter 5. After this first filming, a further enhanced filming setup was applied again in Fall 2005. Chapter 6 provides all necessary information on this optical crosscheck of the tracking system in September. Finally, in Chapter 7, the results are compiled and a brief outlook is provided.

Chapter 2

The Axion

In order to provide an overview on general axion physics, this chapter will introduce the problems of Quantum Chromodynamics which led to the postulation of the axion. Secondly, the properties of this hypothetical particle will be discussed and different axion models will be presented. Furthermore, cosmological and astrophysical considerations, which are able to narrow the mass ranges in which axions could still exist, will be looked at. It goes without saying that not only these considerations put limits on the mass and the coupling constant of the particle looked for so eagerly, but also experimental searches are on their way, trying to push the existing bounds further and eventually prove or exclude the existence of the axion.

2.1 The Strong CP-Problem

Quantum Chromodynamics (QCD), the theory of strong interactions, is a non-Abelian field theory. It is constructed to be both asymptotically free and confining. Hence, exact solutions are very unlikely to exist. Gluons, the gauge bosons of QCD, carry color charge themselves and thus, they can interact with each other. This is important for the theory, but it actually complicates solving field equations immensely. In Quantum Electrodynamics (QED), which is an Abelian theory, things are different, since the photons (gauge bosons of QED) do not carry electric charges.
A perplexing question in particle physics, the so-called strong Charge-Parity-Problem (CP-Problem), is, why QCD does not seem to break the CP-Symmetry[1]. It is expected to be violated, as it is in the electroweak theory, but nevertheless, no effect like that has ever been observed in any experiment so far. As will be discussed in the following, the strong CP-problem originates from the attempt to solve the $U(1)_A$-Problem of perturbative QCD. A possible and, indeed, very elegant solution to the question of CP-Conservation can be derived from the Peccei-Quinn mechanism.

[1] C-Symmetry is a symmetry under charge-conjugation transformation, i.e. inversion of quantum charges, while P-Symmetry refers to parity transformations, i.e. the change of sign in all spatial coordinates.

2.1.1 The $U(1)_A$-Problem

Characteristically, solutions in QCD are obtained by expanding the fields around the ground state (i.e. the vacuum). The Lagrangian density of this perturbative QCD can be written as

$$\mathcal{L}_{\text{pert}} = \sum_f \bar{q}_f \left(\gamma^\mu i D_\mu - m_f\right) q_f - \frac{1}{4} G^a_{\mu\nu} G^{\mu\nu}_a, \tag{2.1}$$

where f is the quark flavor and q_f denotes the quark fields. G represents the gluon field tensor. In Ref. [4] further details are provided.

QCD can only be described approximatively by $\mathcal{L}_{\text{pert}}$, although it is good enough for perturbative calculations. The reason for this insufficiency is that $\mathcal{L}_{\text{pert}}$ is not only invariant under global vectorial transformations, but also under axial ones. QCD, however, does not show this axial symmetry, known as $U(1)_A$. If it did so, this would lead to hadronic parity doublets, indicating a spontaneous symmetry breaking (SSB) of $U(1)_A$ [5].
If a symmetry is spontaneously broken, this means that the Lagranian of a system has a certain symmetry, but the ground state (i.e. the vacuum) does not. In Lagrangian theories, SSB is a frequent phenomenon. Whenever the symmetry which is broken is a continuous global one, a Nambu-Goldstone boson, i.e. a massless spin-zero boson corresponding to the remaining symmetry, appears. However, if the symmetry is not exact, the particle will have a small mass and it is called a Pseudo-Goldstone boson.
Of the four expected Goldstone bosons for a possible $U(1)_A$-Symmetry breaking of QCD, only three have been observed, namely π^-, π^0, π^+. The only particle which could take the place of the fourth boson[2] is η'. It has the correct quantum numbers ($J^P = 0^-$), but is indeed too heavy[3]. Therefore, one faces the $U(1)_A$-Problem, also called the η-mass problem: the non-existence of the fourth boson.

2.1.2 The Solution of the $U(1)_A$-Problem

By postulating the anomalous breaking of the $U(1)_A$-Symmetry, t'Hooft solved the $U(1)_A$-Problem [9, 10]. Anomalous means that a symmetry is not a true one, i.e. it is broken by quantum effects. In the case of $U(1)_A$, the anomaly is known as axial or Adler-Bell-Jackiw (ABJ) anomaly and it adds a term $\mathcal{L}_\Theta$ to the Lagrangian of QCD:

$$\mathcal{L}_\Theta = \Theta \frac{g^2}{32\pi^2} G^{\mu\nu}_a \tilde{G}^a_{\mu\nu} \tag{2.2}$$

with the coupling constant g and $\tilde{G}^a_{\mu\nu}$ the dual of the gluon field strength tensor.
$\mathcal{L}_\Theta$ exists due to the complicated structure of the ground state (i.e. the vacuum) in non-Abelian field theories like QCD. An infinite number of degenerated vacuum states forms the ground state and it is impossible to transform the vacua from one into the other by using continuous transformations (see Ref. [11] and references therein). To characterize

[2] The pion should have a light partner corresponding to a flavor singlet. This would be η' (not η), since $|\eta'\rangle \approx |\eta_1\rangle = \frac{1}{\sqrt{3}} \left\{ \left|u^\uparrow \bar{u}^\downarrow\right\rangle + \left|d^\uparrow \bar{d}^\downarrow\right\rangle + \left|s^\uparrow \bar{s}^\downarrow\right\rangle \right\}$ [6, 7].

[3] Its mass is $m_{\eta'} = 958$ MeV, which is large compared to the pion mass $m_\pi = 135$ MeV [8].

the distinct vacua, an integer is used, the winding number n. The ground state can be expressed as a superposition of the degenerate vacua[4], the so-called Θ-vacuum:

$$|\Theta\rangle = \sum_{n=-\infty}^{\infty} e^{-in\Theta} |n\rangle , \tag{2.3}$$

where $0 \leq \Theta \leq 2\pi$.

For the Standard Model, in order to consider also electroweak interactions, Θ has to be substituted by $\bar{\Theta}$, which is given as

$$\bar{\Theta} = \Theta + \arg(\det \mathrm{M}). \tag{2.4}$$

Here, M is the quark mass matrix. The resulting equation for the additional Lagrangian term accordingly reads then:

$$\mathcal{L}_{\bar{\Theta}} = \bar{\Theta} \frac{g^2}{32\pi^2} G_a^{\mu\nu} \tilde{G}^a_{\mu\nu}. \tag{2.5}$$

A more detailed discussion can be found, for example, in Refs. [12, 13].

2.1.3 The Strong CP-Problem

The $U(1)_A$-Problem can thus be solved, but at the expense of raising a new problem. $\mathcal{L}_{\bar{\Theta}}$ violates CP-Symmetry. No strong CP-Problem would appear, if at least one quark was massless[5]. But since this is not the case, the two terms forming $\bar{\Theta}$ (see Equation (2.4)) are independent. Thus, there is no reason, why they would have to cancel out. This yields to a value for the electric dipole moment of the neutron of

$$d_n \approx 5 \times 10^{-16} \bar{\Theta} \text{ e cm} \tag{2.6}$$

according to Ref. [14], while the experimental limit is [15, 16]:

$$|d_n| < 12 \times 10^{-26} \text{ e cm}. \tag{2.7}$$

This in turn implies $\bar{\Theta} \leq 10^{-10}$ or even zero, which would require fine-tuning between the two summands forming $\bar{\Theta}$. The question, why $\bar{\Theta}$ is so small, is called the *strong CP-Problem.*

2.1.4 The Peccei-Quinn Solution

Peccei and Quinn (PQ) suggested an elegant, and actually the most promising solution to answer the question about the smallness of $\bar{\Theta}$ [17]. Since fine-tuning often implies that there are additional symmetries in a theory, they introduced a global, chiral Peccei-Quinn-Symmetry $U_{PQ}(1)$, and like this, the possibility to have $\bar{\Theta} = 0$ is given. $U_{PQ}(1)$ is a spontaneously broken symmetry. Since it is not an exact symmetry, however, a Pseudo-Goldstone boson is obtained, as both Weinberg and Wilczek pointed out independently [18, 19]. This resulting particle obtained the name *axion*[6]. The mass of the axion m_a is inversely propor-

[4] For this, tunneling solutions (such as instantons) between the degenerate vacua must exist [5].

[5] The $\bar{\Theta}$-term could be made to vanish by an axial transformation of the quark fields under these circumstances [11].

[6] Actually, F. Wilczek named the new particles "after a laundry detergent, since they clean up a problem with an axial current" [20].

tional to the scale of the broken Peccei-Quinn-Symmetry, f_a, due to the chiral anomaly. f_a is sometimes also referred to as the axion decay constant. The additional field will therefore append another term, depending linearly on the field a added to the Lagrangian (since the axion couples to gluons), leading to

$$\mathcal{L}_{\text{Axion}} = \mathcal{L}_{\text{kin}} + \mathcal{L}_{\text{int}} + C_a \frac{a}{f_a} \frac{g^2}{32\pi^2} G_a^{\mu\nu} \tilde{G}_{a\mu\nu}, \tag{2.8}$$

where C_a is a model dependent parameter. The first term represents the kinetic energy and is given by $\mathcal{L}_{\text{kin}} = -\frac{1}{2}\partial_\mu a \partial^\mu a$, the second term takes further interactions of the axion (such as with fermions) into consideration, while the third summand gives the axion field an effective potential. Since this last term as well as $\mathcal{L}_\Theta$ contribute to the axion field, it is possible to minimize it, which leads to

$$\langle a \rangle = -\frac{f_a}{C_a} \bar{\Theta}. \tag{2.9}$$

By introducing an additional axion field a, it is possible to cancel the disturbing $\bar{\Theta}$-term in the QCD Lagrangian: no violation occurs and consequently the strong CP-Problem is solved[7]. However, one practical problem remains: the detection of the axion, which has not been accomplished so far.

2.2 The Axion and its Properties

All the important axion properties and couplings depend on the breaking scale of the Peccei-Quinn-Symmetry, f_a. The proportionality of the various axion coupling constants g_{ai} to the axion mass m_a or to the inverse of the axion decay constant f_a, which is equivalent, are characteristic:

$$g_{ai} \propto m_a \tag{2.10}$$

$$g_{ai} \propto \frac{1}{f_a} \tag{2.11}$$

where i denotes the particle the axion couples to[8]. The appearance (or non-appearance) of certain couplings distinguishes the different existing axion models, which will be discussed below (see Sect. 2.2.2) in more detail.

2.2.1 Axion Couplings

Axions interact with fundamental bosons, such as gluons and photons, as well as with fermion like electrons and nucleons. These couplings form the term $\mathcal{L}_{\text{int}}$ in Equation (2.8).

[7] For completeness, it should be mentioned that alternative suggestions to solve the strong CP-Problem exist. An approach to do so by using supersymmetry can be found in Ref. [21].

[8] Sometimes g_{ai} is also denoted as g_{aii} in order to describe the coupling in a more accurate way.

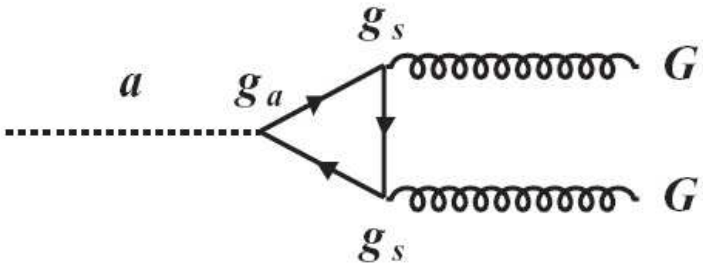

Figure 2.1: Feynman diagram of the axion-to-gluon coupling. g_s is the strong coupling constant, while g_a denotes the axion-to-fermion coupling constant (figure taken from Ref. [3]).

Interactions of Axions with Fundamental Bosons

Coupling to Gluons Due to the chiral anomaly, axions couple to gluons as mentioned above (see Fig. 2.1) , leading to

$$\mathcal{L}_{aG} = \frac{\alpha_s}{8\pi f_a} a G_a^{\mu\nu} \tilde{G}_{a\mu\nu}, \tag{2.12}$$

where α_s is the fine structure constant of strong interactions. This coupling is the feature that distinguishes axions from other pseudoscalar particles, since it follows directly from every axion model. Through the coupling to gluons, axions acquire a mass, which can be obtained from the mixing with pions approximately as [22, 23]:

$$m_a = \frac{m_\pi f_\pi}{f_a} \left(\frac{z}{(1+z+w)(1+z)} \right)^{1/2} \simeq 0.60 \text{ eV} \frac{10^7 \text{ GeV}}{\text{f}_\text{a}}, \tag{2.13}$$

where the pion mass is $m_\pi = 135$ MeV and its decay constant is given by $f_\pi = 93$ MeV. Here, z and w are the quark mass ratios [24]

$$z \equiv \frac{m_u}{m_d} = 0.568 \pm 0.042, \tag{2.14}$$

$$w \equiv \frac{m_u}{m_s} = 0.0290 \pm 0.0043. \tag{2.15}$$

There is a significant variation in the value of z: according to Ref. [8] z is between 0.3 and 0.7, while Ref. [26] gives $z = 0.553 \pm 0.043$.

Coupling to Photons Since, as a result of axion-gluon coupling, axions mix with pions, they also interact with photons [22]. Furthermore, the axion can couple to two photons (triangle loop), if the quarks and leptons carry both PQ charges and electric charges (see Fig. 2.2). This happens in the same way as does the axion-gluon coupling (see Fig. 2.1). The Lagrangian of the interaction can be written as

$$\mathcal{L}_{a\gamma} = -\frac{g_{a\gamma}}{4} F_{\mu\nu} \tilde{F}^{\mu\nu} a = g_{a\gamma} \vec{E} \cdot \vec{B} a, \tag{2.16}$$

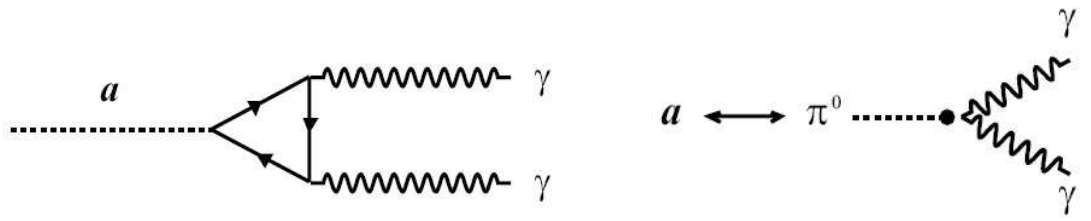

Figure 2.2: Two Feynman diagrams contribute to the axion-photon coupling: coupling of the axion to two photons via a triangle loop through fermions carrying PQ and electric charges (left image), and axion-pion mixing (right image) [3].

where $g_{a\gamma}$ is the coupling constant, F the electromagnetic field tensor and $\tilde{F}$ its dual. $\vec{E}$ and $\vec{B}$ denote the electric and the magnetic field respectively. The coupling constant is given as [22]

$$g_{a\gamma} = -\frac{\alpha}{2\pi f_a}\left(\frac{E}{N} - \frac{2}{3}\frac{(4+z+w)}{(1+z+w)}\right) \tag{2.17}$$

with α being the fine structure constant and both z and w as in Equation (2.14) and Equation (2.15), respectively, and thus, by inserting z and w, one obtains

$$g_{a\gamma} = -\frac{\alpha}{2\pi f_a}\left(\frac{E}{N} - 1.92 \pm 0.08\right). \tag{2.18}$$

The ratio E/N depends on the axion model. While N is the color anomaly of the axion current, E represents its electromagnetic anomaly. They are defined as [22]:

$$E \equiv 2\sum_j X_j Q_j^2 D_j \tag{2.19}$$

$$N \equiv \sum_j X_j \tag{2.20}$$

where for quarks (color triplets) $D_j = 3$ and for charged leptons (color singlets) $D_j = 1$. Moreover, X_j and Q_j denote the PQ and the electric charges respectively. If there are external electric or magnetic fields, this coupling allows for both axion decay $a \to 2\gamma$ and conversion through the Primakoff effect $a \leftrightarrow \gamma$ (more details will follow in Sect. 3.1.1).

Interaction of Axions with Fermions

Axions couple to fermions and the Lagrangian of this interaction is

$$\mathcal{L}_{af} = \frac{g_{af}}{2m_f}\bar{\Psi}_f \gamma^\mu \gamma_5 \Psi_f \partial_\mu a, \tag{2.21}$$

where f denotes the fermion, i.e. the electron or the nucleon in our case. For the fermion mass m_f, g_{af} is given by

$$g_{af} = \frac{C_f m_f}{f_a} \tag{2.22}$$

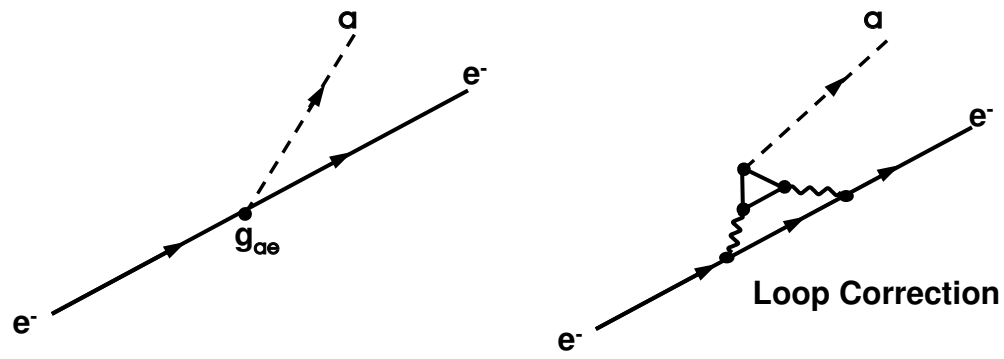

Figure 2.3: Axion-electron coupling. Left image: Direct axion-electron interaction is only possible for DFSZ axions, and it can thus be used to distinguish these axions from the hadronic or KSZV axions. Right image: Higher order coupling of axion and electron. Hadronic axions can only interact with electrons via this coupling [34].

with C_f being an effective PQ charge. g_{af} acts as a Yukawa coupling and $\alpha_{aj} \equiv g_{af}^2/4\pi$ plays the role of an "axionic fine structure constant" [22]. So, if quarks and electrons carry PQ charge[9], these Yukawa couplings to axions can be observed. Since quarks cannot be isolated (due to confinement), the interaction of axion and nucleon has to be considered.

Coupling to Electrons (Tree Level and Radiatively Induced) If electrons carry PQ charge, as they do in certain axion models (DFSZ, see Sect. 2.2.2), there will be a tree-level coupling with axions as in Equation (2.21), where g_{af} for the electron is [22]:

$$g_{ae}^{tree} = \frac{C_e m_e}{f_a} = C_e\, 0.85 \times 10^{-10} m_{eV}. \tag{2.23}$$

m_{eV} is given by $m_{eV} = m_a/\text{eV}$ and C_e depends on the "effective" PQ charge of the electron[10], namely $C_e = X_e^{'}/N$. However, even if $X_e^{'} = 0$, as it can be found in other axion models (KSVZ, see Sect. 2.2.2), there still is a so-called radiatively induced coupling of axions to electrons at a one-loop level with a g_{ae}^{rad} more complicated and smaller than g_{ae}^{tree} [27], thus leading to a smaller contribution to the Lagrangian compared to the tree-level interaction. The Feynman graphs for both kinds of axion-electron coupling are shown in Figure 2.3.

Coupling to Nucleons The general coupling constant g_{af} from Equation (2.22) becomes [22, 27, 28]

$$g_{aN} = \frac{C_N m_N}{f_a} = C_N 1.56 \times 10^{-7} m_{eV} \tag{2.24}$$

[9] This depends on the axion model.

[10] Actually, this is just done to absorb the color anomaly N in the definition of C_e [22].

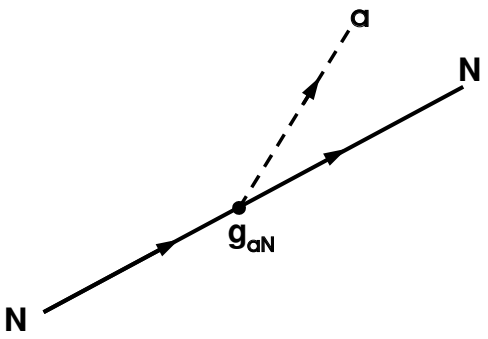

Figure 2.4: Feynman diagram of axion-to-nucleon coupling.

in the case of axion-to-nucleon coupling (see Fig. 2.4).
C_N is different for proton and neutron:

$$C_p = (C_u - \eta)\Delta u + (C_d - \eta z)\Delta d + (C_s - \eta w)\Delta s, \tag{2.25}$$
$$C_n = (C_u - \eta)\Delta d + (C_d - \eta z)\Delta u + (C_s - \eta w)\Delta s, \tag{2.26}$$

where $\eta = (1 + z + w)^{-1}$ and z and w given again as in Equations (2.14) and (2.15), respectively. Δq is the helicity contribution of the nucleon as it is carried by the quark q (with $q = u, d, s$). The numbers for this purpose are, with errors of about ± 0.03 per value [22, 29]:

$$\Delta u = +0.85, \quad \Delta d = -0.41, \quad \Delta s = -0.08. \tag{2.27}$$

Thus, g_{aN} (Equation (2.24)) can be calculated (still depending on the axion model, however).

2.2.2 Axion Models

Axions can be seen in the context of different models. The distinguishing feature between the two major axion model classes is the size of the PQ scale f_a, which is inversely proportional to the axion mass m_a, as mentioned before:

- f_a small $\rightarrow$ m_a large: Visible Axions
- f_a large $\rightarrow$ m_a small: Invisible Axions

Further differentiation of these two classes is, of course, possible.

Visible Axions

The *standard axion model*, as it was originally proposed by Peccei, Quinn, Weinberg and Wilczek (PQWW) [17–19] (see also Sect. 2.1.4), and its variants assume an axion decay

constant of about the size of the electroweak constant, i.e. $f_a \approx f_{weak} \approx 250$ GeV, implying an axion mass of the order $m_a \approx 200$ keV. This kind of axions, known as *visible* or *PQWW-axions*, have been ruled out by numerous experiments as well as astrophysical considerations [13].

Invisible Axions

For weaker couplings of the axion, i.e. at a large scale $f_a \gg f_{weak}$, the axion has been able to escape detection in previous experiments, thus the name *invisible* axion. In models of this kind, an electroweak singlet Higgs field Φ (complex scalar field) with a vacuum expectation value of $f_a/\sqrt{2}$ is introduced. This field is not interacting electroweakly. The two important models are the KSVZ[11] and the DFSZ[12] model. Their main distinguishing feature is the coupling of axion to electrons. They both manage to solve the CP-Problem.

KSVZ-Model The first to suggest an invisible axion model were Kim, Shifman, Vainshtein, and Zakharov [30,31]. In the frame of this scenario, leptons and quarks do not carry PQ charge (that is $C_e = C_u = C_d = C_s = 0$), while some exotic heavy quarks do.
The KSVZ axions are also called *hadronic axions*, because they cannot couple to electrons in the tree level for this reason. A weaker coupling to electrons does exist, though.
KSVZ axions couple to nucleons as shown in Equation (2.24). Evaluation of Equation (2.25) and (2.26) yields to

$$C_p = -0.39, \tag{2.28}$$
$$C_n = -0.04, \tag{2.29}$$

and consequently for the coupling constants, one obtains:

$$g_{ap}^{KSVZ} = \frac{C_p m_p}{f_a} = -6.01 \times 10^{-8} m_{eV}, \tag{2.30}$$
$$g_{an}^{KSVZ} = \frac{C_n m_n}{f_a} = -0.69 \times 10^{-8} m_{eV}. \tag{2.31}$$

As far as the interactions with photons are concerned, Equation (2.18) holds, but different types of KSVZ models suggest different values for E/N. Consequently, this coupling can be either suppressed or enhanced [28].

DFSZ-Model Another approach to describe the invisible axion was presented by Dine, Fischler, Srednicki and Zhitnitskiĭ [32, 33]. In this model, the fundamental fermions carry PQ charge. Therefore, no exotic heavy quarks are needed. Instead of just using an electroweak singlet scalar field Φ, as it is done in the KSVZ model, two doublet fields (Φ_1, Φ_2) are introduced in addition. Their vacuum expectation values are f_1 and f_2, respectively [22].
Since the DSFZ axions can be implemented in Grand Unified Theories (GUT) without

[11] Named after the first people to publish about this model: Kim, Shifman, Vainshtein, and Zakharov.
[12] Honoring the first people to introduce this model: Dine, Fischler, Srednicki and Zhitnitskiĭ.

major difficulties, the DFSZ model is also referred to as a Grand Unified Model.

Direct coupling to electrons is possible in this scenario. C_e is given (for N_f being the number of families) as follows:

$$C_e = \frac{\cos^2 \beta}{N_f} \tag{2.32}$$

and hence the coupling constant can be obtained (following Equation (2.23)) as

$$g_{ae}^{DSFZ} = 0.85 \times 10^{-10} m_{eV} \frac{\cos^2 \beta}{N_f} = 0.28 \times 10^{-10} m_{eV} \cos^2 \beta \tag{2.33}$$

in which the last part of the equation results from the assumption that $N_f = 3$. The term $\cos \beta$ is a parametrization of $x = f_1/f_2$ (see Ref. [22] for a more detailed description).

For the coupling of axions to nucleons the following equations for C_u, C_d, and C_s hold:

$$C_d = C_s = C_e = \frac{\cos^2 \beta}{N_f}, \tag{2.34}$$

$$C_u + C_d = \frac{1}{N_f}, \tag{2.35}$$

$$C_u - C_d = -\frac{\cos^2 \beta}{N_f}, \tag{2.36}$$

which leads to

$$C_d = C_s = \frac{\cos^2 \beta}{N_f}, \tag{2.37}$$

$$C_u = \frac{\sin^2 \beta}{N_f}. \tag{2.38}$$

Consequently, using equation (2.25) and (2.26) as well as $N_f = 3$, one obtains:

$$C_p = -0.10 - 0.45 \cos^2 \beta, \tag{2.39}$$

$$C_n = -0.18 + 0.39 \cos^2 \beta. \tag{2.40}$$

For the interaction of axions and photons, following equation (2.18) with $E/N = 8/3$ for any GUT, the coupling constant is given by:

$$g_{a\gamma}^{DFSZ} \approx -0.75 \frac{\alpha}{2\pi f_a}. \tag{2.41}$$

2.2.3 Origin of Axions

Different possible sources for axions exist. Relict axions could have been produced by three distinct processes in the early universe (see Ref. [34] and references therein): thermal production [35], production through the misalignment effect in the early universe [36–38],

and the decay of primordial topological defects, such as axion strings [39]. It is not sure, which of these processes dominates, since this depends on both the axion mass and whether or not inflation took place. Thermal production yields hot dark matter axions (relativistic axions), while non-relativistic axions would originate from the misalignment effect and the decay of topological defects.
Beside these relict axions, in the cores of stars, such as our Sun, axions or axion-like particles can be produced through Primakoff conversion of blackbody photons, causing these celestial objects to lose energy. More details on this so-called solar axions can be found in the following chapter.
Furthermore, it is possible to produce axions in the laboratory by sending light, preferably a strong laser beam, through a transverse magnetic field[13]. This can be very useful for the experimental detection.

2.3 The Theoretical Limits on Axion Mass and Coupling Constant

In principle, since all values for the PQ breaking scale f_a solve the strong CP-Problem, m_a is completely arbitrary. Before experiments start searching for the axion, however, it is possible, on the basis of astrophysical and cosmological considerations, to exclude several ranges of masses, leaving only a small window (10^{-5} eV$\lesssim m_a \lesssim 10^{-2}$ eV), where axions could still exist.

2.3.1 Astrophysical Limits

Despite their small interaction with normal matter, axions have a considerable influence on the evolutions of stars. Axions could be produced in the interior of stars by different processes and, hence, provide an additional energy loss channel, through which energy from nuclear reactions in the core of the star could be carried away directly. As a consequence, the star will contract and increase its luminosity as well as its central temperature in order to adjust to the new situation. This, in turn, will then lead to a shortening of the star's lifetime due to faster consumption of fuel. It is possible to put limits on the coupling of axions to photons, electrons and nucleons by demanding that time scales of stellar evolution match with observational limits [22].

The best limits on axion-photon coupling can be obtained from low-mass stars with a helium-burning core, known as Horizontal Branch (HB) stars. By observing the ratio of HB stars and low-mass red giants in globular clusters, in which axion emission is suppressed compared to the HB stars, the coupling constant $g_{a\gamma} \lesssim 0.6 \times 10^{-10}$ GeV^{-1} and the axion mass limit is given by [22]

$$m_a \lesssim 0.4 \text{ eV} \qquad \text{(for GUT axion models, i.e. E/N = 8/3)} \tag{2.42}$$

[13] In order to mix a photon with an axion, the external magnetic field has to be such that it fits the missing quantum numbers. Since the photon has spin one but the axion is a spin-zero particle, the magnetic field has to be a transverse one [22].

due to the fact that the Primakoff conversion $\gamma + Ze \rightarrow Ze + a$ is not dominant. This horizontal branch limit, which is also referred to as globular cluster limit, might however vary by a factor of 2 due to uncertainties in its determination [40]. Therefore, when it is plotted in the exclusion plot for $g_{a\gamma}$ (see Fig. 4.23) in order to provide a comparison for the results of CAST and other experiments, the limit $g_{a\gamma} \lesssim 1.0 \times 10^{-10}$ GeV^{-1} is used.

A rather strict constraint on the axion-to-nucleon coupling can be derived by observing the measured neutrino signal from the supernova SN 1987A. Its duration places a limit because after the collapse, neutrinos are trapped inside the hot and dense core and escape is only possible by diffusion, while axion emission would carry away energy from the interior, observable in late-time neutrinos [41]. This is possible, if axions interact feebly enough. Two arguments make up the limit set by SN 1987A, probably leaving a little gap between each other (see Fig. 2.5), called the "hadronic axion window" [42]. If axions interact too strongly, they are trapped in the SN core, thus implying, they cannot be excluded by the SN signal if their mass is larger than a certain mass limit, namely $m_a \gtrsim 10^{-2}$ eV [43, 44]. Nevertheless, some of the energy is carried away by axions leading to a remarkable large signal in the detectors for the neutrinos (Cherenkov Detectors) or, at least, altering the neutrino flux considerably. Hence, another range of axion masses can be excluded [45]. Due to the hadronic axion window, eV-axions might be allowed in axion models which highly suppress tree-level axion-electron coupling (such as KSVZ) and could be a hot dark matter candidate.

Constraints for the axion-to-electron coupling can be obtained from the luminosity function of white dwarfs and from globular-cluster stars, but the achievable limits are unable to exclude more regions than the previous arguments already do [42].

2.3.2 Cosmological Limits

In case axions were interacting strongly enough, i.e. $f_a \lesssim 10^8$ GeV, in the early universe, a thermal equilibrium state would have been reached before the QCD phase transition occurred. However, this range is already excluded by the astrophysical considerations mentioned above. Hence, axions were produced non-thermally, since $f_a \gtrsim 10^8$ GeV.

Inflation Scenario

If inflation took place only after the breaking of the PQ-Symmetry, i.e. the temperature of the universe, T_{univ}, below the PQ scale f_a, then the misalignment mechanism [36–38] would have caused a contribution to the cosmic critical density Ω of

$$\Omega_a h^2 \approx 1.9 \times 3^{\pm 1} \left(\frac{1\mu\text{eV}}{m_a} \right)^{1.175} \Theta_{i.m.}^2 F(\Theta_i) \tag{2.43}$$

with the Hubble constant h in units of 100 km s^{-1}Mpc^{-1} and any anharmonic corrections to the axion potential included in $F(\Theta)$ [42]. $\Theta_{i.m.}$, the initial misalignment of the QCD Θ-parameter, can be close to zero or close to π, but, in order to avoid fine-tuning, $\Theta_i^2 F(\Theta_i) \approx 1$ would be the expected value. Due to observations of temperature fluctuations of the cosmic

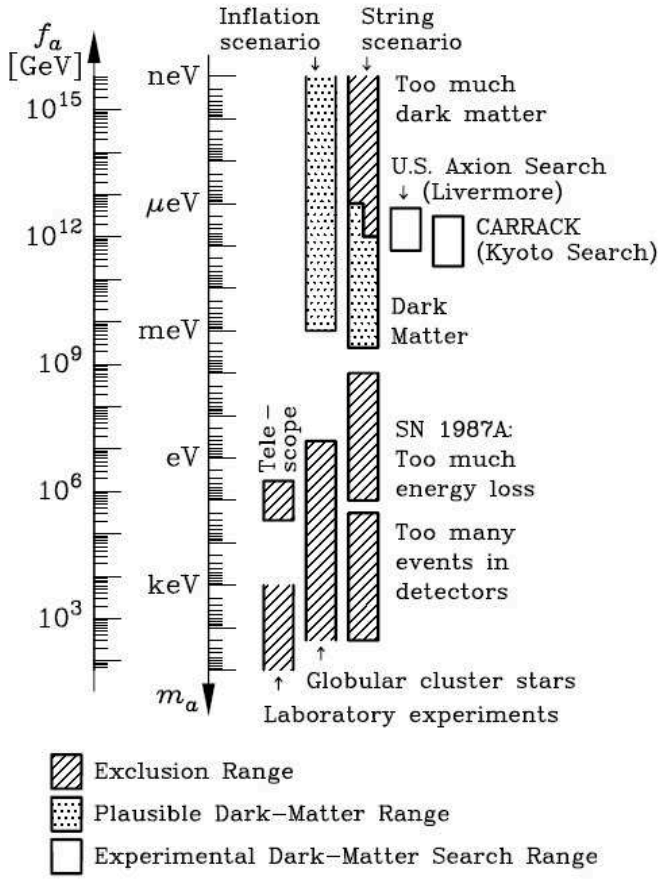

Figure 2.5: Astrophysical and cosmological exclusion regions for the axion mass m_a and, equivalently, the PQ scale f_a. Open-ended bars represent a rough estimate, i.e. its location is model-dependent or has not been established. Since the globular-cluster limit is derived from axion-to-photon coupling, it is model-dependent. GUT or DFSZ models with $E/N = 8/3$ were used here. The limit from the SN 1987A depends on the axion-nucleon-coupling and thus, what is shown here is exact for KSVZ and approximately for DFSZ axions. The dotted regions indicate, where axions could form the cosmic dark matter. Some experiments searching for galactic dark matter axions are also included in the figure (taken from Ref. [50]).

microwave background (CMBR), caused by quantum fluctuations of the axion field during inflation [46], this fine-tuning of the initial angle Θ_i is constrained. According to Ref. [47] the axion mass is thus below $m_a \lesssim 10^{-3}$ eV (see Fig. 2.5).

String Scenario

In another scenario, namely if inflation took place before PQ-Symmetry breaking ($T_{\text{univ}} > f_a$) or if it did not happen at all, cosmic axion strings came into existence [39]. Axion emission makes the strings lose energy. After QCD phase transition, axions acquire their mass and behave no longer relativistic. In principle, the axion density obtained for misalignment and the one for this case are comparable. However, exact results are a controversial issue (Compare Ref. [48] to Ref. [49]). A feasible range, considering the occurring uncertainties, for the string scenario is shown in Figure 2.5.

Concluding, all these constraints do not leave more than a window from μeV to some meV for hadronic axions. Nevertheless, experiments also searched the "prohibited" regions, because neither astrophysical nor cosmological considerations are absolutely stringent. All the astrophysical and cosmological constraints discussed are summarized in Figure 2.5. Additional restrictions on possible axion masses and coupling constant ranges were accomplished by laboratory experiments and thus these will be considered in the following section.

2.4 The Detection of the Axion

As mentioned above, the existence of visible axions could be excluded rather early by considering the effect they would have on stellar evolution (proof through experiments followed a little bit later [13,51]). Pierre Sikivie was the first to propose several experiments on how to detect invisible axions [52]. His suggestion was that it should be possible to convert axions into mono-energetic photons by using a strong magnetic field (Primakoff effect, see Sect. 3.1.1 for a more detailed description of this effect). Since this axion-to-photon coupling is a consequence of the PQ axion-gluon interaction, it can be found in all axion models, and therefore it is used in all experiments to detect the hypothetical particle. Basically, three different types of axions are looked for (see Sect. 2.2.3): galactic axions, solar axions and laboratory axions. The kinds of experiments performed in order to obtain limits on $g_{a\gamma}$ can be distinguished in three major groups, which will be described in the following:

- Haloscope and Telescope Searches (looking for galactic axions)
- Laser Experiments (using laboratory axions)
- Helioscopes (searching for axions coming from the Sun).

In Figure 2.6, an exclusion plot for the different kinds of axion search experiments provides an overview.

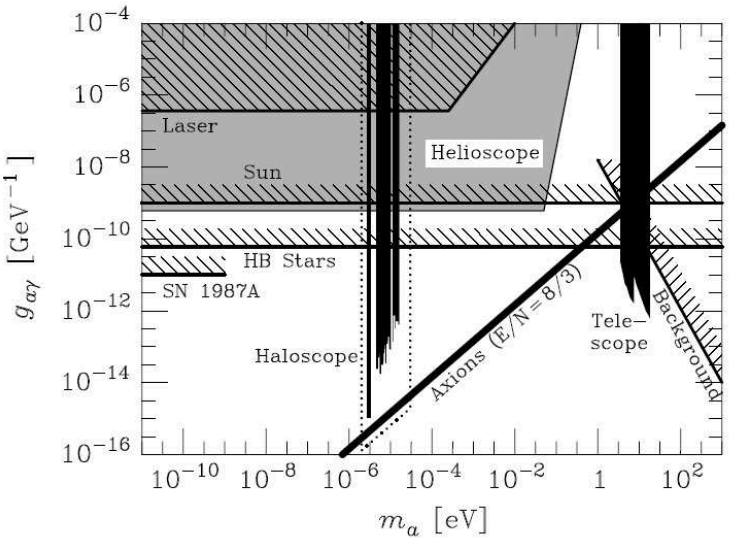

Figure 2.6: Exclusion region for various experiments [50]. The axion-photon coupling constant is plotted versus the axion mass. The astrophysical limit from horizontal branch (HB) stars is added as well. The limits are valid for any pseudoscalar particle, except if haloscopes are used, since these searches assume that the particles are galactic dark matter. Dotted lines refer to ongoing dark matter axion searches.

2.4.1 Haloscope and Telescope Searches

Haloscopes

Microwave Cavity Experiments are searching for galactic halo axions and are thus referred to as haloscopes. Axions (of the order μeV) are converted into photons of a frequency in the GHz range, when passing through a strong, static magnetic field. Coupling of axions is only possible to TM[14] modes of the cavity, so tuning the frequency of the cavity is required, because the axion mass is unknown.
Two pilot experiments (RBF[15] [53], UF[16] [54]) were performed and able to exclude axions of a certain mass range, namely

$$4.5\ \mu\text{eV} < \text{m}_\text{a} < 16.3\ \mu\text{eV}.$$

Follow-up experiments show or will show higher sensitivity, even though they are using setups based on the same principle. So far, the excluded mass range (ADMX[17] at LLNL[18], for results see Refs. [55, 56]) is

$$1.9\ \mu\text{eV} < \text{m}_\text{a} < 3.3\ \mu\text{eV}.$$

[14]Transversal Magnetic
[15]Rochester-Brookhaven-Fermilab
[16]University of Florida
[17]Axion Dark Matter eXperiment
[18]Lawrence Livermore National Laboratory

Further improvements are expected by using new technologies (SQUID[19] amplifiers [57] in order to reduce the noise, and later on dilution refrigerators to decrease the temperature of the cavity further).
A different approach, as set up in Kyoto, Japan, with CARRACK[20] I and II, exploits Rydberg atoms to detect the photons. CARRACK I performed a search in the 8 % range around 10 μeV, while CARRACK II is about to investigate the region of 2 μeV$< m_a <$ 50 μeV [58].

Telescopes

Thermally produced axions, so-called "multi-eV" axions, can be searched for with telescopes, because they should decay into two photons. The most likely places to find such axions are clusters of galaxies [59]. By decaying, these axions will produce an emission line, which, however, could not be observed in the experiment (Kitt Peak National Observatory [60]) and thus the following range does not qualify for axion masses:

$$3 \text{ eV} < \text{m}_\text{a} < 8 \text{ eV}.$$

The radio telescope at the Haystack Observatory [61] was able to rule out coupling constants for masses in the range of 298 μeV$< m_a <$ 363 μeV with:

$$g_{a\gamma} > 1.0 \times 10^{-9} \text{ GeV}^{-1}.$$

2.4.2 Laser Experiments

"Shining Light through Walls" Experiments

In "Shining Light through Walls" or beam dump experiments, a strong laser beam is sent through a magnetic field. There, a part of the photons is converted into axions. Then, a wall or shield blocks the photons, while the feebly interacting axions can pass through to the other side, where they are reconverted into photons by another magnetic field (see Fig 2.7) and detected [63, 64].
Instead of the beam, resonating cavities can be used on either side as well [65]. Results from such an experiment [66] yielded an upper bound for the coupling constant of

$$g_{a\gamma} < 7.7 \times 10^{-7} \text{ GeV}^{-1}$$

for axion masses $m_a < 10^{-3}$ eV.

Polarization Experiments

Axions should change the polarization of the photon beam before and after the wall in the previous kind of experiments (see Fig. 2.8), such that the polarization plane of the incident beam is rotated (Dichroism) and, in addition, there is an ellipticity of the passing

[19] Superconducting QUantum Interference Devices
[20] Cosmic Axion Research using Rydberg Atoms in a resonant Cavity in Kyoto

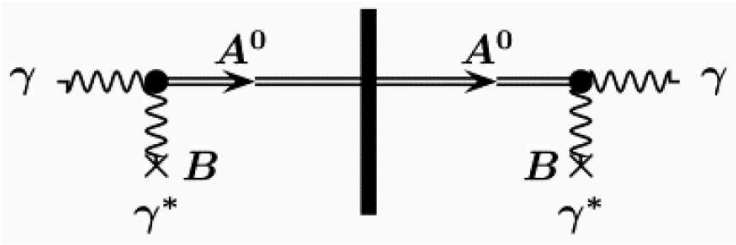

Figure 2.7: Basic principle of a “Shining Light through Walls" experiment. An incoming photon beam is partly converted into axions. A wall keeps the remaining photons from getting to the other side, while the axions pass the shield. Beyond the barrier, the axions can be backconverted in another magnetic field, and then the resulting photons can be detected (Figure taken from Ref. [62]).

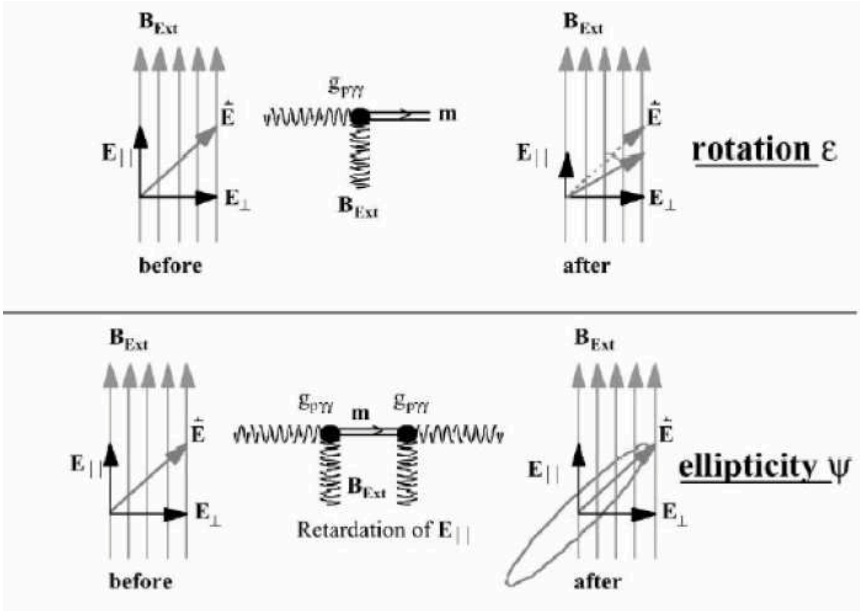

Figure 2.8: Upper image: Principle of the formation of Dichroism, i.e. a rotation of the polarization plane, induced by the creation of a massive particle which couples to two photons. Lower image: Principle of development of Ellipticity induced by the retardation of an electric field component relative to the other, when a massive particle is produced (two photon coupling) [62].

beam observable, while the incident beam was linearly polarized (Vacuum Birefringence). Both effects would be noticeable. Results of such an experiment, accomplished by Semertzidis et al. [67], gave the following results:

$$g_{a\gamma} < 2.5 \times 10^{-6} \text{ GeV}^{-1}$$

for axion masses $m_a < 7 \times 10^{-4}$ eV.

PVLAS[21], a more recent experiment of this kind, observed a strong effect, which might be interpreted tentatively as a axion-like particle. The required coupling strength of axions to photons, however, would be around 3×10^{-6} GeV^{-1}, and thus ruled out by other experiments (such as e.g. CAST [68, 69]), the globular-cluster limit and observed properties of the Sun. Nevertheless, there are first attempts to find a new model of particle physics, in which the PVLAS signal would fit. For further details see Ref. [70] and references therein.

2.4.3 Helioscopes

Searches for solar axions are performed by using helioscopes. One can either utilize an electric field for axion-to-photon conversion via the Primakoff effect or a magnetic one.

In an electric field, as it can be provided by crystalline detectors, axion-to-photon conversion is coherent, if the Bragg condition is fulfilled [71, 72]. Three experiments were looking for these characteristic Bragg patterns:

- The SOLAX[22] experiment [73] used a Germanium Spectrometer giving a bound on $g_{a\gamma}$ of
$$g_{a\gamma} < 2.7 \times 10^{-9} \text{ GeV}^{-1}$$
for axion masses up to about 1 keV.

- The COSME detector [74] at the Canfranc Underground Laboratory, which is a Germanium detector as well, accomplished to reach a similar result, namely
$$g_{a\gamma} < 2.78 \times 10^{-9} \text{ GeV}^{-1}$$
being mass independent, however depending on the solar model.

- The DAMA[23] experiment [75] on its part used NaI(Tl) crystals and achieved a limit of
$$g_{a\gamma} < 1.7 \times 10^{-9} \text{ GeV}^{-1}$$
for masses in the eV range.

[21] Polarizzazione del Vuoto con Laser (Vacuum Polarization with Laser)
[22] SOLar AXion search in Argentina
[23] Particle DArk MAtter searches with highly radiopure scintillators at Gran Sasso

However, the approach to detect solar axions with the help of an electric field turned out to be somewhat limited [76], because neither present nor future crystal detector experiments will be able to challenge the limit set by globular clusters.

The second type of "axion helioscopes" applies a transverse magnetic field to convert the incoming axions into photons [52, 77]. The first experiment to use this technique was performed by Lazarus et al. [78] examining two axion mass regions and leading to the following results:

$$g_{a\gamma} < 3.6 \times 10^{-9}\ \mathrm{GeV}^{-1} \qquad \text{for } \mathrm{m_a} < 0.03\ \mathrm{eV}$$

and

$$g_{a\gamma} < 7.7 \times 10^{-9}\ \mathrm{GeV}^{-1} \qquad \text{for } 0.03\ \mathrm{eV} < \mathrm{m_a} < 0.11\ \mathrm{eV}.$$

Following this experiment, the Tokyo Axion Helioscope [79] continued the search using the same method, but providing better sensitivity, and thus leading to a more restrictive limit:

$$g_{a\gamma} < 6.0 \times 10^{-10}\ \mathrm{GeV}^{-1} \qquad \text{for } \mathrm{m_a} < 0.03\ \mathrm{eV}.$$

At the present time, the CERN Axion Solar Telescope (CAST), which is going to be described in more detail in Chapter 4, is looking for axions using the same basic principle, however, with a considerably increased sensitivity.
A very helpful overview of direct searches for axions can be found in Ref. [80].

Chapter 3

The Solar Axion

The Sun as one of the closest axion sources is used in experimental searches, such as CAST, and thus a closer look will be taken at the so-called solar axions. First, the origin of these particles will be considered and the influence of the solar model used to calculate the axion flux from the Sun as observable on Earth is studied. In order to detect axions from the Sun, helioscopes are generally used and thus axion-to-photon conversion in a magnetic field via the Primakoff effect is an important issue to be discussed. Finally, some further considerations for the application of helioscopes, such as the ephemeris calculation and the refraction of light in the atmosphere (necessary for optical crosschecks of systems tracking the Sun), will be taken into account.

3.1 Axions from the Sun and the Solar Model

3.1.1 The Sun as Source of Axions

As mentioned in Section 2.2.3, axions can be produced in the core of stars. The nearest and brightest of this kind of axion sources, and thus the best choice for an observation, is the Sun. In its interior, fluctuating electric fields, originating from the charged particles in the plasma, are present, and therefore blackbody photons can be converted into axions via the Primakoff effect [77, 81], which is shown in Figure 3.1:

$$\gamma + Ze \rightarrow Ze + a.$$

The rate for transition of photons with energy ω into axions can be written as [77]:

$$\Gamma_{\gamma \rightarrow a} = \frac{T_{\odot} \kappa^2 g_{a\gamma}^2}{32\pi} \left[\left(1 + \frac{\kappa^2}{4\omega^2} \right) \ln \left(1 + \frac{4\omega^2}{\kappa^2} \right) - 1 \right], \tag{3.1}$$

where $T_{\odot}$ is the plasma temperature of the Sun and κ the Debye-Hückel scale[1], given by

$$\kappa^2 = \frac{4\pi\alpha}{T_{\odot}} \sum_j Z_j^2 N_j. \tag{3.2}$$

[1] It describes screening effects.

Figure 3.1: The Primakoff effect in the Sun: a photon converts into an axion in the presence of fluctuating electric fields (left). In a laboratory magnetic field the inverse process can take place and an incoming solar axion can couple to a virtual photon provided by the transverse magnetic field resulting in a real photon (right). Image taken from Ref. [3].

Here, α denotes the fine-structure constant and N_j is the number density of charged particles, which are carrying the charge $Z_j e$. In terms of photon energy w and momentum k as well as by using the axion momentum p, Equation (3.1) writes [82]:

$$\Gamma_{\gamma\to a} = \frac{T_\odot \kappa^2 g_{a\gamma}^2}{32\pi}\frac{k}{\omega}\left\{\frac{\left[(k+p)^2+\kappa^2\right]\left[(k-p)^2+\kappa^2\right]}{4kp\kappa^2}\ln\left[\frac{(k+p)^2+\kappa^2}{(k-p)^2+\kappa^2}\right] - \frac{\left(k^2-p^2\right)^2}{4kp\kappa^2}\ln\left[\frac{(k+p)^2}{(k-p)^2}\right]-1\right\}. \tag{3.3}$$

Axion and photon have virtually the same energy. The axion energy E_a is smeared by the plasma frequency, which is approximately 0.3 keV, and thus small compared to the photon energies (about $3T_\odot \approx 4$ keV, since the temperature in the solar core is $T_\odot \approx 1.3$ keV). Therefore, Equation (3.3) turns to:

$$\Gamma_{\gamma\to a} = \frac{T_\odot \kappa^2 g_{a\gamma}^2}{32\pi}\left\{\frac{\left(m_a^2-\kappa^2\right)^2+4E_a^2\kappa^2}{4E_a p\kappa^2}\ln\left[\frac{(E_a+p)^2+\kappa^2}{(E_a-p)^2+\kappa^2}\right] - \frac{m_a^4}{4E_a p\kappa^2}\ln\left[\frac{(E_a+p)^2}{(E_a-p)^2}\right]-1\right\}, \tag{3.4}$$

with $k = E_a$, $p = \sqrt{E_a^2 - m_a^2}$ and m_a being the axion mass.

The differential axion flux on Earth $d\Phi_a(E_a)/dE_a$ can be obtained from this, by folding the transition rate with the solar distribution of blackbody photons and integrating over a standard solar model as described by Bahcall *et al.* [83] in 1982. Van Bibber *et al.* derive a well-approximated formula for this [77]:

$$\frac{d\Phi_a(E_a)}{dE_a} = 4.02\times10^{10}\left(\frac{g_{a\gamma}}{10^{-10}\mathrm{GeV}^{-1}}\right)^2\frac{(E_a/\mathrm{keV})^3}{e^{(E_a/1.08\mathrm{keV})}-1}\left[\mathrm{cm}^{-2}\mathrm{s}^{-1}\mathrm{keV}^{-1}\right]. \tag{3.5}$$

The average axion energy is $\langle E_a\rangle = 4.2$ keV. The corresponding plot is shown in Figure 3.2.

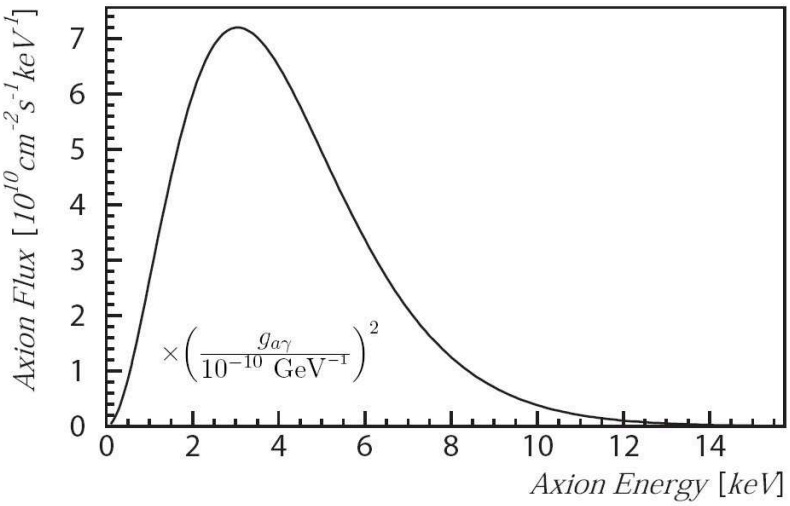

Figure 3.2: The differential flux of axions from the Sun at the Earth (taken from Ref. [3]). The average energy is 4.2 keV, while the maximum of the flux can be observed at an energy of 3 keV [77].

3.1.2 Comparison with the Modern Solar Model

The total axion flux at the Earth, Φ_a, can be calculated from Equation (3.5) based on the standard solar model from 1982 as [77]:

$$\Phi_a = 3.54 \times 10^{11} \left(\frac{g_{a\gamma}}{10^{-10}\ \mathrm{GeV}^{-1}} \right)^2 \ \mathrm{cm}^{-2}\ \mathrm{s}^{-1}. \tag{3.6}$$

By using a modern solar model, namely BP2004 by Bahcall and Pinsonneault [84], Φ_a changes to [86]

$$\Phi_a = 3.75 \times 10^{11} \left(\frac{g_{a\gamma}}{10^{-10}\ \mathrm{GeV}^{-1}} \right)^2 \ \mathrm{cm}^{-2}\ \mathrm{s}^{-1}. \tag{3.7}$$

and a fit of the differential flux is given by

$$\frac{d\Phi_a(E_a)}{dE_a} = 6.02 \times 10^{10} \left(\frac{g_{a\gamma}}{10^{-10}\mathrm{GeV}^{-1}} \right)^2 \frac{(E_a/\mathrm{keV})^{2.481}}{e^{(E_a/1.205\mathrm{keV})} - 1} \left[\mathrm{cm}^{-2}\mathrm{s}^{-1}\mathrm{keV}^{-1}\right]. \tag{3.8}$$

It is obvious, however, by comparing Eq. (3.5) and Eq. (3.8) that the expected axion flux hardly depends on which solar model is used (see Fig. 3.3).

For experimental searches, it is essential to know, where exactly most axions are produced inside the Sun. The axion surface luminosity of the solar disk has been calculated and just recently updated according to the modern model BP2004 (see Fig 3.4). From this it can be calculated (see Fig. 3.5), how many axions are expected to emerge from the solar core. Considering the region of 0.1 $R_\odot$ ($R_\odot$, also denoted as R_{sun}, being the radius of the Sun), about 46.8% of the total number of axions expected from the Sun should be observable, while for 0.2 $R_\odot$, approximately 84.3% of all axions are expected [87]. This corresponds to an angle of about 0.05° and 0.10° respectively as seen from Earth.

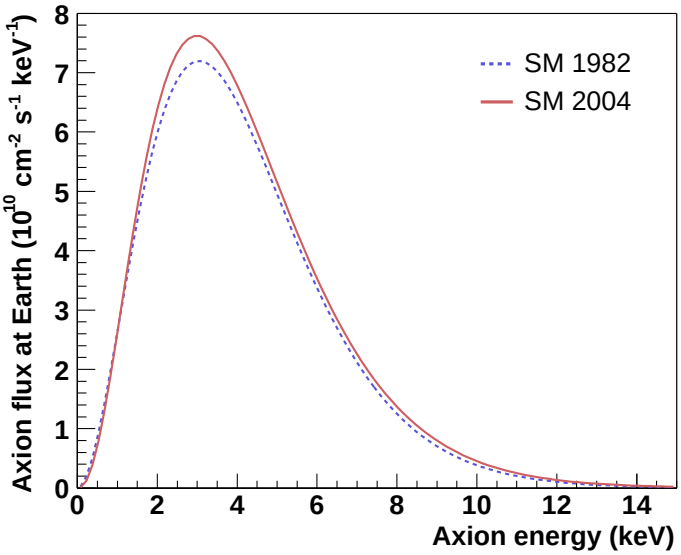

Figure 3.3: The axion flux obtained from the standard solar model (dashed blue line) using Eq.(3.5) compared with the one from a modern solar model (solid red line) using Eq.(3.8) [85].

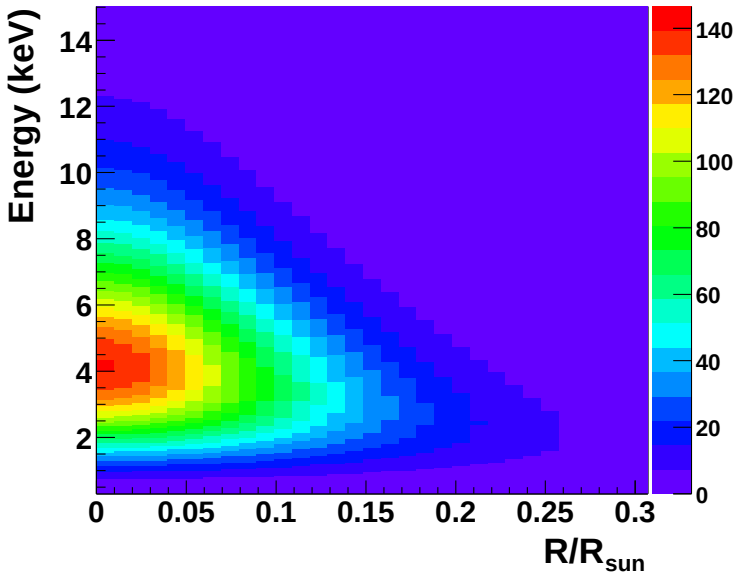

Figure 3.4: Contour plot of the axion surface luminosity of the solar disk shown as a function of a radial coordinate of the solar disk (dimensionless, since it represents the solar radius normalized to the radius of the Sun R_{sun}) and of the axion energy (taken from Refs. [86, 87]). It has been calculated for the modern solar model BP2004. The units are cm^{-2}s^{-1}keV^{-1} per unit surface on the solar disk.

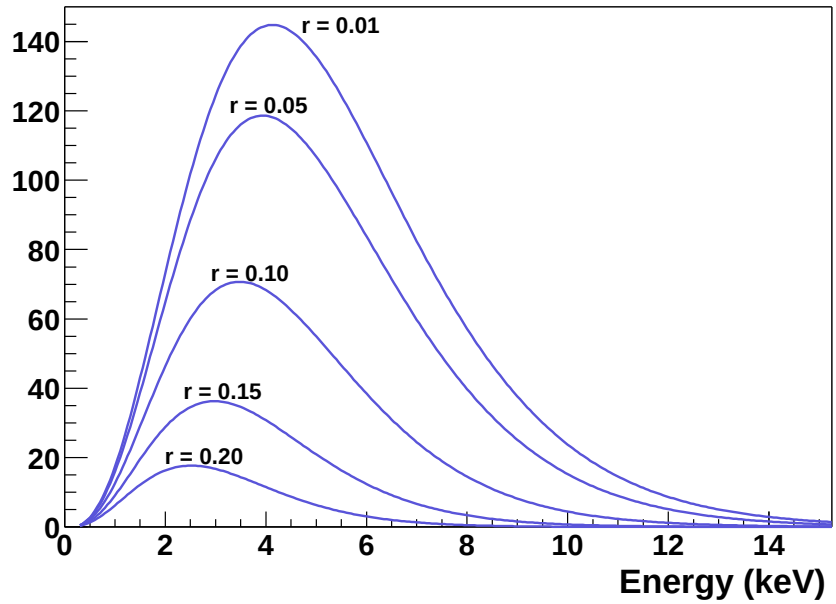

Figure 3.5: The axion surface luminosity of the solar disk is shown for different values of the radial coordinate $r = R/R_{sun}$ [85]. The considered intervals are $\Delta r = 0.01$ and $\Delta E = 0.05$ keV. The units are the same as in Fig. 3.4. By integrating over all radii, one can obtain the total axion flux.

3.2 The Detection of Solar Axions in a Magnetic Field

3.2.1 Solar Axion Conversion in Helioscopes

In a laboratory magnetic field, the inverse Primakoff effect takes place (see Fig. 3.1): The incoming axion converts into a real photon by coupling to a virtual photon provided by the magnetic field:

$$a + \gamma_{\text{virtual}} \rightleftharpoons \gamma.$$

To match the different spins of axion (spin 0) and photon (spin 1) the field has to be transverse. In order to have conversion at any point of the field, the coherence condition has to be fulfilled, i.e. constructive interference is required. This is the case, if the axion field and the photon field are in phase over the full length of the magnetic field. The probability for a conversion then writes [77, 88]:

$$P_{a\to\gamma} = \left(\frac{Bg_{a\gamma}}{2}\right)^2 2L^2 \frac{1-\cos^2(qL)}{(qL)^2}. \tag{3.9}$$

Here, B is the magnetic field, L the length of the magnet, and q the momentum transfer between axion and the photon in the X-ray range. q is defined by

$$q = \frac{m_a^2}{2E_a}. \tag{3.10}$$

In vacuum, the coherence condition (Equation (3.9)) is fulfilled for:

$$qL \ll 1. \tag{3.11}$$

Axion masses of 0.03 eV at the most could thus be observed in a magnetic field of 10 m length.
To look at higher masses m_a, coherence can be restored (for a narrow mass range) by filling the magnet pipes with a low-Z buffer gas, such as helium or hydrogen. Van Bibber *et al.* [77] derived a formula for the conversion probability $P_{a\to\gamma}$, which considers X-ray absorption in the gas by including the inverse photon absorption length Γ for X-rays in a medium:

$$P_{a\to\gamma} = \left(\frac{Bg_{a\gamma}}{2}\right)^2 \frac{1}{q^2+\Gamma^2/4}\left[1+e^{-\Gamma L}-2e^{-\Gamma L/2}\cos(qL)\right]. \tag{3.12}$$

The momentum transfer for this case then turns out to be:

$$q = \left|\frac{m_\gamma^2 - m_a^2}{2E_a}\right|. \tag{3.13}$$

The photon acquires an effective mass, m_γ, proportional to $\sqrt{n_e}$, where n_e is the number density of electrons. As a function of pressure, m_γ is given (for Helium or Hydrogen) by:

$$m_\gamma\ [\mathrm{eV}] \approx \sqrt{0.02\ \frac{\mathrm{P\ [mbar]}}{\mathrm{T\ [K]}}}. \tag{3.14}$$

Equation (3.11) thus translates to:

$$\sqrt{m_\gamma^2 - \frac{2\pi E_a}{L}} < m_a < \sqrt{m_\gamma^2 + \frac{2\pi E_a}{L}}, \tag{3.15}$$

and the coherence condition is satisfied again, such that the effective photon mass matches the axion mass within a small range. By scanning through different gas pressure settings, one is able to study different mass windows up to 0.3 eV for 6.08 mbar at 1.8 K operating temperature (which corresponds to 1 atm at 300 K) using ^{4}He (See Fig. 3.6). After conversion, N_γ photons are expected for the effective detector area S and the observation time t given in days (Efficiency of the detector not included):

$$N_\gamma = \Phi_a \times P_{a\to\gamma} \times S \times t \propto g_{a\gamma}^4. \tag{3.16}$$

From this number, the exclusion plot for the coupling constant $g_{a\gamma}$ (see Fig. 4.23) can be calculated.

3.2.2 Further Considerations for Using Helioscopes

For detection of solar axions with helioscopes, it is important to be aligned with the solar core very precisely and for the longest time possible, in order to capture as many axions as possible and convert them into photons. Therefore, most helioscopes are able to track the

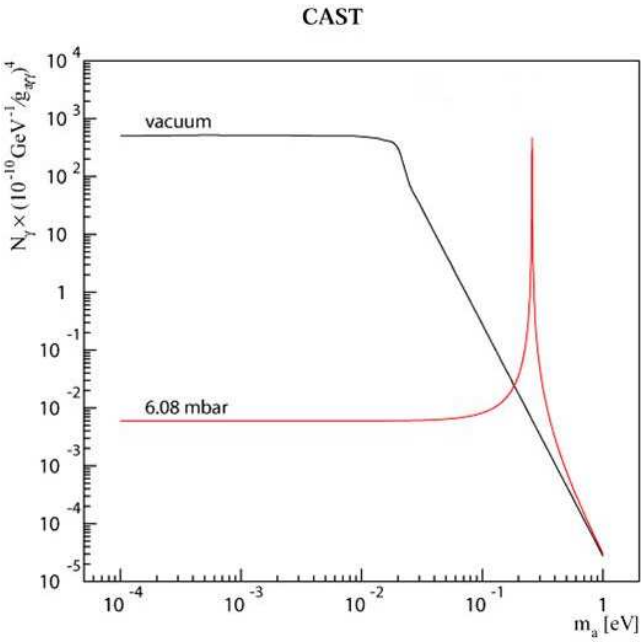

Figure 3.6: Pressure Dependence of the Measurements. In vacuum (black line), a range of axion masses up to a certain point (loss of coherence) can be investigated, then the transition rate decreases dramatically. A buffer gas is able to restore coherence, but only for a very narrow mass range (red line). The position of the peak, and thus the mass to be measured, depends on the pressure of the gas [89].

Sun, i.e. to follow it. This, however, makes it necessary to calculate the way of the Sun as observed from Earth in the course of the year. Additionally, the solar tracking should be cross-checked. One possible way to perform such a test of the system is to use a camera, mounted on the helioscope while tracking, in order to film the Sun and thus check the alignment. In this case, however, photons are observed -instead of axions- and it will be necessary to correct for refraction in the atmosphere.

Ephemeris of the Sun

Traditionally, an ephemeris was a look-up table providing the positions of the Sun or planets at a given time. Today, however, a modern ephemeris includes a software that calculates positions of celestial bodies, such as stars, planets, comets or satellites for example, for virtually any desired time. Such ephemerides cover typically many centuries, past and future. This is possible, because celestial mechanics is an accurate theory. However, there are perturbations causing uncertainties, which have their origin in the existence of numerous asteroids with poorly known masses. In order to calculate the Sun's ecliptic[2] several commercial and non-commercial software routines are available. The most widely used and generally accepted one is NOVAS[3] provided by the U.S. Naval Observatory [90]. NASA

[2]The geometric plane which contains the orbit of the Earth is called ecliptic. Most planet's orbits in the Solar System are close to this plane.

[3]Naval Observatory Vector Astrometry Subroutines

offers an online Ephemeris Computation Service, known as JPL[4]'s HORIZONS System [91].

To actually calculate the ephemerides is everything but an easy task. The problem to solve is a multi-body problem: Other planets influence the Earth's way around the Sun, and therefore its orbit is not exactly elliptical. For a n-body problem, $3n$ second-order differential equations of motion have to be solved. It is possible for $n = 2$, but no general solution exists for arbitrary n.
The usage of different coordinate and time systems complicates the calculations even further. The mostly used celestial coordinate systems are [92]:

- **Horizontal Coordinate System:** It is often used to calculate sunrises and sunsets, but hardly to determine ephemerides.
  The observer's local horizon is used as the fundamental plane and the coordinates are altitude[5] (Alt), i.e. the angle between the object and the horizon from $-90°$ (Nadir) to $+90°$ (Zenith), and the azimuth (AZ), i.e. the angle of the object around the horizon (generally measured from the North point towards the East) from $0°$ to $360°$.

- **Equatorial Coordinate System:** It can be geocentric or topocentric, depending on whether the center of the Earth or a point on its surface is chosen as the point of origin.
  The reference plane in this system is the celestial equator[6]. Its coordinates are declination δ and the right ascension α (or the hour angle t, which is defined as the difference between the sidereal time θ and the right ascension α).

- **Ecliptic Coordinate System:** Both heliocentric (solar center as point of origin) and geocentric (Earth's center as point of origin) ecliptic coordinate system exist.
  The fundamental plane here is the ecliptic of the Sun. The coordinates for both systems are the distance of the observed planet to the Sun (or accordingly Earth)[7], r (Δ). The ecliptic latitude b (β) is the angle between ecliptic and the connecting line of the Sun and the observed planet (Earth and the planet), while the ecliptic longitude l (λ) is the angle between vernal equinox and the projection of the Sun-planet (Earth-planet) connection on the ecliptic.

- **Galactic Coordinate System:** This system uses the so-called galactic plane as reference plane, i.e. the planar region, where most of the (visible) mass can be found. The directions perpendicular to the plane point towards the galactic poles, and thus create a spherical coordinate system. Its coordinates are galactic latitude and galactic longitude.

- **Supergalactic Coordinate System:** This system is hardly used for ephemeris calculations and just mentioned here for completeness.

[4] Jet Propulsion Laboratory
[5] The altitude Alt is also referred to as height above horizon HA or h.
[6] The celestial equator is the plane through the center of the Earth perpendicular to its axis.
[7] The information given in brackets refers to the variables generally used in the geocentric system.

Transforming coordinates given in one systems in those of another can be done, but the formulas for this can be rather complicated. Since not only space but also time matters in ephemeris calculation, there exist several time systems used in celestial calculations, which need attention (for more details see for example [92]):

- Julian Date, i.e. the number of days since the first of January 4713 B.C., 12 o'clock Universal Time or Terrestrial Time, is a common measure in astronomic matters.
- International Atomic Time or Temps Atomique International (TAI) is the time kept by about 200 caesium atomic clocks around the world from which the definition of the SI second originates.
- Ephemeris Time (ET) was used in the former definition of the SI-second and in ephemeris calculation of solar system bodies, but it has been replaced by Dynamical Time (Terrestrial Time (TT) as well as Barycentric Dynamical Time (TDB))
- Universal Time (UT), a timescale based on the rotation of the Earth, can be seen as a continuation of the Greenwich Mean Time (GMT), which is the mean solar time on the meridian of Greenwich, England.
- Coordinated Universal Time (UTC) forms the basis of international civil time keeping.
- Sidereal Time is measured approximately by the movement of the stars, exactly by the diurnal motion of the vernal equinox.

Several other (minor) effects make ephemeris calculations difficult. The analemma could be mentioned as an example for these phenomena: Due to the Earth's tilt on its axis and its elliptic orbit around the Sun, recording the Sun's position everyday at the same time from the identical position leads to the figure of an eight in the sky [93].
Aberration (because of the fact that the observer is situated on the moving planet Earth) or changes through runtime of the light for long distances are other effects to be considered. The influence of gravitation on photons is generally negligible.
For these reasons, calculating ephemerides and tracking the Sun precisely is a challenging task. For example at the CERN Axion Solar Telescope experiment, which will be described in the following chapter, a software based on NOVAS is used for following the Sun. The galactic coordinate system as well as the horizontal coordinate system are used. Furthermore, the application of different time systems, such as the Julian Date and the Universal Time, is necessary. A more detailed description on coordinate and time systems as well as calculating ephemerides can be found in Ref. [92].

A Brief Introduction to Atmospheric Refraction

A common problem in astronomy is that arriving rays of light are changing their direction, when entering Earth's atmosphere. As a result of this phenomenon, called atmospheric refraction, the apparent coordinates of a given point change on the celestial sphere. To be more precise the refraction R is defined by

$$R \equiv z - z', \tag{3.17}$$

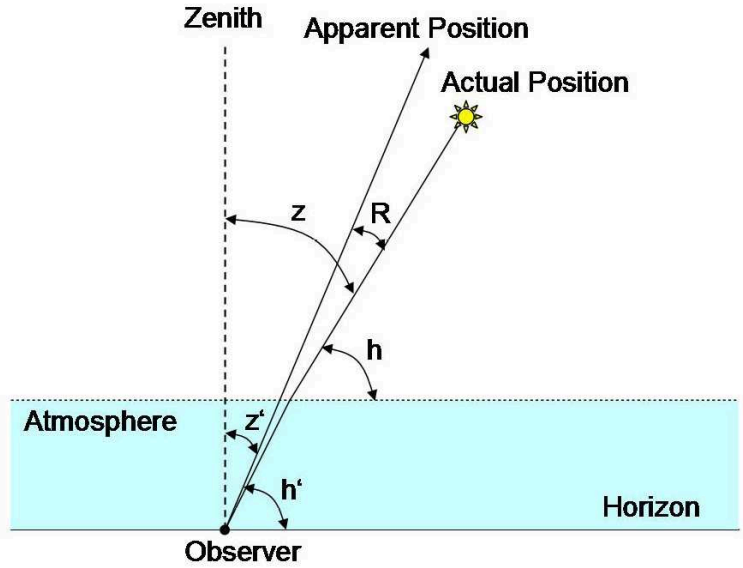

Figure 3.7: Atmospheric refraction. h' denotes the apparent altitude, while h stands for the true height above the horizon. z' and z are apparent and true zenith distance respectively. The refraction is marked by R. The incoming ray is bent towards the surface [92].

where z is the true zenith distance, while z' is the apparent one. Equivalently, one can consider the true and the apparent altitude above the horizon, h and h' respectively, to determine the refraction:

$$R \equiv h' - h. \tag{3.18}$$

Equation (3.17) and (3.18) are equivalent since $z' = 90°\text{-}h'$ and $z = 90°\text{-}h$.
If the density of the atmosphere is decreasing with altitude, as it is for Earth, an incoming ray will be bent towards the surface (see Fig. 3.7). The apparent reduction of the zenith distance depends on the length of the way through the atmosphere and therefore, the refraction is large for objects close to the horizon ($z = 90°$), namely about 0.6°, and decreases for positions closer to the zenith ($z = 0°$), where it reaches the value zero. Thus, if the Sun has to be filmed close to the horizon, considerable correction for refraction is necessary.

Furthermore, the refraction R depends on various factors besides the zenith distance, such as atmospheric conditions, geographic latitude and altitude (height above sea level). Several look-up tables exist giving the values for refraction under specific conditions, see for example Table 3.1. The exact value of the refraction depends on the refractive index n and thus on the temperature T [K] and the atmospheric pressure p [hPa] (both at the place of observation).

The atmospheric refraction can be calculated in degree by using the following formula [92]:

$$R = \frac{p}{60 \cdot T} \left\{ 3.4303 \left[z' - \arcsin(0.9986 \sin(0.9968 z')) \right] - 0.0112 z' \right\}, \tag{3.19}$$

Table 3.1: Refraction as function of height above horizon [92].

h'/degree	R/degree	h'/degree	R/degree	h'/degree	R/degree
0	0.610	5	0.171	50	0.014
1	0.427	10	0.092	70	0.006
2	0.319	20	0.046	90	0.000
3	0.250	30	0.029		

where z' has to be inserted in units of degree and the factor 1/60 results from a unit conversion of angular minutes to degree[8]. A change in temperature of ± 5 K and a simultaneous variation of the pressure of the order 3%, will thus change the refraction by less than 5%. If observing for example the Sun between 5° and 8° above the horizon, which corresponds to a time span of about 15 minutes, no such big changes in temperature, pressure and thus refraction are expected.
For heights above 5°, a more simple approximation exists:

$$R = \frac{(1/60)^\circ}{\tan(h')}. \tag{3.20}$$

It needs to be considered that the precision of this approximation might not be good enough, however. For example, at a height above the horizon of 5° assuming a possible difference in temperature of 5 K and a variance of the pressure of 3%, the approximation might differ by up to 25% (almost 0.04°!), if compared to the result obtained when considering T and p in Eq. (3.19). This discrepancy decreases rather fast with increasing height above the horizon. Concluding, it is possible to say that if high precision is needed, it is essential to consider the temperature and the pressure at the place of observation. This is, for example, the case for the CAST experiment, when an optical crosscheck of the tracking is performed. More details will be given in the following chapter.

[8] 1 degree corresponds to 60 angular minutes or equivalently to 3600 angular seconds ($1^\circ = 60' = 3600''$).

Chapter 4

The CAST-Experiment

The CERN Axion Solar Telescope (CAST), which is situated at the LHC[1] Point 8 of CERN[2] (see Fig 4.1) will be presented in this chapter. As an axion helioscope, CAST aligns a transverse magnetic field with the solar core to allow axion-to-photon conversion via the Primakoff effect. In order to obtain enough statistics, the time of magnet axis and Sun in line should be as long as possible. Thus, a tracking system was designed to follow the Sun very precisely. Firstly, the general setup of the experiment will be explained, including all its major components, namely the magnet, cryogenics and the tracking system. This will be followed by a description of the X-ray detectors, which form another important part of the experiment, because they are used to verify the appearance of a photon from the conversion. Then, a closer look at the solar filming, an independent crosscheck of the tracking system, will be taken since this is the subject which was to be improved in the course of this thesis. Finally, an overview will be given for the two phases of the CAST experiment and accomplished results of the first one will be presented.
As discussed in Chapter 3.2, in order to be sensitive to different axion masses, the coherence condition has to be fulfilled over the length of the magnetic field. With vacuum inside the magnet, CAST is able to detect axions up to a mass of about 0.02 eV. This follows from Equation (3.9) with the values for the magnetic field B and the magnet length L in this experiment ($B = 9$ T, $L = 9.26$ m). For higher masses, the coherence condition cannot be satisfied anymore in vacuum, but it is possible to restore it by inserting a buffer gas inside the magnet pipes. Different gas pressure settings allow then to reestablish coherence for distinct axion masses, because the effective photon mass depends on the gas pressure only (see Sect. 3.2.1). For the CAST experiment, this means sensitivity up to an axion mass of 0.82 eV. Summarizing, CAST is foreseen to consist of two phases:

Phase I Exploration of the mass region up to 0.02 eV by observing axion-to-photon conversion in evacuated pipes.
Phase II Extension of the mass range up to 0.82 eV by using a buffer gas with various pressure settings in the magnet pipes.

[1] Large Hadron Collider
[2] Conseil Européen pour la Recherche Nucléaire

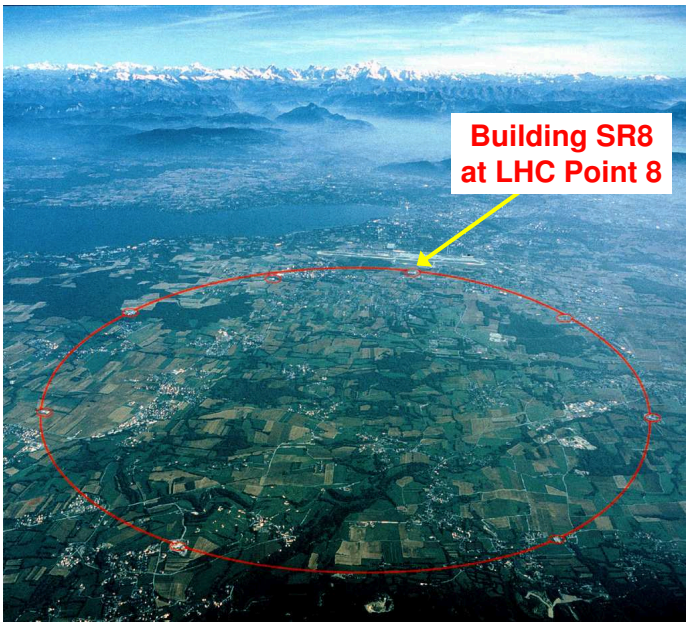

Figure 4.1: Location of CAST at the LHC Point 8 in Ferney-Voltaire, France [CERN].

4.1 The Experiment

4.1.1 The Magnet and Cryogenics

For CAST, a decommissioned LHC superconducting test magnet (see Fig. 4.2) forms the basis of the experiment and functions as an axion telescope. This first generation of the bending magnets has two straight bores. Each bore of the twin aperture magnet has a cross-sectional area $A = 14.5$ cm^2. The provided nominal field is 9 T over a length of 9.26 m [95]. More details can be seen in the technical drawing of the magnet used in CAST (see Fig. 4.3).
The operating temperature of the magnet is 1.8 K. A current of 13300 A is necessary in order to reach a field of 9 T. Thus, a complete cryogenic setup is required to provide the superfluid helium needed. The Magnet Feed Box (MFB, see Ref. [96] for a detailed description) is fixed on top of the magnet towards its sunset end, while the other end is closed by the Magnet Return Box (MRB). Flexible transfer lines for the helium and the quench recovering system allow movement of the whole structure. The "Potence", a movable gibbet, fulfills the same purpose for the power supply lines[3].
A quench is an interesting, even though in most cases disturbing[4], phenomenon connected

[3]This structure persistently caused trouble and had to be watched closely by shift workers during magnet movement periods, i.e. solar tracking, grid measurements, movements to parking position and so on.

[4]Some data taking runs were lost due to real and fake quenches. The latter ones were triggered by false warning signals monitored to protect the setup in case of a real quench.

Figure 4.2: The CERN Axion Solar Telescope in the experimental area. The magnet (blue) is borne on a platform (green), which is supported on the right hand side by a turntable (olive green) allowing horizontal movement, while it is carried by two screws at a girder (yellow) for enabeling vertical movement on the other end (left in image) [94].

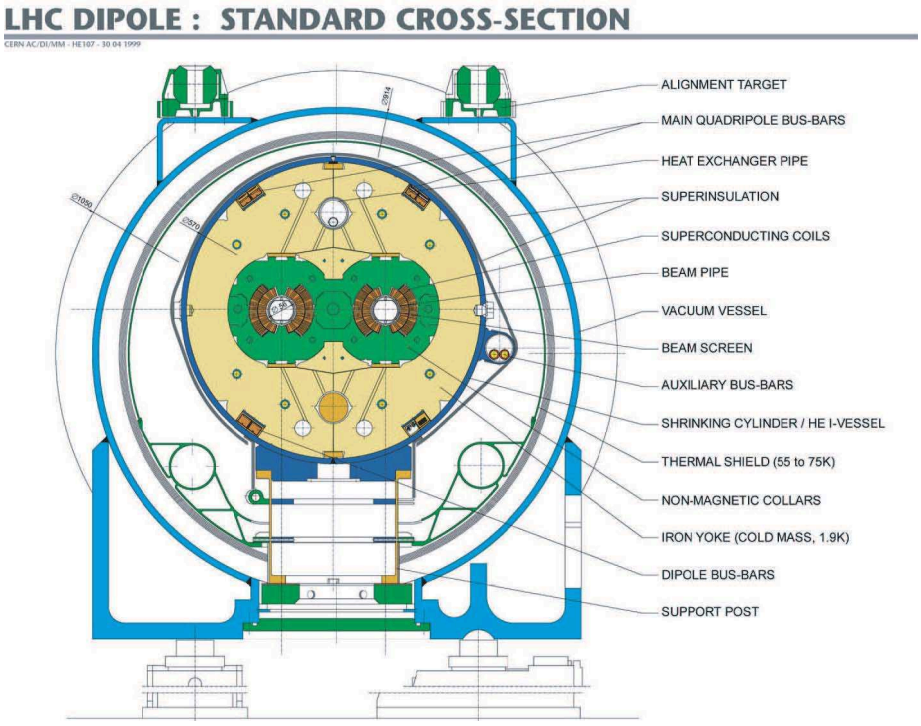

Figure 4.3: Cross-section of a twin-aperture LHC dipole prototype magnet with two straight magnet bores [CERN].

with superconducting magnets. It is the sudden change from the superconductive to the normal-conductive state, i.e. an electric resistivity occurs. Sometimes the temperature increases locally due to small fluctuations or friction, and thus the magnet loses its superconductive properties. This will cause further warming due to the occurring resistance. A rapid increase in pressure is the result. This absolutely requires to have a protection system in order to safeguard the cryogenic plant as well as the magnet itself. The helium is generally recovered, but if certain safety limits are reached or even exceeded the helium is released in order to prevent further damage.

4.1.2 The Tracking System

Two major challenges had to be faced, when implementing the tracking system, which enables the axion helioscope to follow the Sun: A system to move the whole experiment of over 40 tons and a reliable software to determine where to put the magnet and actually direct it to go to the required positions.

Hardware

Mechanical Setup The magnet described in Sec. 4.1.1 is mounted on a platform, which is composed of two strong metallic supports. The reason for choosing such a setup is to allow movement of the whole structure in horizontal as well as vertical direction. This allows an alignment of the magnet axis with the Sun for the longest time possible, and thus data taking time is maximized. In turn, this increases the amount of available statistics for data analysis.
The first part of the support for the platform (yellow girder on the left side in Fig. 4.2) is fulfilling two tasks. First, it moves the magnet along special rails on the floor for an angle of about 80° in azimuthal direction and, in this way, it provides guidance to the platform. Secondly, it is moving the magnet up and down. This is done by means of two screws attached to the support. On the other side of the magnet, where the most weight (close to 40 tons due to the cryogenic MFB) is located, a turntable forms the second support of the magnet platform allowing it to rotate horizontally (right side in Fig. 4.2). The total range of movement that can be reached with this setup is $\pm$ 40° in horizontal and $\pm$ 8° in vertical direction. The inclination of the magnet is restricted to this latter value due to mechanical and cryogenic constraints created by the magnet's internal setup. Consequently, the magnet can be aligned with the solar core for approximately 1.5 h during sunrise and for the same period of time during sunset every day. In the course of one year, this results in a total alignment time of more or less 50 days, if the horizontal range of possible movement is considered as well.

Motors and Encoders The platform is moved by two motors (one for horizontal, the other for vertical movement), which are connected to two encoders. The software guiding the motors/encoders will be described in more detail in the following paragraph. It should be mentioned that emergency stops were implemented for all directions of movement in order to protect the complete experimental setup from damage. These stops are hardware

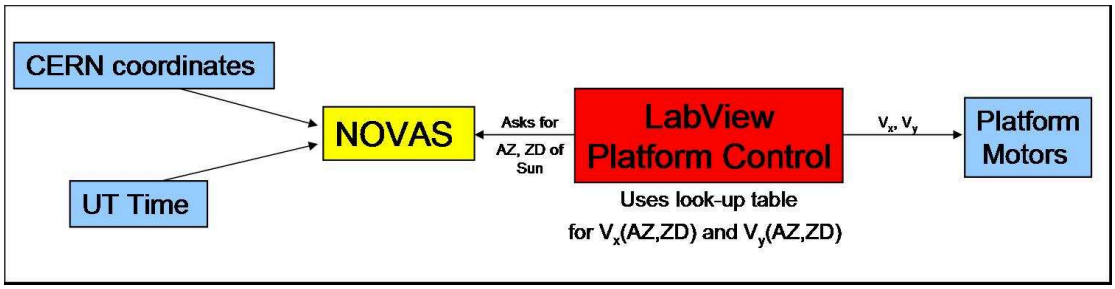

Figure 4.4: Operation principle of the NOVAS-based tracking software [97]. With the Universal Time as well as the coordinates of the experiment given, NOVAS calculates the azimuth (AZ) and the zenith distance (ZD) of the Sun. The LabView Platform Control converts AZ and ZD into encoder values, which then guide the motors. For this, look-up tables obtained with the help of the EST division are used.

switches as well as software limits, both meant to prevent the magnet from tilting too much or derailing while moving.

Software

Tracking Software and Logging of Data The tracking software performs two major tasks: it is guiding the magnet's movement and, in addition to this, it is writing relevant information[5] to logfiles utilized for data analysis later on. Fig. 4.4 points out the general operating principle of the software directing the motion of the magnet. The elaborate program is written in LabView and based on NOVAS[6], a package of subroutines to compute various astrometric quantities offered by the U.S. Naval Observatory [90]. NOVAS reads in the UT Time as well as the coordinates of the experiment[7] at CERN. Then it calculates the azimuthal angles (AZ) and the zenith distances (ZD or z) of the Sun for the minute to come. Following this, the software transforms these values to the corresponding encoder numbers by using look-up tables for the encoder values V_x(AZ, ZD) and V_y(AZ, ZD). The motors are then guided to move the magnet to this position. Shift workers can check current parameters on the user interface (see Fig 4.5) and control the experiment via the program.

Two inputs are especially crucial for an accurate result of the software calculations: the UT time and the look-up tables. Time synchronization of the host PC's clock with two CERN time servers is continuously performed to the order of 1 ms. The look-up tables were obtained with the help of the EST[8] division at CERN. Altogether, ninety magnet positions were measured and put down in encoder values by the surveyors. Thus V_x(AZ, ZD)-V_y(AZ, ZD) tables were built with a high accuracy of 0.001°. Missing interim values in the tables caused gaps, which were filled, however, by using "Hardy's multiquadratic", a spline interpolation method. The accuracy is always better than 0.01°, typically, however, around 0.002° [98].

[5]Examples for such pieces of information are ambient temperature and pressure.
[6]Naval Observatory Vector Astrometry Subroutines
[7]46°15′ N, 6°5′ E, 330 m above sea level.
[8]Engineering Support and Technology

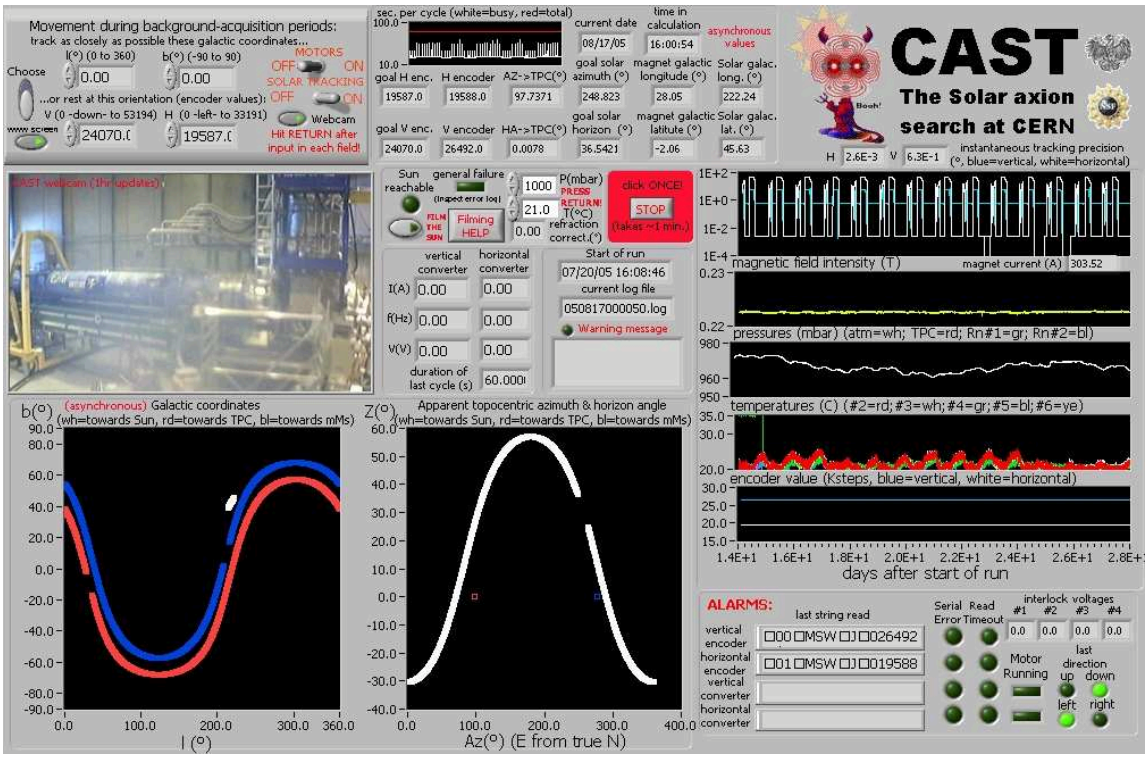

Figure 4.5: Snapshot of the user interface on the tracking PC in the control room of CAST. In the upper left corner, the magnet movement is controlled: motors and tracking mode can be switched on, parking position or galactical coordinates can be entered. Below this, an hourly updated webcam image of the experiment can be seen. At the bottom left, the solar and magnet movement are shown in Galactic coordinates as well as in apparent topocentric azimuth and horizontal angle. The right side of the screen is dedicated to monitor different parameters such as the magnetic field, pressure and temperature. In the lower right corner, alarms, errors and movement information is given. Access to the filming mode is given in the central part of the user interface.

Table 4.1: Summary of possible error sources of the solar tracking precision [3, 97–99].

Source of Error	**Typical Value**	**Maximal Value**
Astronomical Calculations	0.002°	0.006°
Uncertainty of Coordinates (CERN)	$\approx 0.001^\circ$	
Clock Time	$\approx 0^\circ$	
Grid Measurements (0.02 mm precision)	0.001°	
Interpolation of Grid Measurements	0.002°	$< 0.01^\circ$
Horizontal Encoder Precision	$\approx 0.0014^\circ$	
Vertical Encoder Precision	$\approx 0.0003^\circ$	
Perfect Linearity of Motor Speeds	$< 0.002^\circ$	
TOTAL	$< 0.01^\circ$	

In Table 4.1, a summary of possible errors is given and it becomes obvious that CAST's accuracy is designed to be very good [3, 97–99]. Nevertheless, twice a year an additional, independent crosscheck of the tracking system can be performed. This test, the filming of the Sun, will be described in detail later in this chapter (see Sect. 4.3).

The Slow Control In the middle of 2003, an additional independent slow control was designed to be used, because it became necessary to monitor and log more parameters for controlling the system as well as for analyzing the data. From July 2003 on, more information, such as the status of the valves, the load on each of the screws and the position of the magnet in encoder values, was recorded. Furthermore, an alarm system was established to keep important informations for the operation of the experiment under surveillance and alert people in charge, if necessary. Like the tracking software, the slow control (SC) is written in LabView.

4.2 The Detectors

In order to detect the X-ray photon originating from the axion-to-photon conversion in the magnetic field, several low-background detectors are used. Their sensitivity range is between 1 and 10 keV. A TPC (Time Projection Chamber) is located at one end of the magnet, covering both magnet bores, in order to detect photons from sunset axions. On the other side of the setup, where sunrise axions are searched for, two more detectors are mounted. One bore is covered by a MICROMEGAS (MICROMEsh GAseous Structure) detector, while at the other a CCD (Charge Coupled Device) detector is looking for photons from axions. A special feature of the latter device is an X-ray mirror telescope added in between the magnet and the detector to focus the incoming photons on the sensitive chip. All detectors are taking data during about 1.5 hours per day, either in the morning or in the evening, depending on the side they are mounted on. During the remaining time, background measurements are performed and thus, the background for the individual detectors is measured with an exposure time that is approximately 10 times higher than

the one for data taking.

4.2.1 The Time Projection Chamber

The TPC used at CAST, which is taking data during sunset runs, is a conventional type of this kind of three-dimensional tracking detectors, often also referred to as *electronic bubble chamber*, due to the information it is able to provide. The principle detection mechanism of a TPC combines ideas from both Multiwire Proportional Chambers (MWPC) and drift chambers. The central part is a gas-filled volume, where incoming particles interact and thus produce free electrons. These drift towards a net of anode wires and produce an avalanche due to the strong electric field. This increases the strength of the signal there. The first coordinate is obtained from the firing anode wire, the second from the signal induced on the cathode pads, while the third one is derived from the drift time.

Technical Details

The dimensions of the TPC's conversion volume are $10 \times 15 \times 30$ cm^3, where the drift region of 10 cm is parallel to the axis of the magnet and the area of 15×30 cm^2 is perpendicular to this direction. The volume is filled with a mixture of 95% Argon (Ar) and 5% Methan (CH_4) at atmospheric pressure, allowing essentially total conversion ($> 99\%$) of X-ray photons[9] up to 6 keV. In more detail, the basic setup of the detector, as it can be seen in Fig. 4.6, consists of a drift electrode made of aluminum close to the magnet as well as an arrangement of 3 planes:

- The anode plane at +1.8 kV with 48 wires (having a diameter of 20 µm each)
- Two cathode planes at ground with 96 wires (having a diameter of 100 µm each)

The distance between two adjacent wires of the same plane is 3 mm, the gap between the first cathode and the anode plane is 3 mm, while the one between the anode and the more distant cathode plane (with respect to the drift electrode) is 6 mm.
The predominant material used for the chamber is plexiglass (low natural radioactivity), some metallic parts and pieces of other materials, such as the wires, the PCB[10] holding the wires and the screws which keep the chamber together, could of course not be omitted.

Windows and Differential Pumping

The TPC is connected to each magnet bore through a thin window (3 or 5 µm of mylar on a metallic strongback). This is necessary, because of the 1 atm pressure difference between the gas in the detector volume and the vacuum inside the magnet. In order to decrease gas leaks towards the magnet and to protect the windows themselves, a differential pumping system was added in 2004.

[9] For higher photon energies, the conversion efficiency decreases reaching 50% for 11.5 keV.
[10] Printed Circuit Board

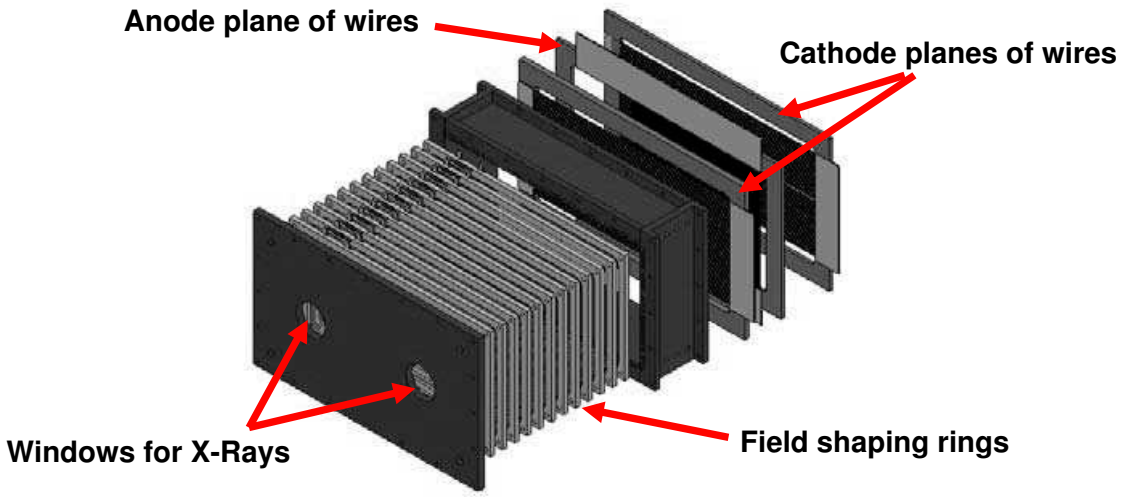

Figure 4.6: Technical Design of the TPC [100]. The X-ray photons from axion-photon conversion enter the detector through two windows connecting the two magnet bores and the TPC. The two cathode planes (at ground) as well as the anode plane (at +1.8 kV) can also be seen in the drawing.

Figure 4.7: TPC with shielding added before data taking runs in 2004 [100].It is possible to see all layers of the shielding (copper box, lead, cadmium and polyethylene).

Active and Passive Shielding

Active and passive shielding were added as well in 2004 to reduce the background of the detector. The passive part consists of several layers (from inside to outside): copper (5 mm), lead (2.5 cm), cadmium (1 mm), polyethylene (2.25 cm) and a plastic covering to flush the interior with pure N_2 gas (see Fig. 4.7). The shielding is able to stop various passing particles. Furthermore, an active part (veto) was installed to reject muons inducing background in the TPC. The background between 1 and 10 keV is now a factor 4.7 below the one of the TPC without any shielding.

Calibration and Data Taking

Four times a day, the TPC is automatically calibrated using a low-energy X-ray source. Data was taken in 2003 and 2004, while the amount of the latter year was five times larger than the data taken in the preceding year. Overall, the total amount of data acquisition in 2003 and 2004 together was 3408 h for background and 203 h for tracking measurements. The advantages of the TPC used at CAST are obvious:

- Stable performance due to robust and well-known conventional design
- Low background due to implemented shielding

4.2.2 The MICROMEGAS Detector

The second gaseous chamber used at CAST is smaller than the TPC and has an innovative MICROMEGAS readout [101]. It is attached to one of the two magnet bores, such that the detector is facing the rising Sun. Unlike the TPC, the MICROMEGAS does not utilize a plane of wires but a micromesh to separate the two distinguished regions. The principle of operation such a detector uses is shown in Fig. 4.8.
After passing the drift electrode, the incident particle will produce ion-electron pairs within the conversion region, which is separated from the amplification gap by a grid: the micromesh. In order to reach a high electron transmission to the amplification region, a voltage of up to 500 V is applied. An avalanche process will occur after the mesh is passed and the grid will keep the ions produced in the avalanche from re-entering the conversion region. It so collects the ions, which provides the first readout (utilizing a Flash ADC), while the electrons continue their way to the anode, where they are readout on a novel structure of x-y strips.

Technical Details

The frame of the detector used to search for photons from Primakoff conversion is made of plexiglass. The electrodes are attached to it. The conversion region is 25 mm thick, the amplification gap 50 µm. The mesh consist of 5 µm copper, its holes have a size of 25 µm with a separation distance of 50 µm. For the readout, there are 192 x-strips and the same amount for the y-direction. The pitch is $\approx$ 350 µm. As gas, a mixture of argon with 5% of isobutan is used.

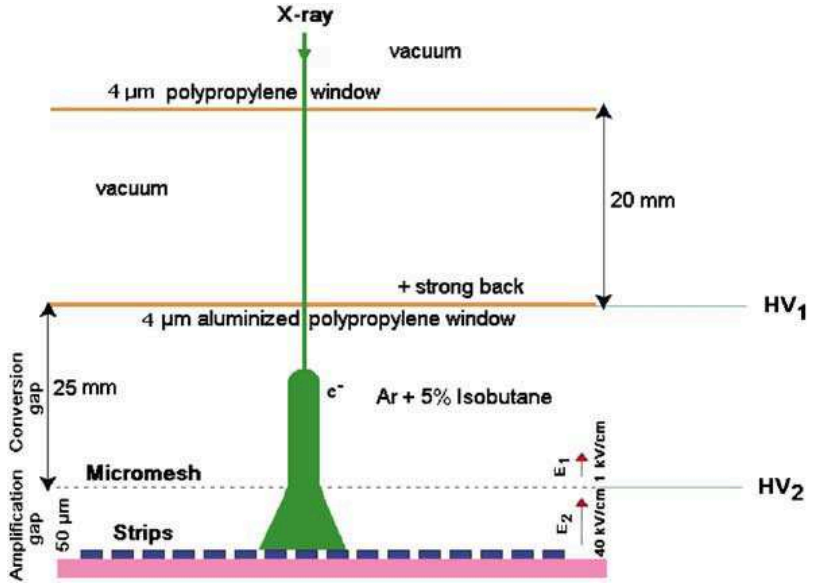

Figure 4.8: Schematic view of the MICROMEGAS detector used at CAST. The conversion gap of 25 mm is divided from the amplification region (about 50 µm) by a micromesh. For the signal readout x-y strips are used (bottom) [3].

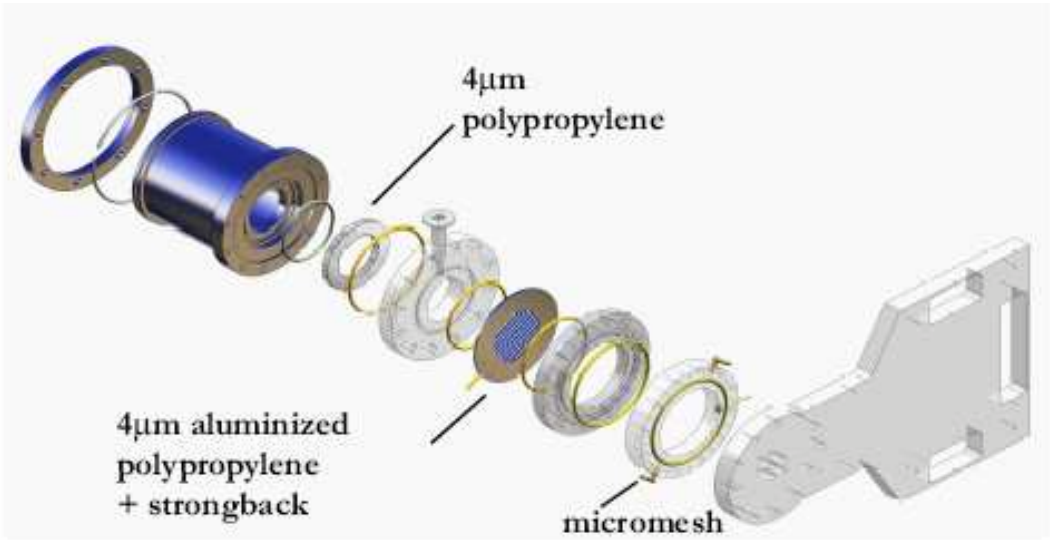

Figure 4.9: Blown-up view of the Micromegas detector at the CAST experiment. All components are clearly separated. The attachment to the magnet was accomplished via an aluminum tube of about 1 m length and a flange. A direct installation at the bore was not possible, because everything (CCD, X-ray telescope, Micromegas) had to be arranged, such that it fitted on a platform together [3].

Windows and Differential Pumping

Being a gaseous detector, two windows (polypropylene, 4 μm each, one is aluminized and serves as cathode) are needed to connect the MICROMEGAS with the magnet volume (vacuum), while aiming for maximal transparency for low energy X-rays as well as minimal leaking. As with the TPC, differential pumping is applied to achieve the latter goal. A blown-up view of the detector is shown in Figure 4.9.

Calibration and Data Taking

In addition to daily data taking, calibration and pedestal[11] runs were performed by workers on morning shift. Altogether, the amount of usable data taken were 75 h (178 h) of tracking and 750 h (2404 h) of background data in 2003 (2004), which leads to a total of 253 h following the Sun and 3154 h acquiring non-tracking data. The major advantages of Micromegas are various:

- High stability and efficiency
- Good resolution of both energy and position
- Fast response

A detailed detector study of the Micromegas at CAST and the analysis of the data obtained in 2003 and 2004 by this detector can be found in Ref. [3].

4.2.3 The X-ray Telescope and the pn-CCD Detector

The most sensitive detector setup at the CAST experiment consists of a focusing X-ray mirror telescope and a Charge Coupled Device (CCD, see Fig. 4.10). It is situated at the remaining fourth end of the two magnet bores. Both parts were originally designed as prototypes for X-ray astronomy [102,103]. This system takes data during morning runs: the telescope focuses the incoming photons from axion conversion to a spot of approximately 6 mm^2 on the CCD. Due to the interaction of the X-rays with the silicon atoms of the pn-CCD, electrons and holes are created and kept separated by strong electric fields. The electrons are captured in small potential wells below the surface and can be transferred to the readout chip by being shifted from one well to the next, conserving the charge distribution pattern achieved in the ionization process (see Fig. 4.11). A more detailed description of pn-CCDs in general is given in Ref. [104] and references therein.

The X-Ray Telescope

The focusing device used at CAST is a Wolter I type X-ray mirror telescope, which was a prototype of the German X-ray satellite mission ABRIXAS[12] [102, 105]. It consists of an arrangement of 27 nested parabolic and hyperbolic mirror shells made of gold coated nickel

[11] Pedestal runs are equivalent to the mean value of the charge measured by the strips without real triggers given. Thus they are important for the correct readout of the strips [3].

[12] A BRoad band Imaging X-ray All-sky Survey

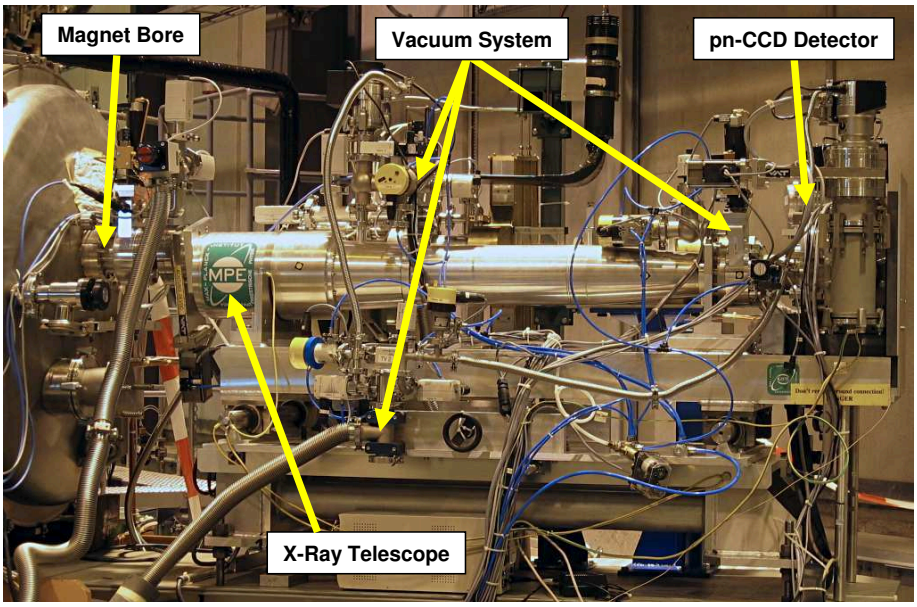

Figure 4.10: The X-ray telescope and the pn-CCD at CAST. They are mounted to one bore (left) of the superconducting magnet. The telescope is situated inside the tube visible in the middle of the picture, while the CCD detector is attached to the end of the tube (right). The vacuum system can be seen as well [109].

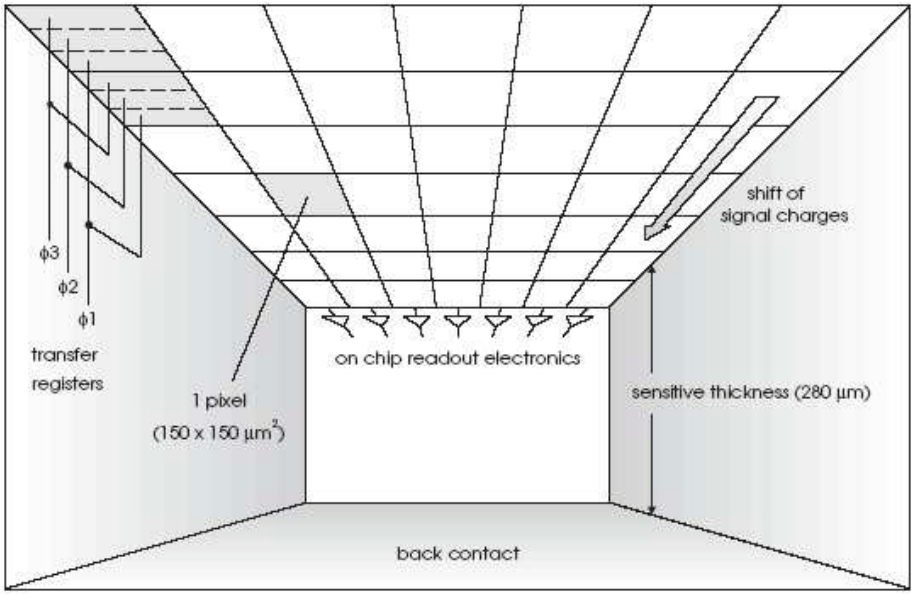

Figure 4.11: Inside the pn-CCD. X-Rays hit the device from the backside (here: bottom). The electrons are captured in potential wells and can then be transferred to the readout [104].

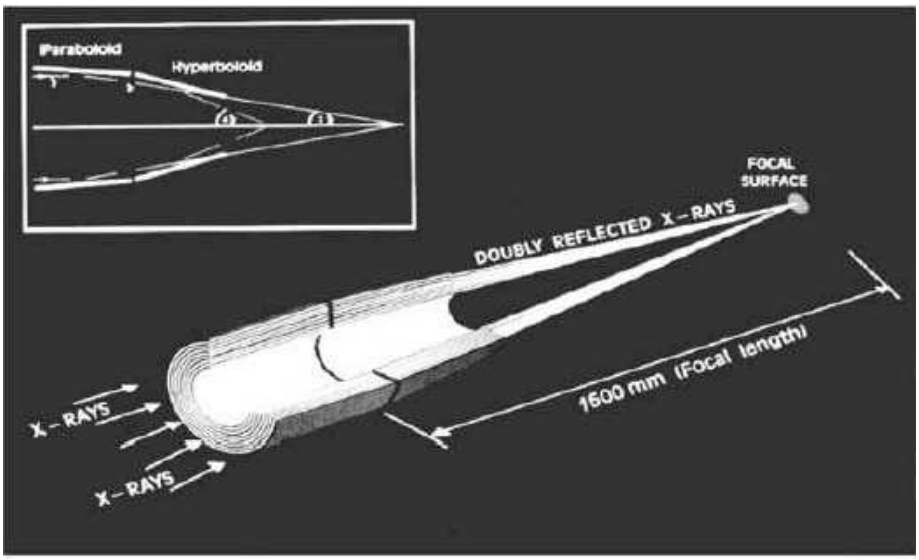

Figure 4.12: Schematic view of the Wolter I type telescope used at CAST. One sector of the telescope is used since the magnet bore diameter is 43 mm only. The functional principle is based on [108].

(see Fig. 4.12 and Fig. 4.13). The diameter of the shells varies from 76 mm to 163 mm from the innermost to the outermost shell, respectively. A cobweb-like structure supports the shells (see Fig. 4.13). Only one of the six sections is used at CAST, because the diameter of the magnet bore is 43 mm only. The focal length of the telescope is 1.60 m and it is operated under vacuum conditions at a pressure of less than 10^{-5} mbar to prevent the mirror shells from contamination[13] [106].
By focusing the photons coming from the magnet to a small spot, the signal to background ratio is enhanced by a factor of 200 (the signal to noise ratio by a factor of 14), but at the same time a high precision of the tracking[14] is absolutely essential in order to achieve good results using the telescope in combination with the CCD detector at CAST [107].

The pn-CCD

The pn-CCD detector is located in the focal plane of the X-ray telescope. It is a prototype developed for the XMM-Newton[15] mission of ESA[16] [104]. The performance of the detector was optimized to fulfill the demands of low background application by adding passive shielding (copper and lead, see right image in Fig. 4.14) as well as by improving the software background rejection (based on a pattern recognition algorithm). For a summary of specific

[13]The composition of the residual gas is an additional critical factor here.
[14]The desired tracking precision has been the subject to many lively discussions. In order to get the image blurred over not more than 4 pixels on the CCD chip (which is already quite a lot), the accuracy should be always better than $1.2'$, i.e. 0.02° [106].
[15]This name derives from the X-ray Multi-Mirror design used and is meant to honor Sir Isaak Newton. Formally, it was called High Throughput X-ray Spectroscopy (HTXS) Mission.
[16]European Space Agency

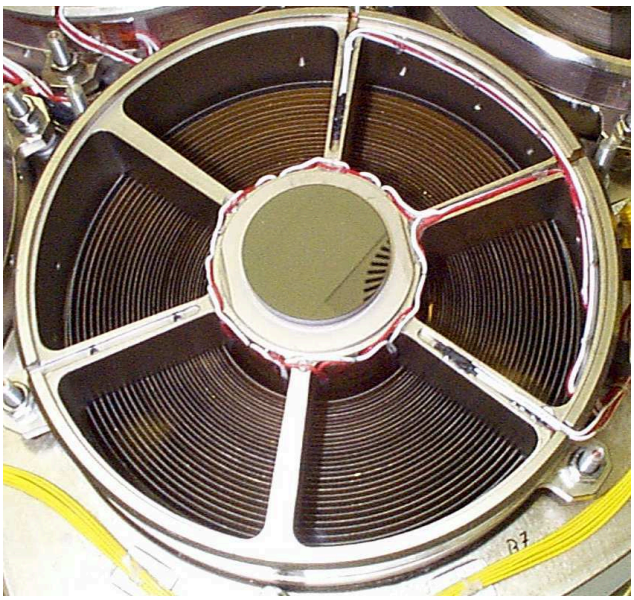

Figure 4.13: Front view of the mirror system with cobweb-like support for the 27 mirror shells. The diameters vary from 76 mm up to 163 mm [109].

detector parameters see Tab. 4.2.
The CCD chip with a sensitive area of 2.88 cm^2 (see left image in Fig. 4.14) is larger than the expected image of the solar core (0.2 $R_\odot$, which corresponds to approximately 19 pixels= 2.83 mm), where most axions are expected to come from. Due to this fact, it is possible to measure a potential signal from axion to photon conversion and background simultaneously using the surrounding area. Systematic errors can thus be reduced. The CCD is operated at $-130°$ C using a cooling mask in vacuum.

Calibration and Data Taking

Every morning before solar tracking, a calibration with a ^{55}Fe source is performed by the shift personnel. Data was acquired in 2003 and 2004. While the analysis for the first year is already completed, evaluation of the latter one is still ongoing. The total amount of data taken was 2956 h for background and 300 h for tracking measurements. The major advantages of this detector setup are:

- High quantum efficiency
- Improvement of the signal to background ratio by a factor of about 200 due to focusing with an X-ray telescope
- Very good spacial and energy resolution

Table 4.2: Detector Parameters of the pn-CCD [109].

Detector Parameters	
Geometry	200×64 Pixels
Pixel size	150×150 µm^2
Sensitive Area	2.88 cm^2
Depletion Depth	280µm
FWHM	175 eV @ 6 keV
Efficiency $(1 - 7$ keV)	$> 95\%$
CCD Temp.	$-130°$ C
Cycle Time t_{int}	71.775 ms
Readout Time t_{read}	6.06 ms

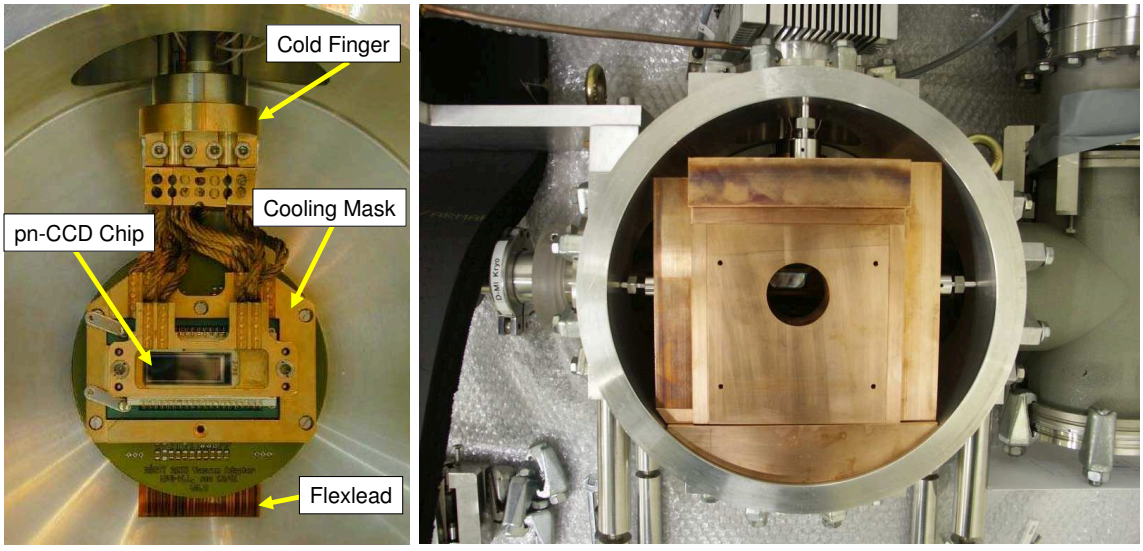

Figure 4.14: Left image: CCD chip with gold plated cooling mask, that is connected to a cold finger of a Stirling cooler device. Right image: Inner shielding components of the pn-CCD (lead and copper). An additional layer of lead outside the detector housing further reduces background. The vacuum components are attached on the right side of the vessel [109].

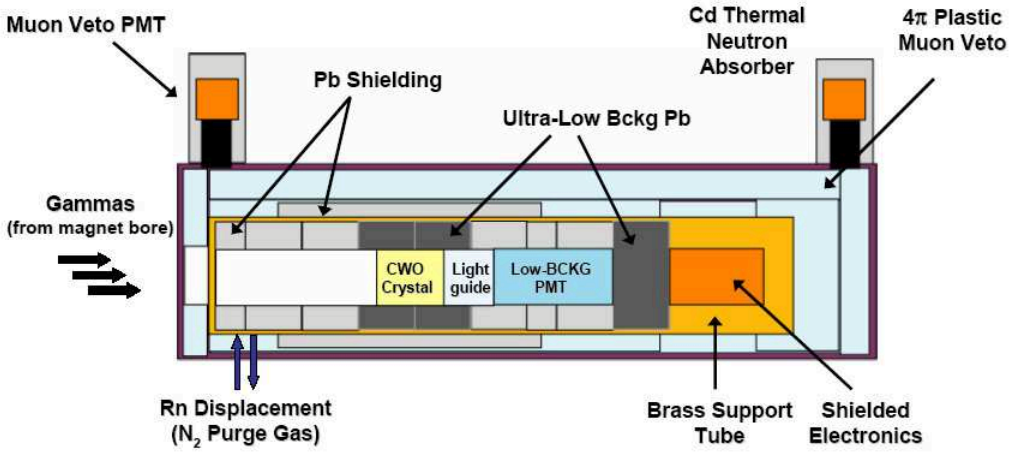

Figure 4.15: Schematic view of the High-Energy Calorimeter [110]. A large inorganic scintillating crystal ($CdWO_4$) of about 0.6 kg is used together with a low-background photomultiplier tube. An active muon veto and a borated thermal neutron absorber are shown as well here.

4.2.4 Addendum: The High-Energy Calorimeter

In 2004, a high-energy calorimeter was installed at CAST close to the MICROMEGAS . It was intended to search in parasitic mode for axions or axion-like particles of higher energies than the ones the three X-ray detectors are looking for. The sensitivity region for gammas induced by axions ranges from $\approx$ 100 keV up to $\approx$ 150 MeV. A schematic drawing of the 0.6 kg $CdWO_4$ (CWO) calorimeter is shown in Figure 4.15.

4.2.5 The Field of View

After having taken a closer look at the detectors, it is useful to consider the field of view (FoV) the magnet can provide, if its cold bore is considered to be the limiting optical element.
It can be calculated (see Fig. 4.16) using:

$$\alpha = 2 \arctan \frac{d}{L} \tag{4.1}$$

where α denotes the opening angle, i.e. the field of view, d is the bore diameter ($d = 43$ mm) and L the magnet length ($L = 9.26$ m). A fully illuminated FoV of approximately 0.53° can be achieved. Neither one of the detectors has its sensitive area directly attached to the magnet bores: For Micromegas an extension of > 1 m is used, while for the CCD the telescope separates the end of the magnet pipe from the sensitive area of the detector. For the TPC, the extension is shorter, but still its sensitive part is not directly at the magnet bore. Due to this fact, vignetting effects occur and the FoV of all detectors is therefore not fully illuminated.
If no telescope was used, the FoV of the full CCD chip, which is about 0.34°, would be

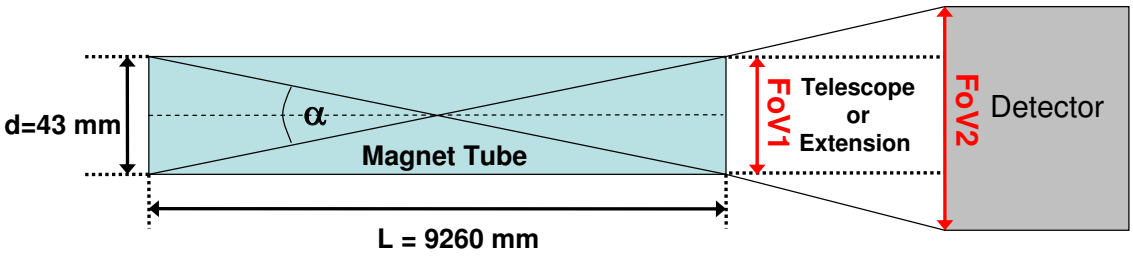

Figure 4.16: Field of View α of the magnet. FoV1 denotes the fully illuminated field of view, while for the detectors due to the distances between the bore and the sensitive part a partly vignetted field of view, FoV2, is obtained. α can be calculated and is about the size of the Sun (0.5°).

able to cover about 64% of the entire Sun ($\approx 0.53°$). The telescope, however, focuses the incoming converted photons to a spot with a diameter of about 19 pixel, i.e. a disk of 20% of the solar radius is imaged on the chip [106]. Thus, it should be stressed once more that a very high accuracy of the tracking system is essential, in order to be able to observe axions originating from the solar core (10-20% of the Sun). The precision has to be at least as good as 0.02°.

4.3 The Solar Filming

4.3.1 Filming at CAST: An Overview

When the tracking system was just about to be finished, first calls for an independent crosscheck of the tracking accuracy were voiced. The first suggestion to do this by using an optical instrument was made in July 2002. Basically, the idea was to cut a window in the wall of the experimental area facing northeast-east, align a camera with the axis of the magnet and directly film the Sun, while following it. One important thing to consider is refraction of light in the atmosphere, which does not occur for axions, since they do not noticeably interact with air. Consequently, two different versions of the tracking program were necessary: one should correct for refraction (while filming) and the other should not do so (while regular tracking).
Ever since the window was cut, the possibility to film the Sun twice a year, namely in March and September, was used six times up to the present day (Fall 2002, Spring and Fall 2003, Fall 2004, Spring and Fall 2005), although some difficulties were encountered. Bad weather conditions and trees blocking the view have been just two of the facts complicating the filming of the Sun.

4.3.2 The System to Film the Sun

The Filming Software

The version of the tracking software for filming can be accessed via the normal user interface of the tracking PC (see right part of Fig. 4.17). People on shift have to start it manually

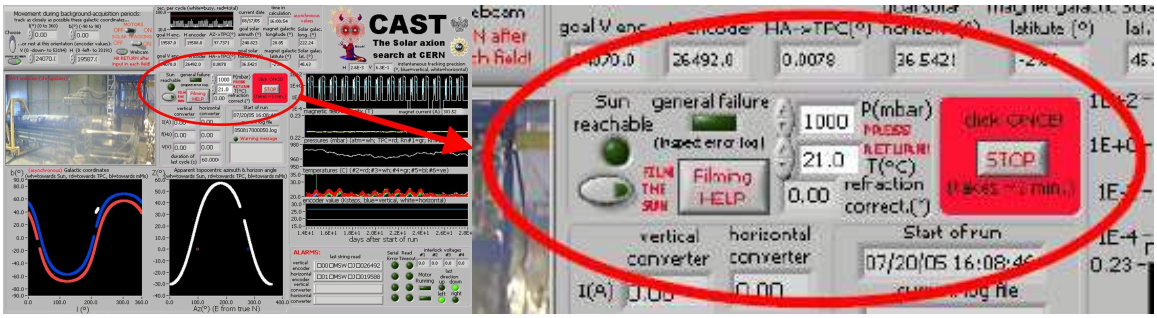

Figure 4.17: Filming software implemented in the tracking program (User Interface on tracking PC). If the Sun is within the range of movement of the magnet, a green light can be seen. Any occurring error will show up by a light as general failure. In order to activate the Filming Mode of the software, the "Film the Sun" button has to be pushed. The Filming Help button provides additional information on pressure and temperature, which have to be entered. If done so, the refraction correction is displayed and logged as well.

and insert the pressure p and temperature T for the location of the experiment, which are taken from the internet [111]. In addition to this, the zenith distance ZD is known, since it is calculated by NOVAS. So the aberration in the atmosphere can be taken into account in real-time, which means as a function of ZD, p and T. The atmospheric refraction correction can be predicted given this input with an error of less than 0.00025°, even when being close to the horizon at low altitudes [98, 99].

The First Setup

The setup for the filming of the Sun used until Spring 2005 was rather inventive. A webcam attached to a small optical telescope (see Fig. 4.18) was aligned with the magnet by means of fixing the telescope within a sphere. Having the same dimensions as the Taylor-Hobson spheres (TH-sphere[17], see left image in Fig. 4.19) used by the surveyors of the EST division at CERN, it was possible to align the optical axis of the setup with the magnet by the help of the geometers. A pointer was used in order to analyze the pictures of the webcam: it is checked if the tip of the pointer is in line with the center of the crosshairs installed within the telescope (see for example right image in Fig. 4.19).

4.3.3 A Chronology of Filming

Starting the Fun The first optical crosscheck was performed at the end of September 2002. Although many improvements were to come, this first approach already showed that the magnet was pointing towards the Sun and seemed to be well-centered.

Further Opportunities to Film In March and September 2003, the procedure was repeated and some limiting factors became more obvious. Beside the usual suspects causing trouble, such as the trees, the weather conditions, a girder in the window, and a helium

[17] A TH-sphere is a sphere of standard radius ($r = 1\ 3/4$ inch $\approx 44,45$ mm) with an illuminated center used in surveying, most of the time in combination with a theodolite.

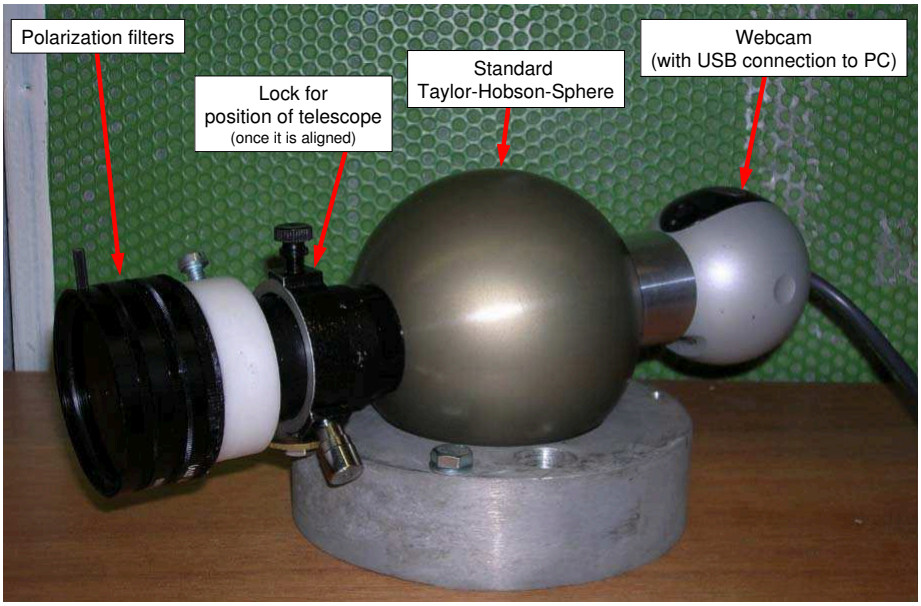

Figure 4.18: Picture of the complete setup used for filming the Sun until Spring 2005 consisting of an optical telescope fixed within a standard Taylor-Hobson sphere, a webcam attached to it and polarization filters.

tank outside the experimental hall, it turned out that the precision of the setup's alignment with the magnet axis was restricted due to the limited resolution of the webcam: The bright spot in the center of the observed TH-sphere was broadened considerably (see Fig. 4.19). An error of about 5 mm at a distance of approximately 5 m, i.e. an error in the angle of $\approx 0.05°$, resulted from this. Errors from the picture analyses are not included in this number. Unfortunately, the problem would remain as long as the webcam was used. But the good news were that, within this precision, the magnet was aiming at the solar center in March 2003, which was a very satisfying result. As a special feature, a movie of this filming was produced and can be watched online [112]. During Fall of the same year, some problems occurred when analyzing the pictures. An offset of the hairline center was observed, implying a possible displacement of as much as 30% of the solar radius for the magnet alignment to the Sun. As a possible cause a hysteresis[18] of the magnet movement system was under suspicion. However, reanalysis of the pictures showed that the chosen treatment of the pictures strongly influenced the outcome. The position of the crosshairs depended strongly on the image chosen as a reference for comparison with the Sun picture. Also by varying the brightness, one could change the apparent shape of the Sun considerably, hence "proving" almost any result. Finally, it turned out after further careful analysis that CAST was still pointing at the Sun. Nevertheless, improved optics were desirable for better accuracy.
One more filming was performed with the same setup in September 2004, after missing

[18]Hysteresis here means the inability to return to the same position in space with the magnet by going back to the same encoder values.

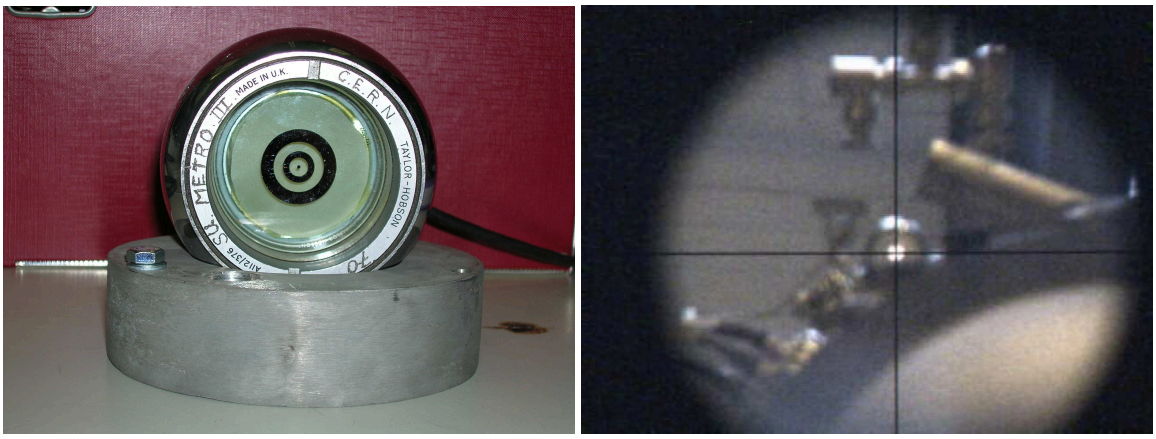

Figure 4.19: Left image: Taylor-Hobson-Sphere (TH-sphere) as it is used by surveyors. Right image: Alignment of the webcam/telescope with TH-sphere. It can be seen that the small spot of light in the center of the sphere is broadened due to the resolution of the camera.

out in March 2004, due to mechanical constructions in the experimental area. This time, however, a huge effort was made to put the camera in three different positions in order to find the best place for a new setup. It was possible to locate a position providing the clearest view and the longest time window for filming. The first position, situated on top of the magnet in front of the MFB, had to be slightly higher than in previous years, because the newly arranged TPC shielding was blocking the view of the webcam if mounted in the old position. Another platform was installed to one side of the experiment[19], allowing the camera to be put there at two different heights (see Fig 4.20 and Fig. 4.21). Analyzing the acquired pictures showed that, within the given precision, CAST was pointing at the Sun (see Fig. 4.22).

4.3.4 Outlook

Building on the experience gathered from previous filming sessions, a new setup was designed, improved and used from Spring 2004 on. The modifications made, performance of the new setup as well as the analysis of the data will be presented in the following chapters. An improvement of the filming system was crucial, since a reliable crosscheck of the tracking system with high precision was needed, due to the fact that a very good tracking accuracy is essential in order to ensure that the Sun is in the field of view of the detectors. Thus, the new setup was intended to prove for sure that CAST is pointing at the Sun. Before more details will be given, a short overview on CAST's achievements during its first phase and the current status of preparations for the second phase will be given.

[19]The two sides of the experiment, i.e. left and right of the magnet axis, are named after the site they are facing: Jura and the airport. The platform was installed on the Jura side, i.e. towards West.

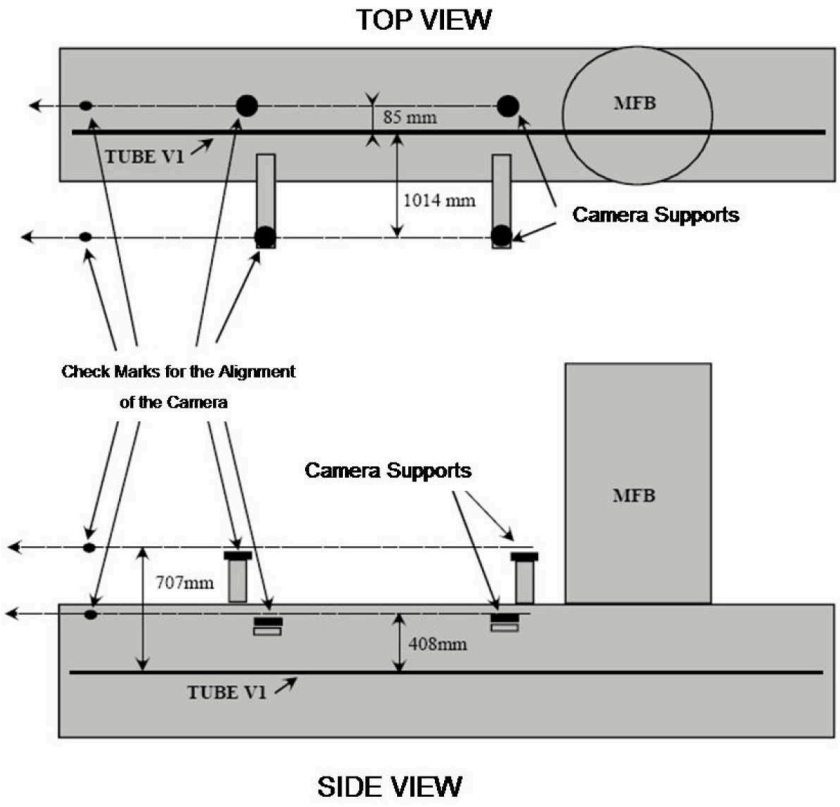

Figure 4.20: Positions of the optical setup during filming in September 2004. The first platform is on top of the magnet, while the second one is mounted towards the Jura side [Picture courtesy of the EST division at CERN].

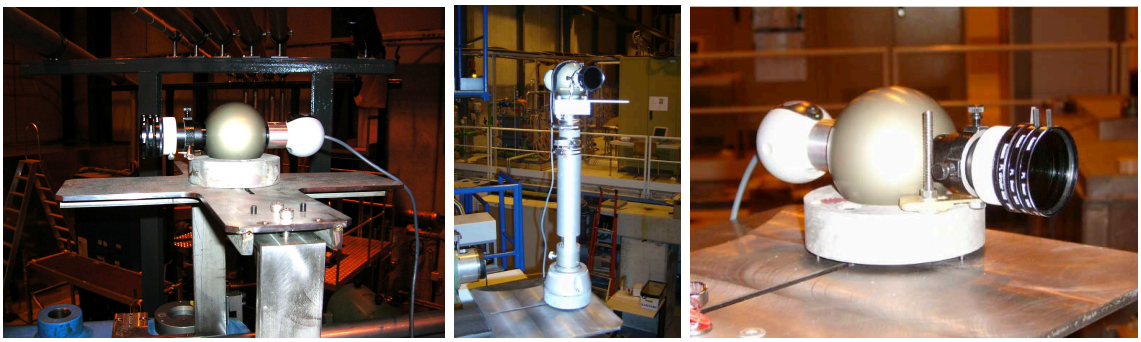

Figure 4.21: Left image: First position of filming the Sun in September 2004 on top of the magnet. Middle image: Second position towards the Jura side. A vertical extension of 50 cm is used. Right image: Third position. The camera is in the same place as the second position, but no vertical extension is used.

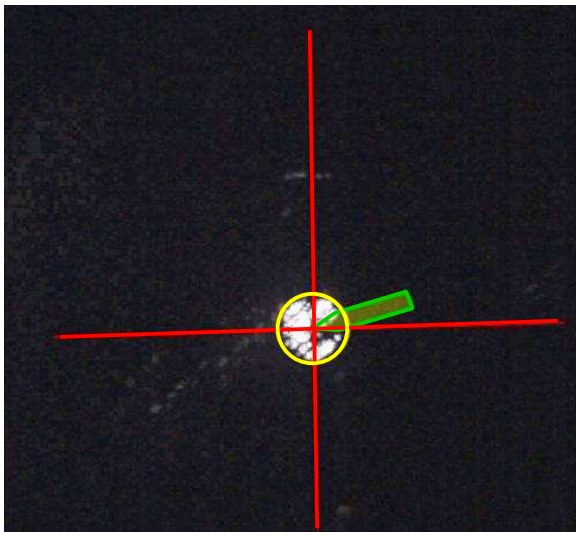

Figure 4.22: Result of the analysis performed in Fall 2004 by T. Papaevangelou. The precision is 3-5 mm/5 m, which corresponds to 0.03°-0.06°, i.e. 1.8′-3.6′.

Table 4.3: Data sets of the 2003 data taking period [69]

Data Set	Tracking Exposure (h)	Background Exposure (h)	$(g^4_{a\gamma})_{\text{bestfit}}$ ($\pm 1\sigma$ error) (10^{-40} GeV^{-4})	χ^2_{null}/d.o.f.	χ^2_{min}/d.o.f.	$g_{a\gamma}$(95%CL) (10^{-10} GeV^{-1})
TPC	62.7	719.9	-1.1 ± 3.3	18.2/18	18.1/17	1.55
MM set A	43.8	431.4	-1.4 ± 4.5	12.5/14	12.4/13	1.67
MM set B	11.5	121.0	$+2.5 \pm 8.8$	6.2/14	6.1/13	2.09
MM set C	21.8	251.0	-9.4 ± 6.5	12.8/14	10.7/13	1.67
CCD	121.3	1233.5	$+0.4 \pm 1.0$	28.6/20	28.5/19	1.23

4.4 First Results of CAST and Prospects

4.4.1 Phase I and its Results

Phase I started data taking in 2003 and concluded at the end of 2004. The analysis of the first year's data is already finished and published [69]. A summary of these data sets measured by the different detectors is given in Tab. 4.3. No significant excess of signal over background could be observed but an improved upper limit on the axion-to-photon coupling $g_{a\gamma}$ could be set combining the results of the three X-ray detectors:

$$g_{a\gamma} < 1.16 \times 10^{-10}\text{GeV}^{-1}(\text{at 95\% CL for } \text{m}_\text{a} < 0.02 \text{ eV}) \tag{4.2}$$

This result is already 5 times more stringent than the ones achieved by previous laboratory experiments and it is comparable to constraints from astrophysical considerations. It will be further improved by the analysis of the 2004 data (see Fig 4.23).

4.4.2 Preparations for Phase II

With the setup of Phase II, the CAST experiment will improve the upper limit on $g_{a\gamma}$ in an extended axion mass range, and, for the first time, a laboratory experiment will have the opportunity to enter the axion model zone (shaded band in Fig. 4.23).
As a first step ^{4}He will be inserted in the magnet bore. ^{4}He will be usable at 1.8 K for pressure settings up to about 6 mbar before liquefying (74 steps with $\Delta P = 0.08$ mbar will be applied). Then, ^{3}He will be used at up to 60 mbar (590 pressure settings in steps of $0.08 - 0.1$ mbar are planed).

The sensitivity of CAST for determining $g_{a\gamma}$ depends basically on two things: the available time to measure with each pressure setting and the number of steps in the pressure increment.
Each pressure setting gives a narrow distribution around the corresponding axion mass to determine a $g_{a\gamma}$-limit (see Fig. 3.6). Partly overlapping distributions in the mass range determine the number of pressure settings. The more time and the more steps, the better will be the limit on $g_{a\gamma}$ in the newly explored axion mass range, i.e. $g_{a\gamma}$ will decrease.
For an exclusion plot, i.e. if no signal is observed, the 2σ-limit on $g_{a\gamma}$ in the simplest scenario (Gaussian distribution) can be used and thus the dependence of $g_{a\gamma}$ on the observation time t can be obtained utilizing Equation (3.16) as

$$g_{a\gamma} \propto \sqrt[8]{1/t}\,. \tag{4.3}$$

Thus the larger t the smaller, i.e. the better, will $g_{a\gamma}$ be. Furthermore, this implies that measuring e.g. t=1 day (instead of $2^8 = 256$) will worsen the upper limit on $g_{a\gamma}$ by a factor 2 only.
For ^{3}He, even more steps are needed to cover the desired mass range and thus, within the available time, the limit on $g_{a\gamma}$ will increase. This can be seen in the steps visible in the exclusion plot (see Fig. 4.23).

At the moment, a new gas system for ^{4}He and ^{3}He is about to be built and novel "cold windows" to protect the detectors from the cold He gas in the magnet bore will be implemented in the experimental setup. Additional X-ray optics for one of the detectors (Micromegas) are designed to be used, leaving CAST with two X-ray focusing devices for its second phase.

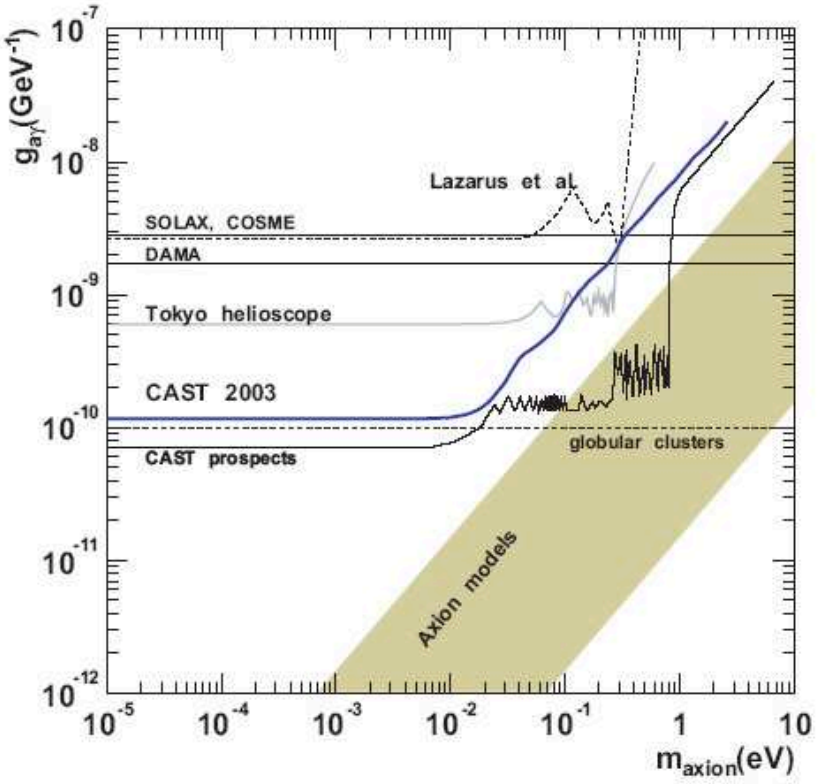

Figure 4.23: Exclusion plot of the axion to photon coupling constant (at 95% CL) obtained from the 2003 data of CAST. The result is more stringent than other laboratory constraints. Theoretical models are represented by the shaded band. Prospects for CAST's second phase, which will enter the axion model zone, are shown as well [69].

Chapter 5

Filming the Sun: Spring 2005

For March 2005, a new setup for the solar filming was designed, tested and used for the first time. To start with, the components of the system will be presented, in order to show, which improvements have been achieved and were subject to testing in Spring 2005. The alignment with the magnet and the actual data taking will be described. Furthermore, the performed analysis of the pictures will be presented in this chapter. Special problems, which occurred either during filming or analyzing, will be discussed. These were difficulties, such as the influence of changing the focus settings and an apparent distortion of the shape of the solar disk in some pictures. Finally, results will be given and conclusions drawn. Basically, the filming in March 2005 can be considered as a test for the new setup, especially because the magnet was not in its usual operating condition, due to the start of modifications of the experiment to make it ready for its second phase. The opportunity was taken to test as many different conditions for the filming as possible in order to be well prepared for the Fall 2005, the next chance to observe the Sun.

5.1 The new Setup for Spring 2005

5.1.1 The Initial Situation

As a starting point for improvements of the solar filming system, the setup described in Chapter 4.3 was given (see Fig. 4.18): a standard webcam, an optical telescope fixed inside a sphere with the specifications of a Taylor-Hobson sphere (TH-sphere[1]) and three polarization filters (linear and circular). The basis for the best possible position of a new setup was the platform on the Jura side, located at a distance of 1014 mm to the left of the magnet tube V1 and at a height of 408 mm above the same pipe (see Fig. 4.20).
The most motivating aspects for a new setup were the limited resolution of the webcam and problems with the alignment of the camera and the attached telescope with the magnet axis. The limited resolution had hitherto restricted the achievable precision of the solar

[1]The notation TH-sphere will be used in the following to describe a sphere with the dimensions of a standard Taylor-Hobson sphere as described in Section 4.3.2 and Figure 4.19 (p. 55), which might however hold a telescope or crosshairs.

Figure 5.1: Best available view from the side platform for the new setup as tested with the webcam/telescope in Fall 2004. The Helium tank can bee seen in the lower part of the window, while the girder in the middle is partly hidden behind the yellow structure supporting the magnet.

filming. The alignment turned out to be difficult, because the system had to be brought into a position such that the center of the crosshairs within the telescope matched with the light spot in the center of a standard Taylor-Hobson sphere at about 5 m distance as well as with the tip of a pointer, which was approximately 7.6 m away from the camera. Once aligned as well as possible, the webcam had to be screwed to the surveyor's cup for Taylor-Hobson spheres in which it was sitting. It was difficult to keep the camera in the aligned position while fixing it. Additionally, in the course of performing the fine adjustment of the alignment, the focus had to be changed by turning the ring which fixed the webcam to the telescope. This changed the alignment as well, since the system was slightly moving in the course of touching the focus ring.
Predictable complications for a new setup, which were already present in the old system, were given by the environment of the experiment and had to be minimized as far as possible. Trees in a nearby wood outside the CAST experimental area have been obstructing the view of the Sun (more during the period of filming in Fall than in Spring because of the foliage). Furthermore, the window through which the Sun can be filmed is separated in two pieces by a steel girder, which cannot be removed since it is a support structure. Unfortunately, narrowing the time window of possible Sun observation even further, a Helium tank placed right outside the experimental area blocks the view in the lower to middle part of the window (depending mainly on the height of the camera position). However, these limiting factors were minimized by the choice of the position of the new setup and thus quite a good view could be achieved, at least for the left part of the window, as can be seen in Figure 5.1.

Figure 5.2: The ST-7 from SBIG [114]. When used at CAST, the camera is turned upside-down, which in principle does not make any difference and was just done for technical reasons such as to have better access to the power supply, USB connection and so on.

5.1.2 The CCD Camera and the Optics

The main objective for improvements was a new camera with appropriate optics, which could be borrowed from the MPE[2] for Spring 2005 in order to test if it would work for the purposes of CAST. The camera, an ST-7E from SBIG[3], is a CCD camera with two sensitive chips: one for imaging and one for guiding the camera if it is used in astronomic photography. For the filming of the Sun at CAST only the imaging chip was used, which is a Kodak KAF0401E with 765×510 pixels of a size of 9×9 μm^2, hence resulting in an total dimension of about 6.89×4.59 mm^2.
An image of the outer appearance of the camera can be found in Figure 5.2, while technical drawings are to be found in the Appendix A (Fig. A.1 and A.2). More technical details are given in Ref. [114].
In combination with the ST-7E, Olympus optics (OM-System, E. Zuiko, Auto-T, 1 : 4) of 200 mm focal length were used (see Fig. 5.3 for outer dimensions). Attached to the CCD camera by a special adapter ring from SBIG with a thread on the camera side and a bayonet connection on the lens side, the Olympus optics can be focused to distances between 2.5 m and infinity (beyond 30 m). It should be mentioned that the bayonet connection caused some troubles, because it was not as rigid as it was supposed to be and thus the optics were not completely fixed in a position perpendicular to the camera resulting in shifts of the picture.
The field of view resulting from this combination of CCD camera and optics in arc seconds per pixel can be calculated as [114]:

$$\text{Field of View} = \frac{20.6 \times \text{pixel size}\,[\mu\text{m}]}{\text{focal length}\,[\text{cm}]} = \frac{20.6 \times 9}{20}\,[\text{arcseconds}] = 9.27\,'' \approx 0.026^\circ,$$

[2]Max Planck Institute for Extraterrestrial Physics in Munich
[3]Santa Barbara Instrument Group

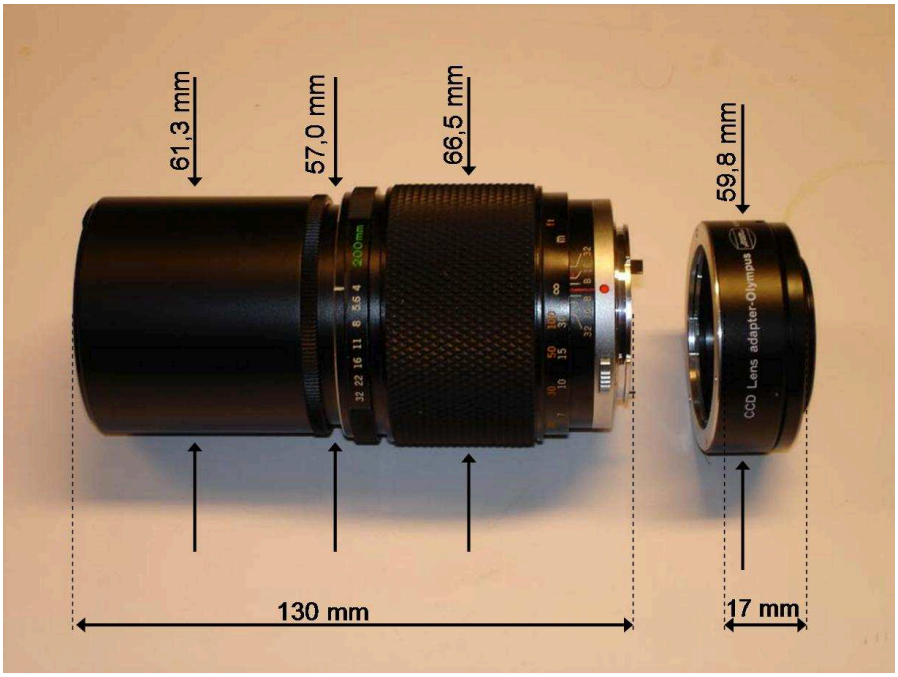

Figure 5.3: Olympus optics of 200 mm focal length. On the right side the adapter ring to attach the lenses to the ST-7E can be seen [115].

where the factor of 20.6 results from a unit conversion of radian to degree. The field of view for the whole chip is therefore approximately $1.31° \times 1.97°$. The Sun (with a size of $\approx 0.5°$) can thus be imaged completely .
In order to appreciate the improvement achieved by using this new camera, an alignment picture of both the old and the new setup is shown in Figure 5.4.
To protect the sensitive CCD-chip by reducing the intensity of the incoming light in the visible spectrum and in order to have a better view of the Sun, different filters were tested:

- A special solar filter foil used for observations of the Sun by eye or camera (Transmission[4] of about 0.001% or, equivalently, an optical density[5] of approximately 5.00).
- A glass filter of unknown transmission (optical density), however less than 0.001% transmission, i.e optical density larger than 5.00.
- Kodak Wratten Gelatin filters with transmissions of 32%, 13%, 10%, 1%, and 0.1% corresponding to optical densities of 0.50, 0.90, 1.00, 2.00, and 3.00.

The filters were placed right in front of the optics. However, there was some space, and thus air, in between the lenses and the filters and furthermore, the optical axis and the filters

[4]The transmission T is the ratio of the output energy of a filter to its input energy expressed in terms of percentage.

[5]The optical density D is the reciprocal of the transmission T expressed in logarithmic terms: $D = \log_{10}(1/T)$.

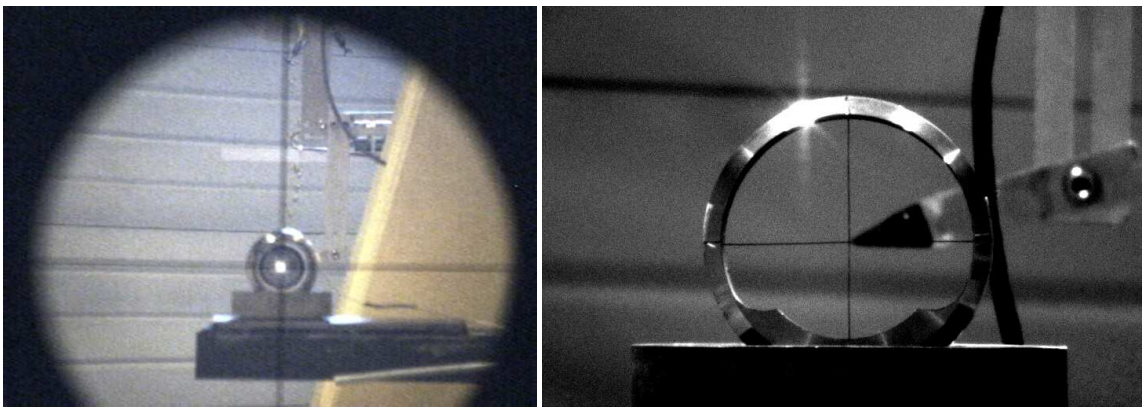

Figure 5.4: Left image: Picture of the standard Taylor-Hobson sphere taken with the old setup (Webcam with telescope) in Fall 2004. Right image: Alignment picture focused to 5 m (Crosshairs) taken in Spring 2005 with the ST-7 and the Olympus optics.

might have been not exactly perpendicular, possibly resulting in aberration, especially for the thicker glass filter. Combinations of different filters were used as well.

5.1.3 The Platform and the Camera Support

The new camera demanded the design of a support to hold it. The idea was to construct it in a way, such that both translation and rotation of the ST-7 were possible. In the three spatial directions ≈ 1.5 cm total movement for each direction was provided, while the camera could be rotated for about 25°. This simplifies the fine-adjustment of the alignment. The 3D-support can be seen in the left image of Figure 5.5.
In order to use the best possible view, it was necessary to be in the axis determined in Fall 2004 with the old setup. This however implied, due to the new support, that a novel platform was needed at a lower level than the former one to compensate for the height of the 3D-mounting. The new platform was attached to the already existing side platform (see Fig. 5.5, right image). The adjustment turned out to be a bit difficult and in addition there were some concerns, if the weight of the new platform, the support and the camera would twist the original carrier they were fixed to. This, however, was ruled out by surveyors' measurements.
Technical drawings of the support and the platform can be found in the Appendix A (Fig. A.3 and Fig. A.4 respectively).

5.1.4 The Crosshairs and the Pointers

Since a new system to align the camera with the magnet bore should be used (more details in Sect. 5.2.1), it was necessary to have a target like the Taylor-Hobson sphere, but with the possibility to view a second target, i.e. a pointer, through this device. Therefore, a sphere of the desired standard size was built with two copper wires inside ($\varnothing = 0.3$ mm each), crossing in the center of the sphere (see Fig. 5.6). This defines an exact point, which

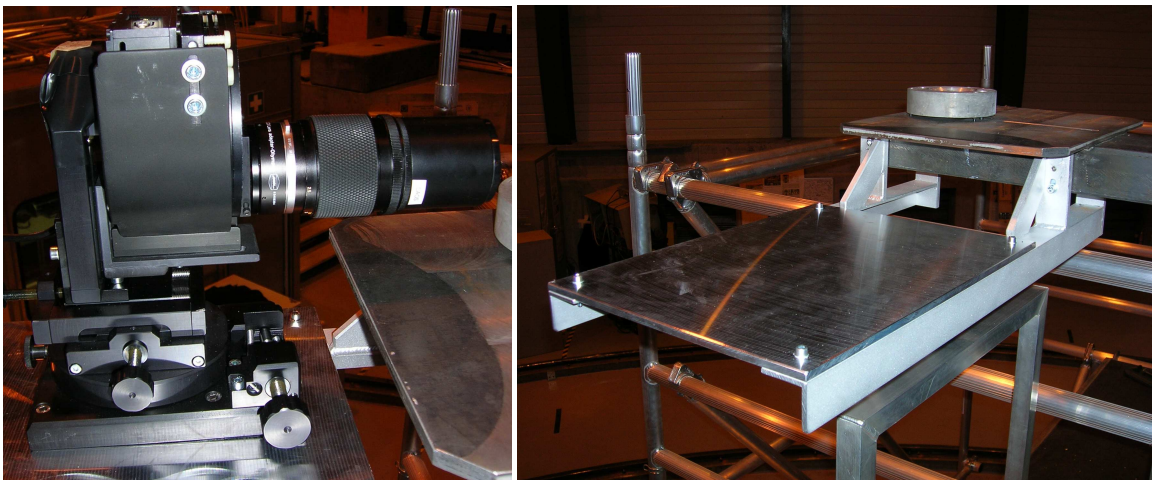

Figure 5.5: Left image: The 3D-support for the ST-7. Movements in the 3 spatial dimensions and rotation of the camera are possible. The optics (attached to the camera) can be seen in the upper right part of this picture. Right image: Platform used as a basis for the 3D-support and the ST-7 itself, in a way to allow for a clear view of the Sun through the window.

does not change if the sphere is rotated. It can be used as a reference. Illumination of the sphere in order to improve the visibility of the wires was possible, but in tests it turned out that it was easier to see the wires without lights due to reflections caused by the copper.
As a second target, two pointers were available from the old setup. The first pointer, a rather roughly cut one from aluminum, was exchanged in the course of filming in Spring for a second, very precise pointer within a disk. Its tip marks the center of the circle as it is given by the disk (see Fig. 5.7).

5.2 Alignment and Data Taking

5.2.1 The Alignment of the Setup

In addition to the usage of the new setup, a novel way of alignment was chosen. The basic principle was to align the camera by utilizing both targets (crosshairs and one pointer) at the same time, thus applying the same principle as it is used for aiming with a rifle (rear and front sight). The geometers aligned the pointer and the cross wires with the magnet axis and then the camera was brought into its position on the same axis by overlapping the tip of the pointer and the center of the crosshairs. This crossing point in the pictures will be called the reference point and it will indicate where the magnet is actually pointing.
The alignment of the two targets was performed in height as well as in distance of the magnet tube V1, which is the Jura side pipe of the two available ones (see Fig. 5.8). A point for the surveyors' reference on the side platform in front of the camera was used for this purpose.

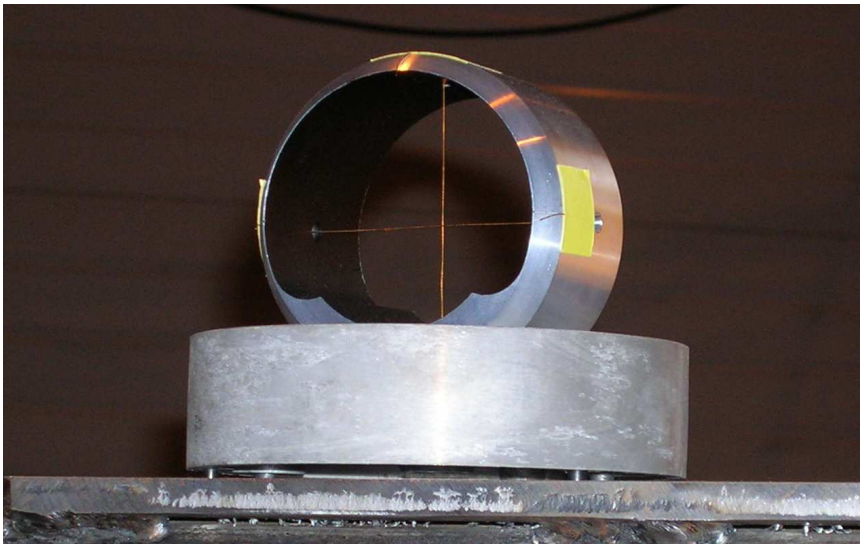

Figure 5.6: Crosshairs inside a standard Taylor-Hobson sphere used as a target in 5 m distance from the camera.

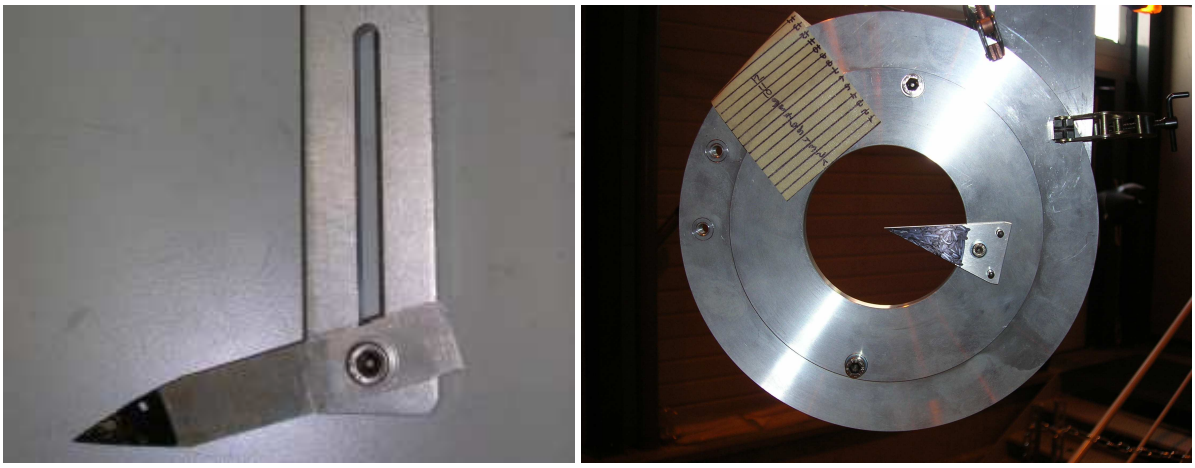

Figure 5.7: Left image: Roughly cut aluminum pointer. Right image: Precise Pointer indicating the center of the disk with its tip.

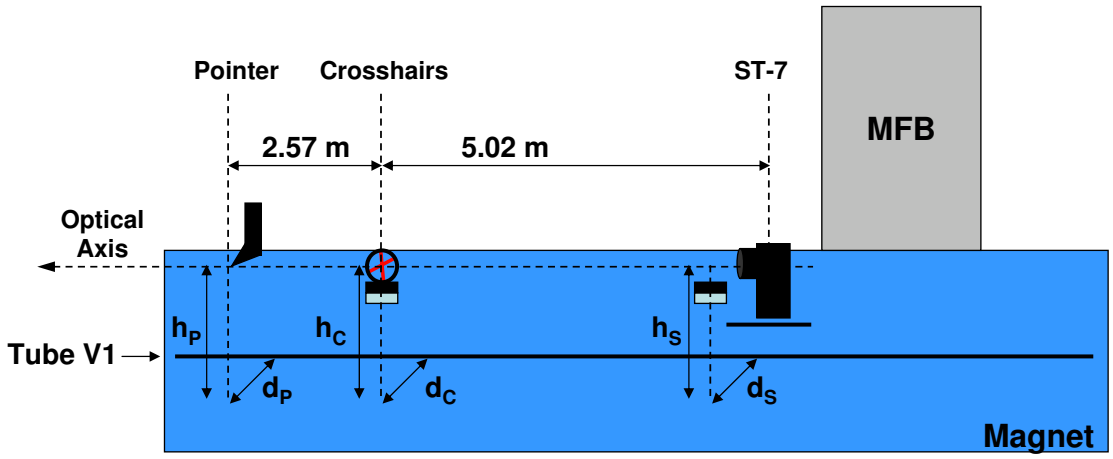

Figure 5.8: Alignment of the new setup. h_P, h_C, and h_S denote the height of the pointer, the crosshairs and the surveyors's cup (in front of the ST-7 to align pointer and crosshairs) above the magnet tube V1. d_P, d_C , and d_S on the other hand are the horizontal distances between the optical axis and the pipe V1.

The first alignment by the surveyors (imprecise pointer used) gave the following values for the heights h_P (height of pointer above tube V1), h_C (height of crosshairs above V1) and h_S (height of surveyors' reference point above V1) as well as for the distances d_C (horizontal distance of the crosshairs from V1) and d_S (horizontal distance of the surveyor's reference point from V1):

$$h_P = h_C = h_S = 408.3 \text{ mm}$$
$$d_C = 1014.1 \text{ mm}$$
$$d_S = 1014.5 \text{ mm}$$

Unfortunately, d_P (distance of the pointer from V1) was not measured, thus the pointer was not aligned for horizontal distance to the tube. The error in the alignment resulting from this can be estimated.
It should be mentioned, that the pointer was exchanged for the third day of filming: the inaccurate one was substituted by the precise disk with pointer. The alignment of it was checked by the geometers after the filming finished, giving the following values:

$$h_P = 408.8 \text{ mm}$$
$$h_C = 408.3 \text{ mm}$$
$$h_S = 408.3 \text{ mm}$$
$$d_P = 1014.1 \text{ mm}$$
$$d_C = 1014.1 \text{ mm}$$
$$d_S = 1013.5 \text{ mm}$$

Table 5.1: Summary of possible errors for the alignment of the setup (camera, crosshairs, and pointer) to film the Sun in Spring 2005.

Source of Error in Alignment	**Maximal Value** 16.3.2005 Pointer only Filming Mode	**Maximal Value** 17.3.2005 Pointer only Tracking Mode	**Maximal Value** 21.3.2005 Pointer in Disk Filming Mode
Surveyor's measurements	$< 0.006°$	$< 0.006°$	$< 0.006°$
Pointer Misalignment	$\approx 0.008°$	$\approx 0.008°$	$< 0.004°$
Crosshairs	$\approx 0.006°$		
TOTAL	$< 0.012°$	$< 0.010°$	$< 0.008°$

5.2.2 Study of Systematic Errors in the Alignment

There are three major contributions to the systematic error of the alignment:

- Uncertainties in the surveyors' measurements
- Error due to the misalignment of the pointer in distance from the magnet tube
- Inexactness of the crosshairs

The surveyors' precision is given as 0.5 mm/5 m (about 0.006°), 0.5 mm/7.5 m (about 0.004°) for crosshairs and pointer respectively.
The second contribution given by the pointer, which was not checked for being aligned, can be estimated to be < 1 mm/7.5 m, i.e about 0.008°. For the third day (precise pointer used) this error was less than 0.004° according to geometers' measurements.
The crosshairs were checked for precision, and turned out to be 0.5 mm off, i.e about 0.006°. After the first day of filming, however this was improved by further stressing the wires, such that no deviation was observable anymore. For the affected first day of filming, this was included in the error calculations for the alignment.
Additional tests for possible sources of further errors were performed:
It was checked that the optics of the camera were as horizontal as the magnet axis. Once aligned, taking them off and putting them on again did not produce any change observable with the surveyor's instruments.

The total error of the alignment can be calculated to be $< 0.012°$ (see Tab. 5.1), i.e. about 2.3% of the solar diameter, for all three days of solar filming.

5.2.3 Data Taking

Following all preparations, the Sun was filmed on three days in Spring 2005, namely on March 16, 17 and 21. The magnet was following the Sun in filming mode (correction for

atmospheric refraction) for the first and the last date, while the system used the usual tracking mode (no refraction correction applied) on the 17th of March.
While using the filming mode was the general practice performed for all previous filmings, it was the first time to take pictures of the Sun while pointing to its real position instead of its apparent one. In doing so, and calculating the difference in position due to refraction to compare the observed position with the expected one, the tracking program can be checked directly, i.e. without using a correcting program such as the filming mode.
Since, at the time of filming, the magnet was not in its usual condition[6], the filming was primarily seen to be a test for the new setup and a possibility to figure out the best way to film the Sun. Therefore, many different conditions were tested for their usefulness, summarized as:

- Use of different focus settings while aligning and filming
- Filming with and without the crosswired TH-sphere
- Diverse kinds of filters to get good quality pictures
- Two different pointers as a second target in combination with the crosshairs
- Both modes offered by the software, i.e. tracking and filming mode

5.3 Analysis

Due to the different treatment and distinct problems encountered for the pictures taken in different modes, they will be discussed separately.

5.3.1 Filming Mode Pictures (16.3.05/21.3.05)

Processing of the Pictures

After sorting the pictures according to the different conditions (Crosshairs on/off, various settings of focus), which influence the apparent size of the Sun and possibly also its observed shape, the diameter of the solar disk was determined by choosing an appropriate circle (Red in lower image of Fig. 5.9). The solar core is marked by two further red circles with a size of 10% and 20% of the previous one, having the same center. From reference pictures of the pointer and the cross wires taken before the actual filming (see upper image in Fig. 5.9), the expected center of the Sun, i.e. the point where crosshairs and the tip of the pointer are in line (reference point), is determined. It is marked in green in Figure 5.9. The diameter is of no importance, only the center matters as it denotes the reference point. The last important thing to be aware of is the field of view for the magnet bore, marked in blue in the same figure. At this stage no errors of alignment or analysis are included in the picture, but one obtains a first impression on where the magnet is pointing.
The position of the observed solar center can be obtained from every picture taken during

[6]The TPC and its shielding were not installed causing a difference in weight of about 1.2 t.

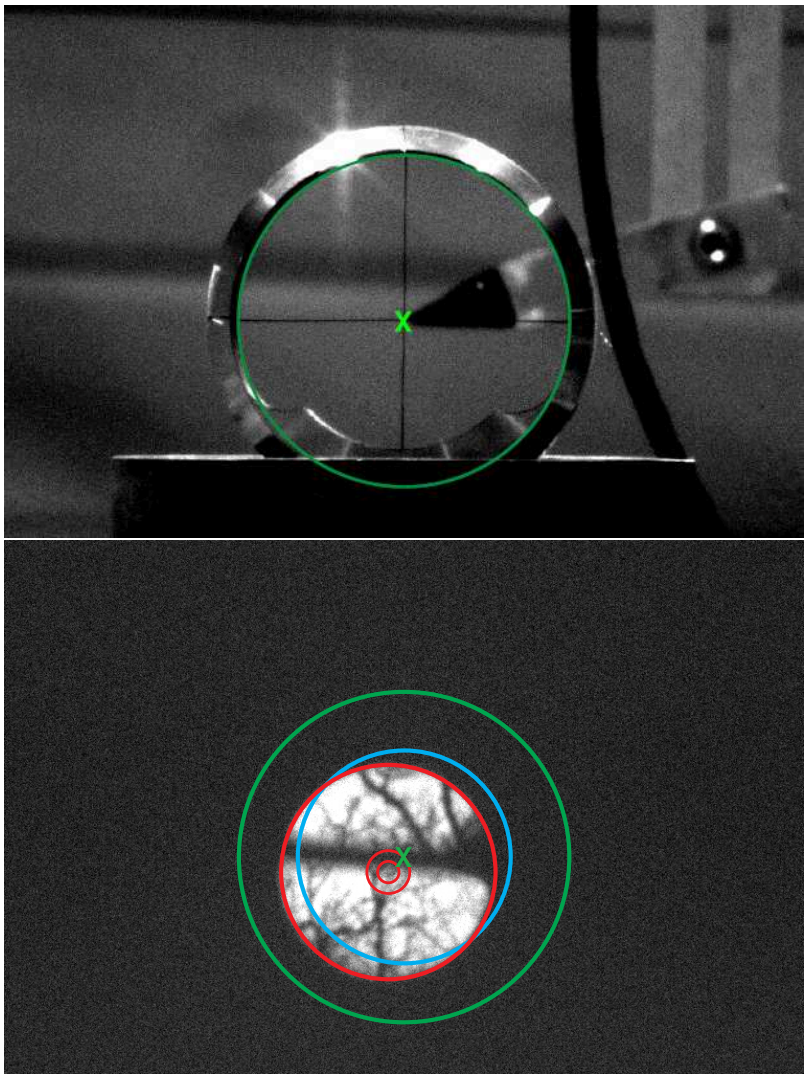

Figure 5.9: Upper image: Picture taken on the 16th March before the actual filming to verify the alignment. The reference point is the center of the green circle (its diameter is adjusted to the TH-sphere size, but it is basically arbitrary). Lower Image: Taking the reference from the upper image (green), the solar disk and two disks with 10% and 20% of the solar diameter (i.e. the solar core) are marked in red. The field of view of the magnet bore, i.e. its acceptance region for incoming axions, is drawn in blue.

filming and the distance to the reference point in x- and y-direction can be calculated. X-axis and y-axis are chosen in the direction of the tracking movement. Knowing the field of view per pixel for the camera in combination with the optics, it is possible to convert these observed distances given in pixels of the picture into a corresponding deviation in degrees.

Study of Systematics

Before analyzing the pictures of the Sun in more detail, a look at the sources of errors is appropriate. As far as systematic errors are concerned, there are basically two major aspects limiting the precision of the filming setup:

- The alignment of the system with the magnet axis
- Errors in the analysis of the pictures with the computer

The errors due to the alignment were already discussed in Section 5.2.1 and calculated to be $< 0.012°$ for all three days of filming.
For the second source of errors originating from the analysis, three things have to be considered:
Using different focus settings for taking the pictures changes the image (More details can be found in Sect. 5.3.3) and results in an error of the order $\mathcal{O}(0.02°)$. Furthermore, the choice of the circle center might lead to different values for its coordinates x and y, thus changing the distance between observed and expected solar central point. Nevertheless, this uncertainty turns out to be smaller than the previous one and leads to a contribution of the order $\mathcal{O}(0.005°)$. There is a further contribution to the error of the order $\mathcal{O}(0.01°)$ originating from the transformation of the distances in pixel or mm (as obtained from the pictures) to the desired unit degree, due to uncertainties in the field of view of the filming system.

For the data of 16th March 2005, i.e. the filming before the change of the pointer, an additional correction has to be applied. In the pictures, it can be seen that the pointer and the crosshairs are not exactly in line. The pointer is 4 pixels to the right side of the center of the wires, which means the camera is about 1.2 mm to the right of the optical axis, i.e. towards the magnet, and it is turned such that the ST-7 and its optics are not parallel to the magnet axis (see Fig. 5.10). Therefore, the central point of the Sun is expected to be to the left of the reference point, in fact $0.013°$ to the left. This is only the case for the x-coordinate, not for the height (y-coordinate) as can be seen from alignment pictures. Data taken on March 16 were corrected for this shift. For March 21, no visible misalignment occured. The systematic uncertainty resulting from the determination of the shift for the x-direction is of the order $\mathcal{O}(0.006°)$, while for the y-coordinate it is larger, namely of the order $\mathcal{O}(0.012°)$.

Combining all systematic errors results in a total uncertainty of $0.026°$ for the x-coordinate and $0.028°$ for the y-direction[7].

[7] As a reminder: The error of the tracking accuracy of the system to follow the Sun is $< 0.02°$.

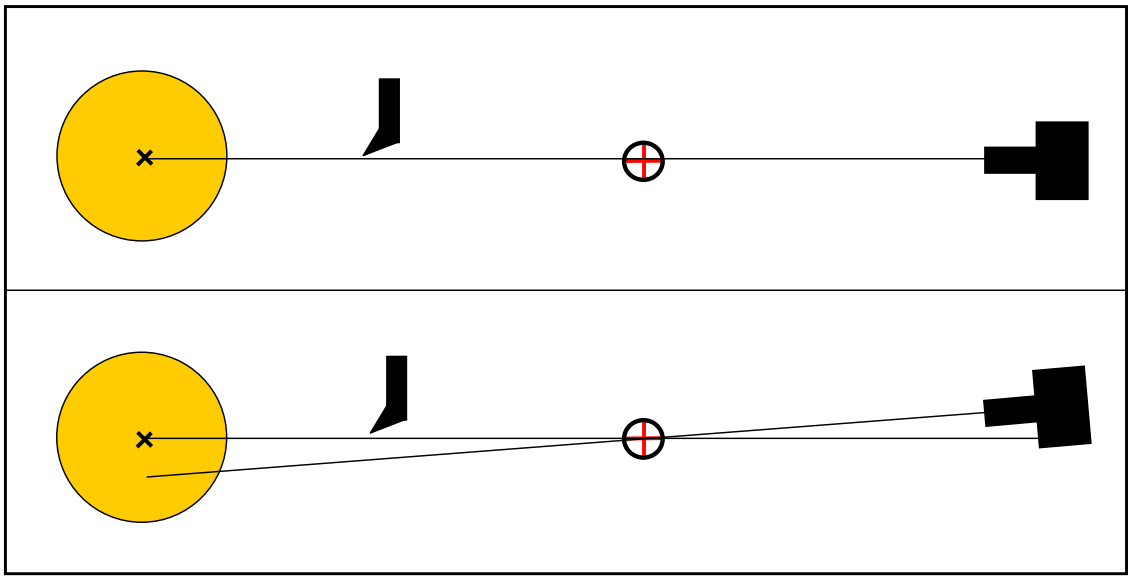

Figure 5.10: Upper image: Top view of filming setup (camera, crosshairs, pointer) for perfect alignment with the magnet axis. The reference point is expected to be equivalent with the observed center of the Sun, provided that the magnet is precisely following it. Lower image: Top view of filming setup for the camera placed too much to the right of the optical axis. There will be a gap observable between pointer and crosshairs (instead of an overlap of the two), and one expects to see the crosshairs to the left of the solar center. This shift can be calculated.

Observations

First it was checked, if the observed points for the solar center of both filming days with refraction correction were compatible with each other and the expected value, i.e the reference point. Then the pictures were sorted according to the focus setting. This was done in order to see the effect of different settings and check the compatibility of the observed center in the pictures with the reference point.

Sorted by Day In Figure 5.11(a), the reference point is set to be the origin of the coordinate system and the distances of the observed points in x-direction as well as in y-direction from (0, 0) are plotted in degrees. On first view, all measurements are lower than the expected center of the Sun and slightly to the left, which (if significant) would imply the magnet is pointing too high and too much to the right, since the reference point indicates where the magnet is pointing. Data points from the first day of filming tend to be a bit more to the right side of those for the second day and they are slightly more spread in both x- and y-direction. The plotted points are generally multiple points at the same position. In most cases, they result from subsequent pictures taken without any change of focus and can be regarded as independent measurements.
In order to check if the data of the two days are compatible, the observed points per days are averaged and the according errors are calculated. For March 16 and 21, the averaged

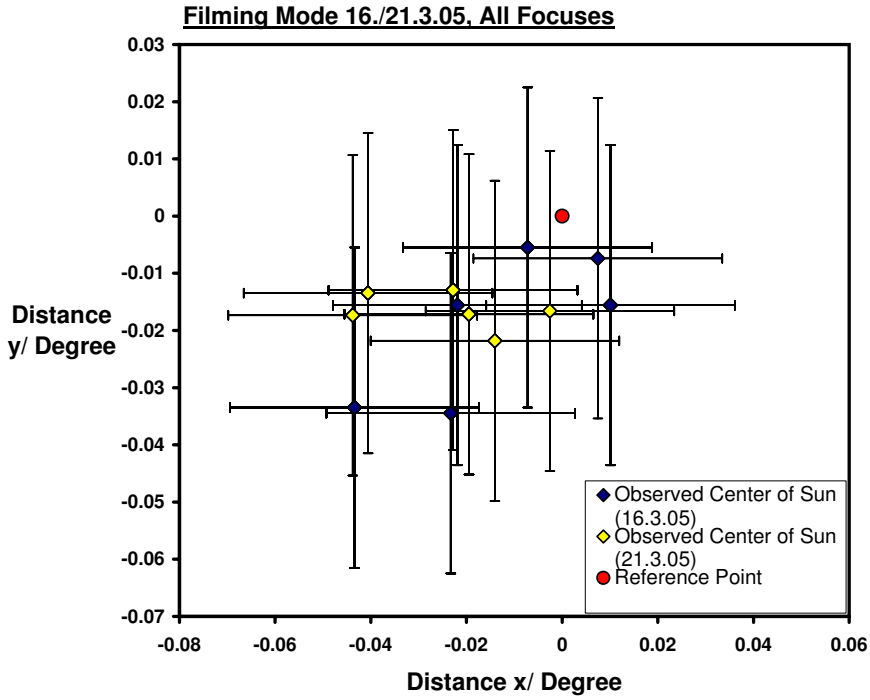

(a) All distances of the observed solar center from the reference point in degree. The data points are sorted by day. The error bars are the systematic uncertainties.

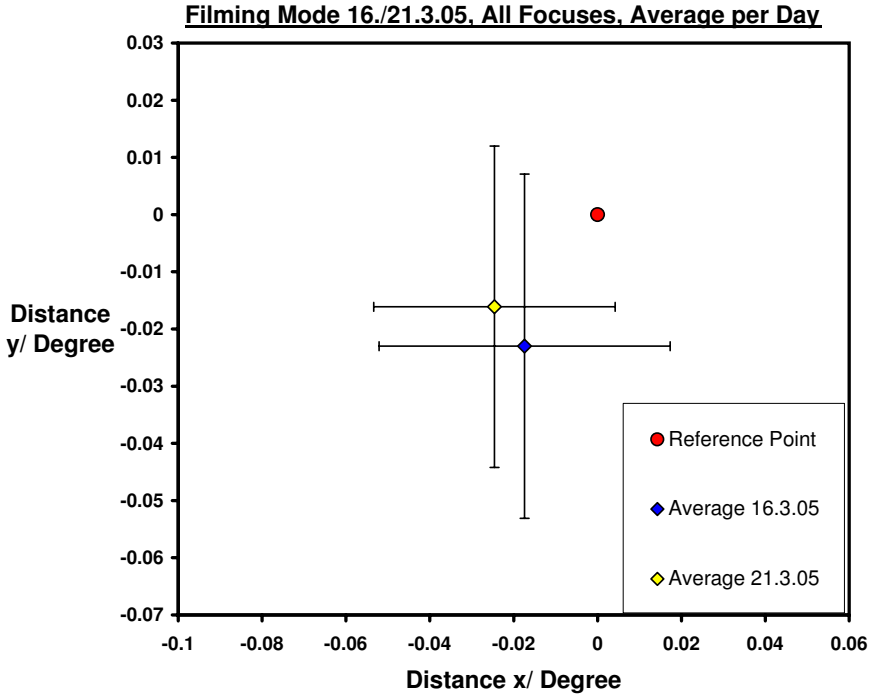

(b) Distances of observation and reference for the solar center in degrees averaged per day of filming. The errors are statistical and systematic uncertainties combined.

Figure 5.11: Distances of reference point and actually observed center of the Sun sorted by day. The reference point is set to be (0, 0). All focus settings are included.

distance from the reference point in x- and y-direction is:

$$\begin{aligned}
\bar{x}_{16.3.} &= -0.0174^\circ \pm 0.0037^\circ(\text{stat.}) \pm 0.0261^\circ(\text{syst.}),\\
\bar{y}_{16.3.} &= -0.0230^\circ \pm 0.0019^\circ(\text{stat.}) \pm 0.0279^\circ(\text{syst.});\\
\bar{x}_{21.3.} &= -0.0246^\circ \pm 0.0025^\circ(\text{stat.}) \pm 0.0250^\circ(\text{syst.}),\\
\bar{y}_{21.3.} &= -0.0161^\circ \pm 0.0006^\circ(\text{stat.}) \pm 0.0250^\circ(\text{syst.}).
\end{aligned}$$

The statistical error is the error of the mean value. Figure 5.11(b) shows the according plot with statistical and systematic errors combined. Within these, the data of the two days are compatible and so are the results for both days with the reference point. Thus, with a filming precision of better than 0.028° (typically around 0.026°), CAST is pointing to the center of the Sun. Considering that the solar core is about 0.054°-0.108° and the magnet acceptance region has a size of 0.532°, this is well within the desirable accuracy.

Sorted by Focus Given the consistency of the data of both filming mode days, it is interesting to sort the acquired pictures by different focus settings. A plot of this can be seen in Figure 5.12(a). The tendency of the observed points to be rather low and slightly to the left of the expected value can of course be observed here as well, since the same pictures were used arranged in another way.
In most cases, in which the observed solar center was found at different positions for the same focus setting, this happens when returning to the same focus after defocussing.
Averaging over all measured points per focus setting (see Fig. 5.12(b)) leads to the conclusion that all points are compatible with each other and the reference point within the combined statistical and systematic error:

$$\begin{aligned}
\bar{x}_{\ 5m} &= -0.0421^\circ \pm 0.0005^\circ(\text{stat.}) \pm 0.0261^\circ(\text{syst.}),\\
\bar{y}_{\ 5m} &= -0.0246^\circ \pm 0.0035^\circ(\text{stat.}) \pm 0.0279^\circ(\text{syst.});\\
\bar{x}_{\ 7m} &= -0.0247^\circ \pm 0.0043^\circ(\text{stat.}) \pm 0.0261^\circ(\text{syst.}),\\
\bar{y}_{\ 7m} &= -0.0192^\circ \pm 0.0028^\circ(\text{stat.}) \pm 0.0279^\circ(\text{syst.});\\
\bar{x}_{10m} &= -0.0219^\circ \pm 0.0004^\circ(\text{stat.}) \pm 0.0261^\circ(\text{syst.}),\\
\bar{y}_{10m} &= -0.0156^\circ \pm 0.0031^\circ(\text{stat.}) \pm 0.0279^\circ(\text{syst.});\\
\bar{x}_{15m} &= \ \ 0.0035^\circ \pm 0.0034^\circ(\text{stat.}) \pm 0.0261^\circ(\text{syst.}),\\
\bar{y}_{15m} &= -0.0173^\circ \pm 0.0009^\circ(\text{stat.}) \pm 0.0279^\circ(\text{syst.});\\
\bar{x}_{30m} &= \ \ 0.0075^\circ \pm 0.0095^\circ(\text{stat.}) \pm 0.0261^\circ(\text{syst.}),\\
\bar{y}_{30m} &= -0.0074^\circ \pm 0.0037^\circ(\text{stat.}) \pm 0.0279^\circ(\text{syst.});\\
\bar{x}_{\text{Inf}} &= -0.0177^\circ \pm 0.0020^\circ(\text{stat.}) \pm 0.0261^\circ(\text{syst.}),\\
\bar{y}_{\text{Inf}} &= -0.0226^\circ \pm 0.0026^\circ(\text{stat.}) \pm 0.0279^\circ(\text{syst.}).
\end{aligned}$$

The accuracy is therefore always better than 0.029°, typically around 0.027°. By sorting the pictures according to their focus setting, neither one of the settings seems to be significantly better than the others. However, when analyzing the pictures, it is easier to determine the solar circle and thus its center, when the Sun is as sharp as possible, favoring the settings

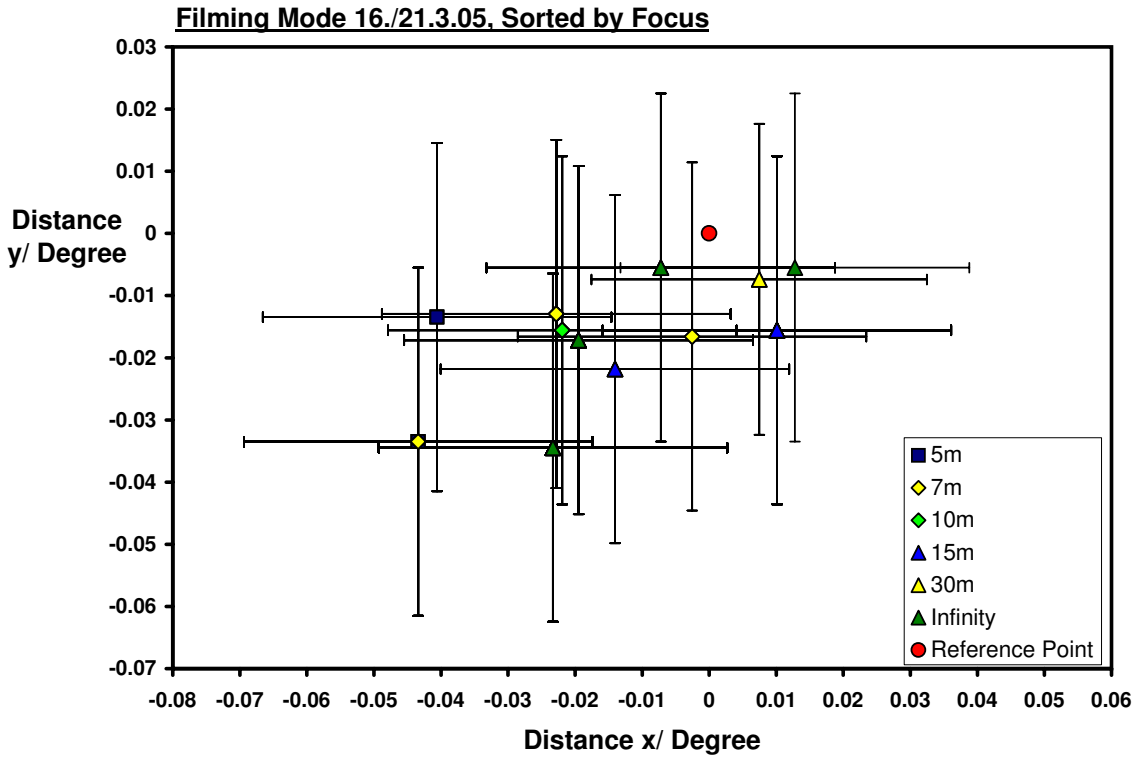

(a) All distances of the observed solar center from the reference point in degree. The data points indicate the position of the center of the Sun as observed in the different focus settings. The error bars are the systematic uncertainties.

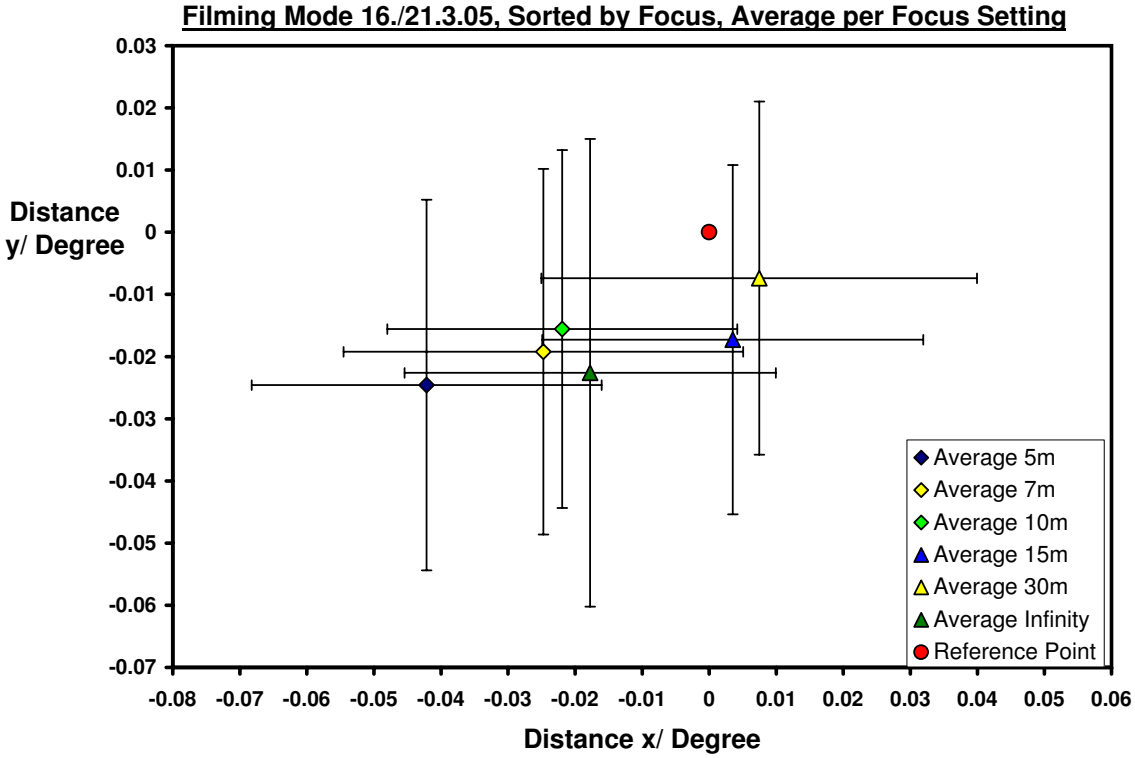

(b) Distances of observation and reference for the solar center in degrees averaged per focus setting. The errors are the combined statistical and systematic uncertainties.

Figure 5.12: Distances of reference point and actually observed center of the Sun sorted by the different focus settings used. The reference point is set to be (0, 0). Both days are included.

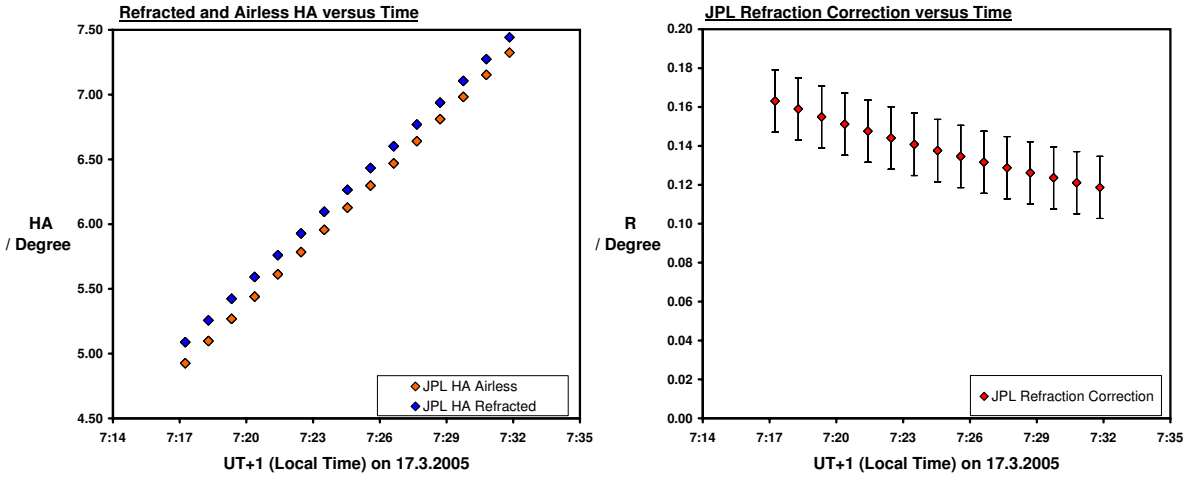

Figure 5.13: Left Plot: The real and the apparent height of the Sun above the horizon (HA) in degrees versus time for the morning of the 17th March 2005. The refraction correction is the difference between the two values for HA and it is decreasing with larger HA. Right Plot: Refraction Correction plotted versus time for the same day. It was calculated using JPL's HORIZONS System. The error bars are the systematic uncertainties.

15 m, 30 m and Infinity. It should be mentioned that the determination of the observed solar circle was not performed automatically, but by visual judgment for pictures taken in March 2005.
Averaging over all observed points during filming on March 16 and 21 leads to the mean value:

$$\begin{aligned} \bar{x}_{\text{Spring 2005}} &= -0.018^\circ \pm 0.002^\circ(\text{stat.}) \pm 0.026^\circ(\text{syst.}), \\ \bar{y}_{\text{Spring 2005}} &= -0.020^\circ \pm 0.001^\circ(\text{stat.}) \pm 0.028^\circ(\text{syst.}). \end{aligned}$$

5.3.2 Tracking Mode Pictures (17.3.05)

Processing of the Pictures

Basically, the same technique as for the filming mode was used to process the images taken in tracking mode to determine the center of the Sun from these pictures. A difference arises from handling the data obtained in this way. The reference point will show the real position of the Sun, while the measured points will indicate the center of the apparent solar location. JPL's HORIZONS System was used to calculate the refraction correction necessary for every minute during tracking. The calculated vertical angles above the horizon (HA) with and without refraction versus time are visualized in Figure 5.13.
The refraction correction R, i.e. the difference of the HA calculated for the apparent Sun position (refracted) and the HA without refraction (airless), is plotted against time in the right part of Figure 5.13.

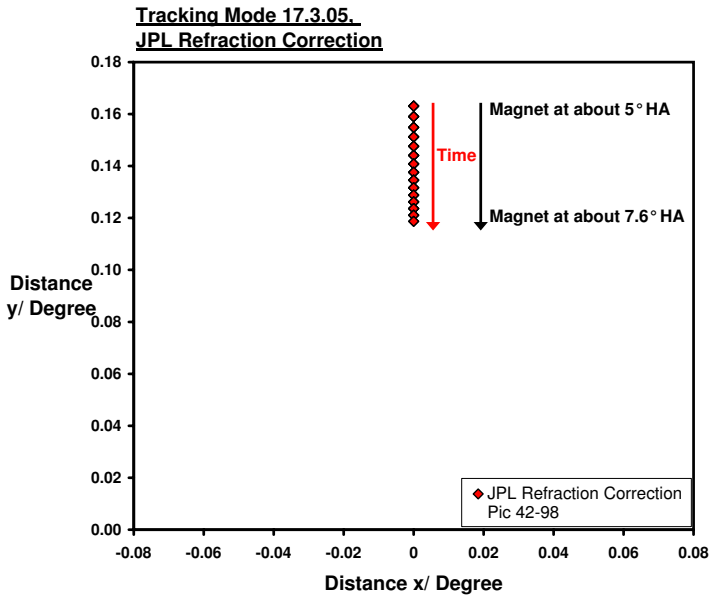

Figure 5.14: Movement of the theoretical points (JPL) in x- and y-direction due to the different refraction corrections for different HA during filming the Sun on the 17th March 2005. For larger heights above the horizon (HA) the refraction correction would decrease further and reach the value 0 for HA= 0°, i.e for the zenith.

For the analysis, the distance between the reference point and the observed solar center is calculated. This provides the observed refraction correction and can thus be compared to the theoretical refraction correction of JPL. It is important to keep in mind that in the course of tracking, the correction changes due to the increasing height above the horizon (about 5° at the beginning of filming and approximately 7.6° at the end). This can be seen in Figure 5.14.
Some additional sources of errors, compared to the filming mode pictures, have to be considered.

Study of Systematics

All systematics for the filming mode pictures are applicable for the tracking mode as well, including the shift of the measured points as it had to be considered for the data of the 16th March, due to the misalignment visible in the pictures (see Sec. 5.3.1, Study of Systematics). Since the alignment of March 16 has not been changed for March 17, the shift is of the same size, i.e 0.013°. Combining all systematic errors results in a total uncertainty of 0.026° for the x-coordinate and 0.028° for the y-direction.

Additional systematics appear due to uncertainties in the JPL data [116]. For example, due to local differences in the atmospheric conditions, the refraction correction may vary up to several arc seconds ($\mathcal{O}(0.015°)$). This is an error in y-direction only, i.e. in the direction of refraction.

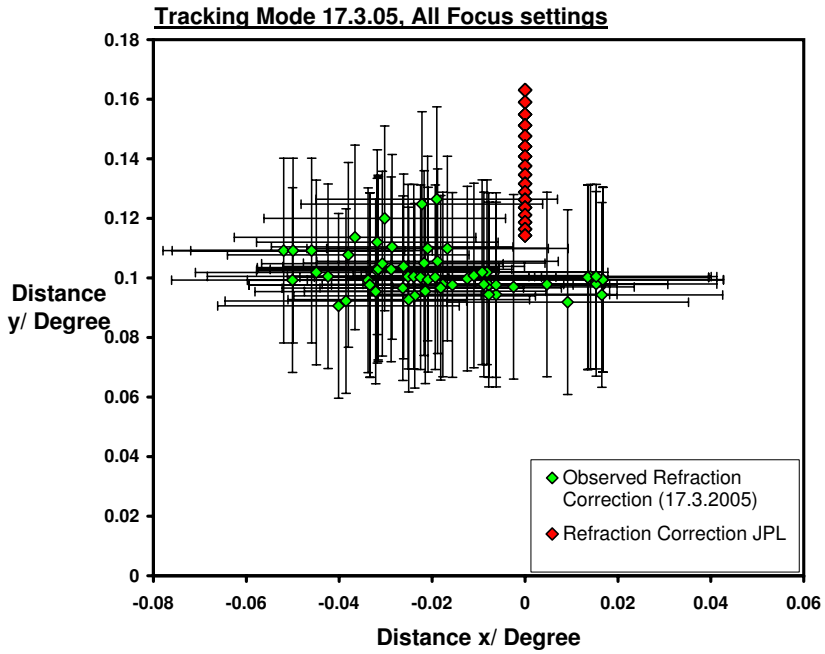

Figure 5.15: Overview on all observed refraction corrections during filming in tracking mode on March 17. The data are neither sorted chronologically nor by focus. The red symbols denote the expected values given by JPL. The error bars are the systematic uncertainties of both JPL data and the observed points.

Furthermore, the azimuth (AZ) and the height over horizon (HA), as well as the refraction correction R are calculated only once a minute by JPL. This is also the case for the logged data from the CAST experiment. However, JPL and CAST are not calculating AZ and HA at the same time and some extrapolations are necessary in order to compare the two. From this a contribution to the error in the y-direction of the JPL data arises. It is about 0.007°.
Thus the combined systematic error for the "theoretical" reference values of JPL is of the order $\mathcal{O}(0.016°)$ for the y-coordinate.
The x-coordinate of the refraction correction is expected to be zero and not to change with time, since refraction does in general not depend on the azimuth. Therefore, there is no need to apply the same errors on x as mentioned above for the y-direction. The only error that might have to be considered occurs for refraction anomalies, i.e. a dependence of the refraction on the azimuth. However, this uncertainty is negligible in our case.

Observations

A first look at the expected and the observed refraction correction, without sorting the measurements neither chronologically nor by focus setting (see Fig. 5.15), shows that the observed corrections are smaller than the expected ones by about $\mathcal{O}(0.03°)$, i.e. the magnet is pointing higher than expected. This agrees with what was observable in the filming mode pictures. However, the errors on y are of the same order of magnitude. The error bars are

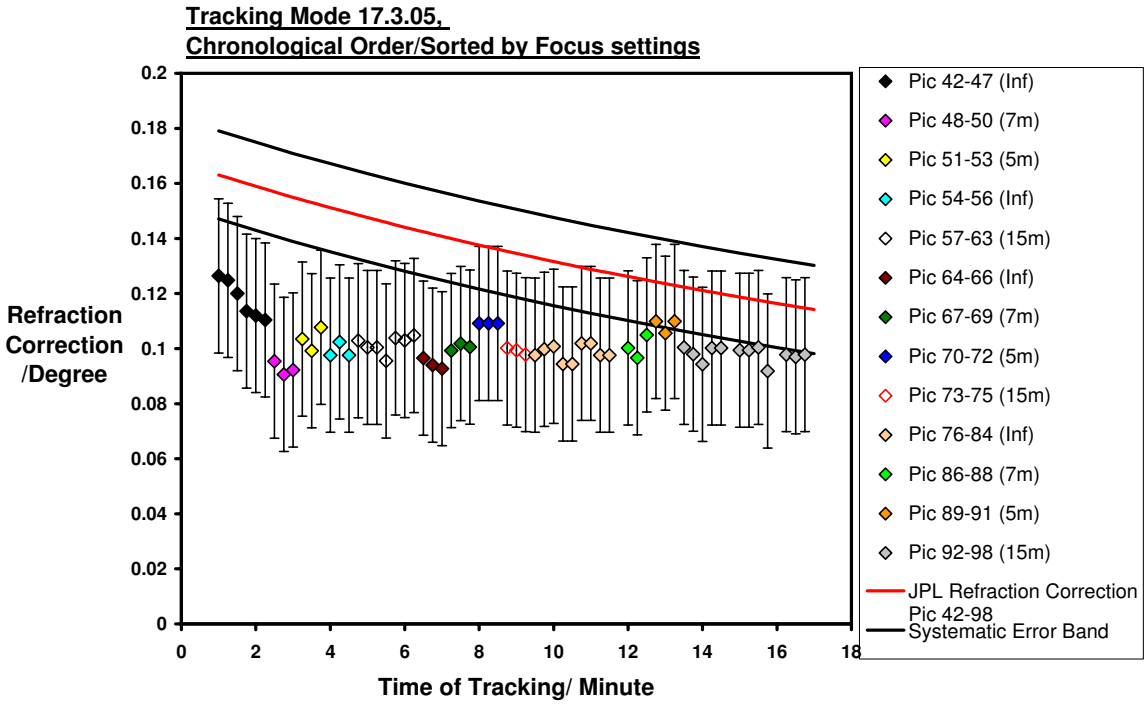

Figure 5.16: Observed and expected refraction correction during the 18 minutes of filming in tracking mode on March 17. Different focus settings are marked in various colors. The plotted error bars are systematic errors only.

the combined systematic uncertainties of both the measurements and the JPL data. The spread of the observed refraction correction over the duration of filming is smaller than the spread of the expected one. Within the errors the data points agree with the theoretical spread of about 0.05°.

For a more detailed analysis, it is useful to look at the projections, i.e. to plot the refraction correction (y-coordinate) as well as the x-position versus time. For this, an absolute time (minutes of filming the Sun) is used. JPL calculates the refraction only once per minute, while there are about 4 pictures[8] taken during this time. A fit to the JPL data is used for comparison with the observations.

In Figure 5.16 the observed and expected refraction correction during the 18 minutes of filming in tracking mode on 17th March is shown. The data points are also sorted by focus setting. Here, it can be clearly seen that the experimental refraction correction does not decrease as much as the theoretical one. It seems to be rather constant, except for the first focus setting during the initial 90 s of filming. The magnet was already tracking the Sun for some time before the filming started, so these first points cannot result from the

[8]The ST-7E has only a parallel port and hence the download times for the pictures are long. Its follow-up model, the ST-7XE, which was used in Fall 2005, has a USB connection resulting in fast downloads.

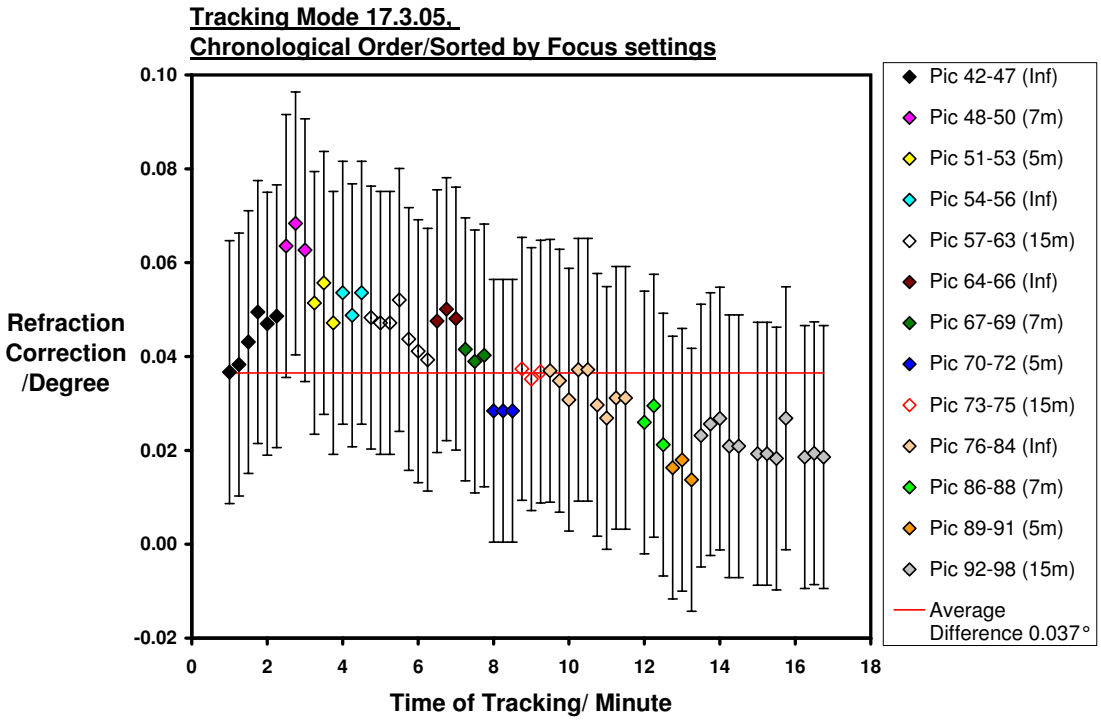

Figure 5.17: The difference between the observed and the expected refraction correction is expected to be equal to zero. The average difference is plotted as well.

magnet trying to get in its position to point at the Sun.
There are two sources of statistical errors: First, the determination of each data point has a statistical variation, since it is obtained by visual judgment. Second, the focus setting has been changed quite often during this filming in tracking mode (in most cases every three pictures) leading to jumps.
If one subtracts the observed refraction correction from the JPL data, one obtains an average difference of 0.037° with a statistical error of the mean of 0.016° and a systematic uncertainty of 0.032° (see Fig. 5.17). This difference is expected to be zero, which is the case within the combined errors. The difference is larger (about 0.06°) at the beginning of filming, when the refraction correction itself is considerable and decreases until the observed and the theoretical correction differ from each other by the order of 0.02°.

In the x-coordinate, no change is expected, since the refraction depends on the HA only. Nevertheless, there is a certain spread observable in the distances of the solar center in the pictures and the crosshairs, i.e. the reference point, as can be seen in Figure 5.18. In the beginning of tracking, there is a tendency to negative values for x. They increase during the tracking. This means that there is a movement of the magnet in x-direction observable in opposition to the tracking: In the beginning the magnet is pointing to the right side of the central part of Sun, while in the end it tends to aim to the left part of the solar core.

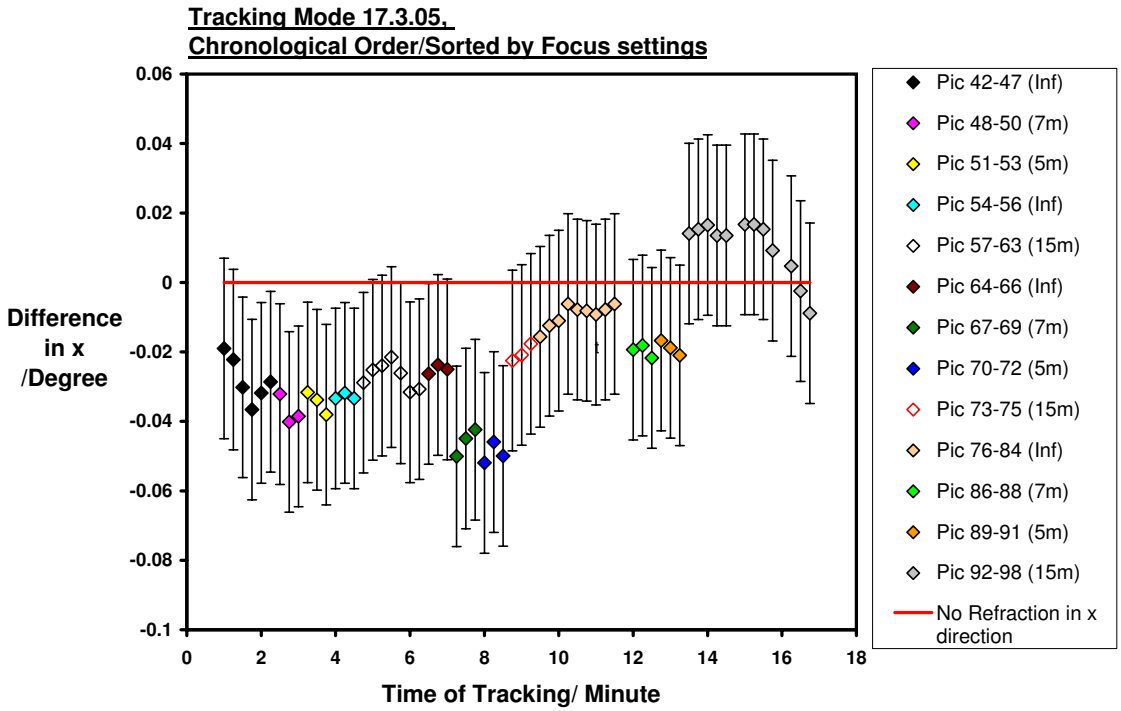

Figure 5.18: Observed and expected distance in x-direction of solar center and reference point during the 18 minutes of filming in tracking mode on March 17. Different focus settings are marked in various colors. The plotted error bars are systematic errors only.

The mean distance of the observed x-coordinates from the expected one is $-0.019°$ with a statistical uncertainty of $0.004°$ and a systematic error of $0.027°$, which implies a mean value compatible with the expected value for the difference, namely zero.

Overall, the observed refraction correction is smaller than the expected one, suggesting again that the magnet is pointing slightly too high. There seems to be a small shift in the x-direction, i.e. a movement of the magnet from a little too right to a little too left is observed in the tracking movement.

5.3.3 General Problems

Some general problems were encountered when analyzing the pictures and shall be discussed in the following.

Influence of Changing the Focus

A problem emerges from changing the focus, which is necessary for the alignment in order to bring cross wires (at about 5 m) and pointer (at about 7 m) in line as well as for filming the Sun (with focus preferably at 15 m, 30 m or Infinity) to get its shape as sharp as possible. In addition to the expected effects of changing the focus (objects out of focus are

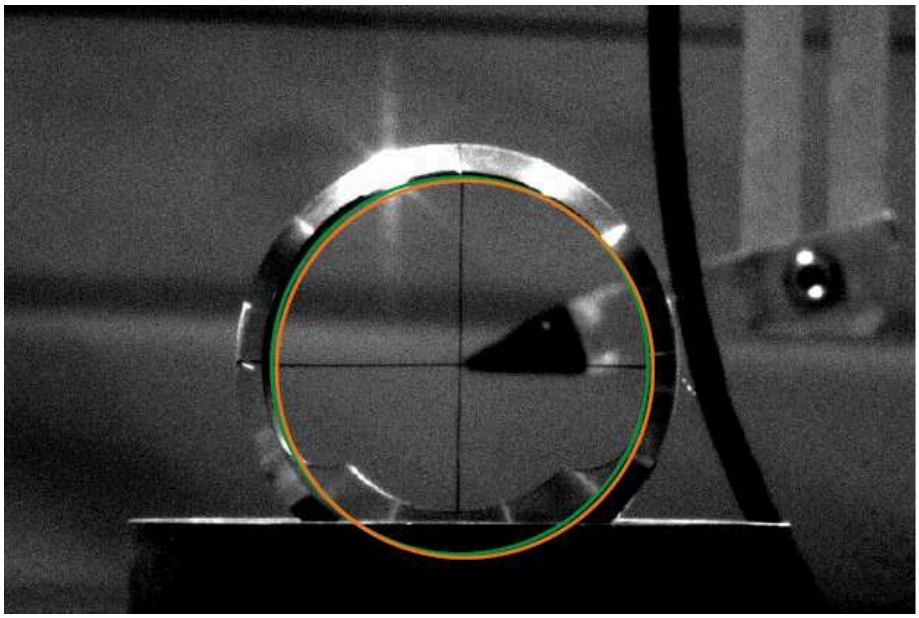

Figure 5.19: Influence of changing the focus on reference pictures. The green circle marks the center of the crosshairs when the camera is focused to 5 m, while the orange one for 7 m. The difference is about 1′-1.5′, i.e 0.017°-0.025°.

broadened), shifts in the picture can be observed. Reference pictures taken at a focus setting 5 m and 7 m give different positions for the center of the crosswires/tip of the pointer. E.g. for the 16th March (see Fig. 5.19), this results in a difference of about 0.017°-0.025°. Thus the position of the reference critically depends on the picture chosen.
By going back to the same focus after defocussing, a shift remains, changing the position of the observed point. This results in a systematic error, or (if the focus setting is changed very often) in a statistical error. The only way to avoid these shifts seems to be not to change the focus at all, which is however necessary in order to align the setup.
For filming in tracking mode, the focus was changed very often (in most cases every three pictures). Jumps in position provoked by this cause a statistical error.

Influence of TH-sphere

The hole in the TH-sphere holding the crosshairs was designed, such that the full Sun is visible through it. Since filming was done with focus to infinity, there were no big effects to expect, but some shadows could be observed on the edges of the solar disk, probably due to reflections[9] from the TH-sphere. However, this did not influence the analysis of the pictures.
In some images taken directly before filming the Sun, it can be seen that the TH-sphere is not exactly put in place, i.e. the wires on one side of the crossing point appear to be longer

[9]The TH-sphere was blackened from the inside but not from the outside.

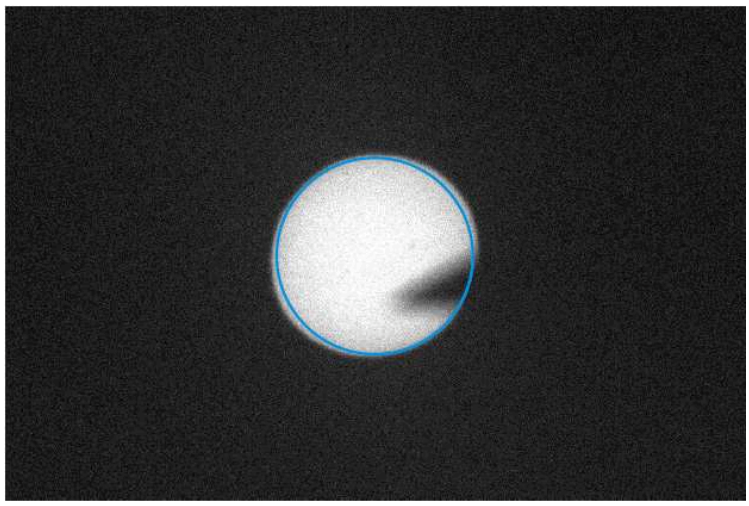

Figure 5.20: Apparent distortion of the shape of the Sun. The direction of the major axis of the distortion is at an angle of about 45° to the horizontal. A circle of the size of the expected diameter of the Sun is marked in blue for comparison. N.B.: Taken on 17th March in tracking mode, the solar center is expected to be above the visible pointer.

than on the other side and inner parts of the sphere become visible. This however, does not effect the picture analysis either, since only the crossing point is used as a reference, not the circle given by the TH-sphere. No parts of the Sun were cut off due to the slightly misaligned position of the TH-sphere.

Apparent Distortion of the Sun

A strange phenomenon could be observed, when filming through the upper part of the left window (see Fig. 5.21) at about 97°-98° horizontal (Azimuth AZ) and 6°-8° vertical (Height above horizon HA) under various conditions (Crosshairs on/off, different focus, both modes of following the Sun). An apparent deformation of the solar disk to an elliptic shape with an angle of $\approx 45°$ between the horizontal and its major axis. The axis was in the direction of the magnet movement from the lower-left corner to the upper-right one (see Fig. 5.20). The order of magnitude of this effect is approximately 1/60°, that is about 3% of the solar disk diameter. An ellipse is expected due to refraction, but its major axis and minor axis should be parallel to the horizontal and the vertical respectively. Two possible explanations were at hand:

- Inhomogenities in the plexiglass window of SR8
- Vibrations in the direction of the magnet movement

To test window inhomogeneities, a tiltable plate with concentric circles was designed to be put outside the window at specific positions in order to check if the circles would appear distorted. Since it was not possible at that point to move the magnet to the desired coordinates, a pipe was added to the plate, fixed perpendicular to its plane. It was equipped

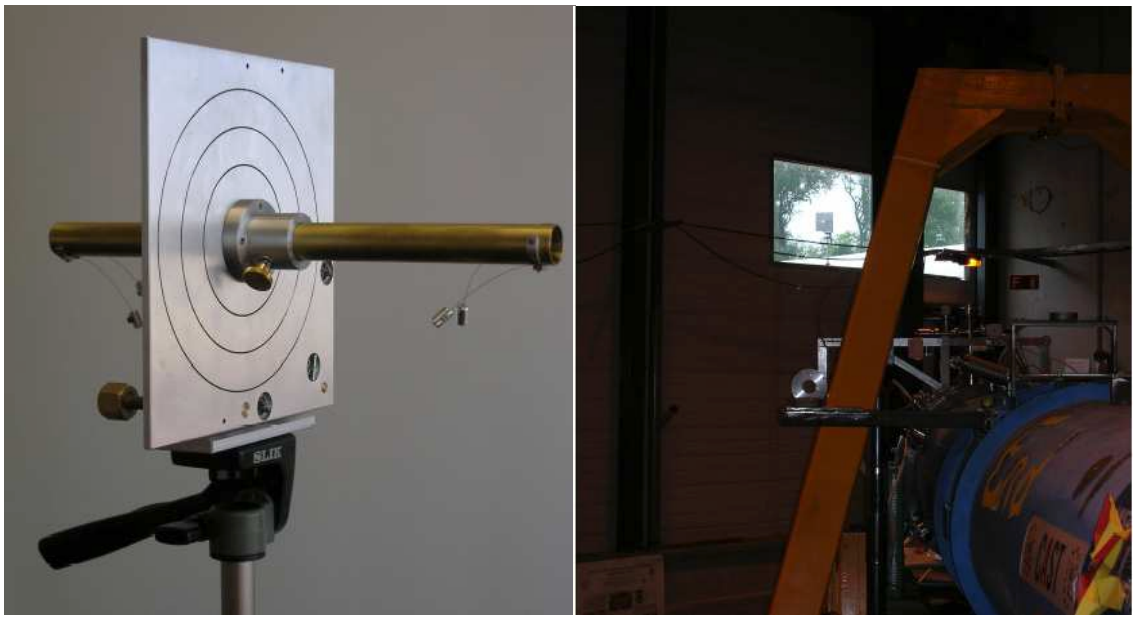

Figure 5.21: Left image: The tiltable plate used to check for window inhomogeneities. It has concentric circles and a pipe with crosshairs at each end to aim for the camera. Right image: The plate was placed outside the window of the experimental hall and observed with the camera mounted on its platform.

with two sets of crosshairs, one at each end, in order to aim at the camera. The plate and the setup can be seen in Figure 5.21. Several positions were tested, but no distortion could be observed (see Fig. 5.22). Probably the window was not the reason for the noticed deformations. However, it cannot be completely excluded as a source of this error, because only spot tests were performed and the chosen positions were not exact since the magnet could not be moved. In addition to this, the conditions in Spring were different than at the time of the test in July (e.g. temperature).

A second possible explanation for the distortion, namely vibrations of the magnet, was checked as well. If the magnet oscillates back and forth in its direction of movement, then the observed picture of the Sun should not be a true ellipse, but rather consist of two circles connected by two straight lines (see Fig. 5.23). Since there were only few pictures with the apparent distortion for each condition, the vibrations cannot be permanent ones. Furthermore, due to the fact that the straight part is rather short, the amplitude of the oscillations must be small. Thus, occasionally occurring vibrations with small amplitudes are a potential explanation for the observed distortion of the solar shape.

In the data of the filming in Fall 2005, no such effect of distortion seems to appear. The window was partly opened during the filming in September and strong vibrations of the magnet were noticable by hand. However, no apparent distortion could be observed in the pictures. The improvements of the setup after March 2005 were thus successful in suppressing vibrations: the supports of the filming system were made more rigid.

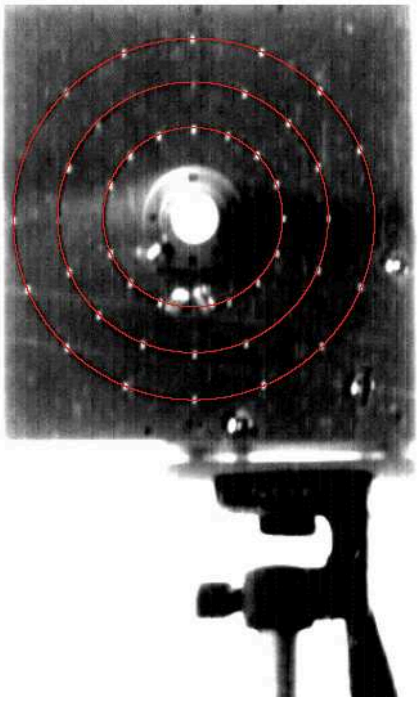

Figure 5.22: A picture of the plate with concentric circles to test the apparent distortion of the Sun occuring in some pictures. The bright spots on the disks are holes in the Aluminum plate along the marked circles to improve the visibility. No elliptic deformation of the circles is observable.

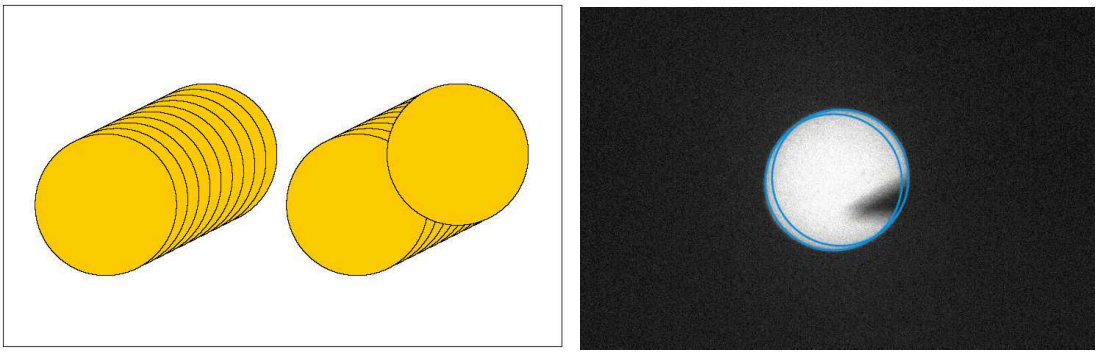

Figure 5.23: Left image: If there are vibrations along the direction of movement, two circles of the size of the Sun connected by two straight lines should be observable. Right image: Since the connecting part is very short, the apparent distortion can only be caused by vibrations with a small amplitude. The expected solar circle fits twice, supporting this scenario as a possible explanation for the deformation.

5.4 Results and Conclusions

In March 2005, the new filming setup was tested successfully under different conditions with the following results:

- Setup
  - For the filters, it is best to use them in various optical densities, so one can combine them and thus get a clear picture of the Sun no matter if it appears bright (in the hole) or dimmed (behind the trees).
  - The platform needs further improvement, i.e. it has to be made more rigid to damp oscillations and it should be made more flexible at the same time, in the sense that it is possible to change the position of the platform easily in order to be able to align the system well.
  - The 3D-support should be made more rigid as well to further damp oscillations.
  - The wires of the crosshairs have to be fixed in the right position mechanically. So far only tape was used to accomplish this.
  - The choice of the pointer is obvious: the precise pointer attached to a disk is much better to see in the pictures. However, the diameter of the disk's inner hole has to be made bigger in order to allow for a full sight of the Sun, even if the magnet was not exactly centered.
- Data Taking
  - The setting of the focus does not have a significant influence on the filming accuracy. However, changing the setting can cause unpredictable, but small shifts of the picture. The best solution would be not to change the focus at all.
  - The TH-sphere containing the crosshairs can stay in position during the filming if focus settings of 15 m to Infinity are used. However, it is not necessary to keep it in position during filming. Some shadows might occur on the edges of the solar disk, so it is recommendable to remove it after the alignment check.
  - An apparent distortion of the solar disk in some pictures may occasionally occur due to oscillations with a small amplitude. A more rigid setup should be able to eliminate this problem easily. It would be recommendable to film with an open window during the Fall 2005 to definitely exclude the plexiglass as a possible source for the apparent distortion.

The analysis of the pictures obtained in filming mode showed that, within statistical and systematic uncertainties of better than 0.029°, the CAST magnet is pointing at the center of the Sun. The mean value determined from all measured points during filming on March 16 and 21 is:

$$\begin{aligned} \bar{x}_{\text{Spring 2005}} &= -0.018^\circ \pm 0.002^\circ(\text{stat.}) \pm 0.026^\circ(\text{syst.}), \\ \bar{y}_{\text{Spring 2005}} &= -0.020^\circ \pm 0.001^\circ(\text{stat.}) \pm 0.028^\circ(\text{syst.}). \end{aligned}$$

The precision is much better than it was in previous filmings (accuracy at best 0.05°, which is the error of the alignment of the setup without any errors due to analysis or misalignment visible in the pictures). Since the region from which most axions are expected to emerge is about 0.054°-0.108° (10-20% of the solar diameter) and the total field of view for the magnet bore being 0.532°, the magnet alignment is sufficiantly accurate for the purposes of CAST. The precision of the filming system could be further improved to match the accuracy of the tracking system (better than 0.02°).

For the tracking mode pictures, the change of the refraction correction during the time of filming was not as large as expected (which would have been about 0.05°), however within the errors the change is compatible for experimental and theoretical data. The values of the observed correction were always smaller than the expected ones. This discrepancy was larger in the beginning of filming (up to 0.06°) and smaller towards the end ($\approx$ 0.02°). For the x-coordinate, which is not expected to change, a spread could be observed as well, indicating a movement of the magnet from a little too right to a little too left in the tracking.

In all data sets, the observed points are lower than the expected ones, implying that the magnet was pointing a bit too high ($\mathcal{O}(0.02°)$). This effect could be due to the fact that the magnet was not in its usual operating condition and thus lighter than usual at its end facing the Sun in the morning (TPC side). Maybe it is also an undetected systematic error applicable for all three days, not depending on the alignment.
One might say that there is a tendency that the observed solar center is more to the left than expected, implying that the magnet points to larger x-values during all three days of filming.
Thus, it seems as if the magnet is slightly ahead in time when tracking, which might suggest a minor error in the tracking software. The change in the vertical and the horizontal angle of the magnet movement during one minute of tracking is about 0.15°, hence the fact that the observed points are too low could result from being about 10 s ahead with the calculations in the tracking software. In any case, as said before, within the expected precision of the tracking and the given accuracy of the filming, the CAST magnet was pointing at the Sun in March 2005.

Chapter 6

Filming the Sun: Fall 2005

In late September 2005, the Sun was visible once again through the window of SR8, where the CAST magnet was prepared for the second phase of the experiment.
This chapter will inform first about the latest changes performed to further improve the filming accuracy by improving the setup used in Spring 2005 as well as by automatizing the analysis of the obtained pictures. This will be followed by a brief overview of the alignment and data taking procedure in Fall 2005 and, furthermore, the analysis of the obtained pictures on the three days of filming (September 23, 24 and 28) will be presented. Due to the fact that changes in the alignment as well as the setup were necessary, every day has to be treated separately as far as the systematic errors and the analysis are concerned. Some problems, which occurred during the filming, will be considered to ensure that no influence on the analysis results from them. Concluding, the results will be presented and an outlook on possible future improvements and changes can be found at the end of this chapter.

6.1 Improvements for September 2005

For the filming of the Sun in September 2005, the setup as well as the analysis were improved, based on the experience gathered in Spring 2005.

6.1.1 Improvements of the Setup

CCD Camera and the Optics

First, a follow-up model of the camera utilized in Spring 2005 was acquired, an ST-7XME, with the main difference that it has a USB Port rather than a parallel one, allowing a faster download of the pictures from the camera to the computer. Thus it is possible to take more pictures during filming and have therefore more statistics.
A new adapter ring to hold the optics, i.e. the same model of Olympus lenses as used in March, made the connection more rigid. Nevertheless, the optics still had some freedom of movement, thus they were not exactly perpendicular to the CCD chip, assuming that the sensitive part of the ST-7 is parallel to the body of the camera. There were suggestions

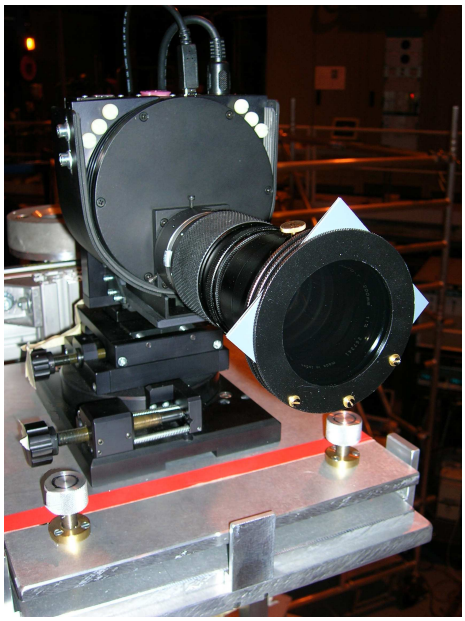

Figure 6.1: The new filter holder can be attached to the Olympus optics and it is possible to fix it in the desired position with a screw. It can hold two filters at the same time.

to fix the optics externally, but this would just have kept them in one of the extreme positions, i.e. looking slightly upwards or downwards, rather then keeping the lenses exactly horizontal.
In order to adjust the filters in a fixed position directly in front of the ST-7, a holder was built (see Fig. 6.1), which can be screwed to the optics. Two filters can be put on simultaneously, such that it is possible to combine different optical densities.

Platform and Camera Support

In order to make the alignment of the system easier and more rigid at the same time, a new platform for the filming setup was designed. The platform used in March 2005 was difficult to be placed in the right position for filming, because it was screwed underneath the carrier attached to the magnet. Therefore, the platform as well as the carrier were substituted and a construction of Rexroth Modular Profile Systems [117] was used in combination with a console to hold a tiltable platform instead. On top of this, the 3D-support for the ST-7, as it was used in Spring, could be put. Like this, all desirable movements of the setup can be performed (see Fig. 6.2 and Appendix B for a technical drawing):

- The distance to the magnet can be changed by moving the vertical profile along the two horizontal ones.
- The height can be varied by moving the console along the vertical profile.
- The inclination of the camera (to make it parallel to the magnet axis in up and down direction) can be changed by tilting the platform fixed on top of the console.

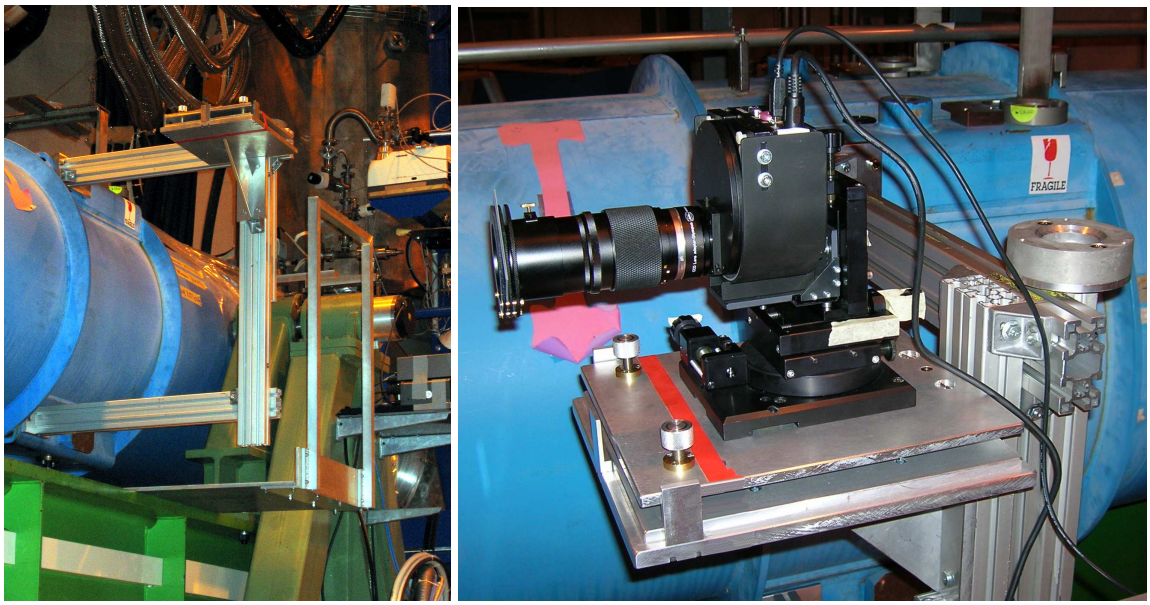

Figure 6.2: Left image: The new side arm for the filming system constructed by using Rexroth Modular Profile Systems. A console is attached to the vertical profile. It can be moved up and down to bring it into any desired position. Right image: The tiltable platform mounted on the console fixed to the Rexroth Profiles. It simplifies the vertical alignment of the optics. The 3D-support and the ST-7 are screwed to the inclinable platform.

- Fine adjustment can be performed by using the 3D-support of the camera described in Section 5.1.3, thus translations and rotation of the ST-7 are possible.

In the course of substituting the old support, a new safety platform to stand on during filming had to be built (see Appendix B, Fig. B.2), because more space as it was necessary for the setup in Spring 2005 was needed for the Rexroth profiles.
Also the 3D-support was made more rigid, by changing some parts and adding another set screw.

Crosshairs and Pointer

In order to stress the wires and get them as straight as possible, clamps with fixation screws were added on the TH-sphere holding the crosshairs instead of the tape applied in March. At the CERN workshop, the pointer within the disk was blackened and the diameter of its inner disk was increased in order to allow for a full view of the Sun, even if it did not appear completely centered. On the last day of filming, a double pointer was used. For this purpose, two disks, each with a pointer, where screwed together for better definition of the central point (see Fig. 6.3). This indeed simplifies the analysis.

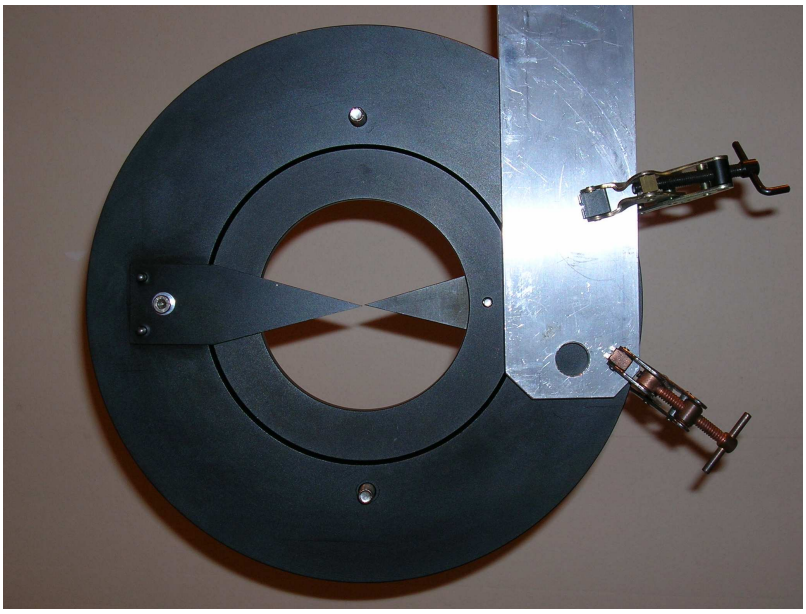

Figure 6.3: The double pointer consists of two disks screwed together, each of them having a pointer attached, which indicates the center of its disk. This makes it easier to determine the central point.

6.1.2 Improvements of the Analysis

The determination of the solar center from the pictures was automatized for the filming in September 2005 using a Matlab routine. An example program [118] offered in the Image Processing Toolbox of Matlab was used as a starting point and then extended to an applicable program for the filming. The function *bwtraceboundary* can be used to find the edges of the solar disk and a circle is fitted to the traced boundary. Since there are branches of trees preventing a full sight of the boundary of the solar disk in several pictures, performing only one tracing and fitting process is not good enough. Thus, the solar shape is determined many times using different starting points. The resulting fits are limited by excluding too small radii as well as too large ones. Then, the median of the radii and centers of the fitted circles is chosen, since it is more robust than the mean concerning outliers. The median is plotted in the original filming picture to make visual crosschecks possible. The reference point is taken from the alignment pictures[1] and saved along with the distance to the observed solar center in a file. This can then be used for spreadsheet analysis or plotting.
The big advantage of the Matlab program is that a large amount of pictures can be processed rather quickly and visual judgment can be used as a crosscheck. The source code of the utilized routine can be found in the Appendix C.

[1]It turned out that determining the reference point by visual judgment is more precise than using a routine, which had to trace the crosshairs in various lighting conditions.

6.2 Alignment and Data Taking

6.2.1 Alignment of the Setup

In principle, the same procedure was followed for the alignment in September as it was done in March 2005. The alignment had to be repeated every day before filming, since little improvements of the setup were necessary or the misalignment was too severe. For the distances of the pointer, the crosshairs and the surveyors' reference cup from the magnet tube V1 as well as for their height above the same pipe, the geometers' measurements led to (denotations as in Sect. 5.2.1 and Fig. 5.8, p. 68):

$$\begin{aligned} d_P = d_C = d_S &= 1014.2 \text{ mm} \\ h_P &= 408.4 \text{ mm} \\ h_C &= 408.3 \text{ mm} \\ h_S &= 408.3 \text{ mm} \end{aligned}$$

The height of the optics' center was measured to be equal to h_S and it was checked that the optics were in a horizontal position viewed from the Jura side. During the first filming, it turned out that the lenses were not parallel to the magnet if viewed from above. This led to a misalignment visible in the pictures, similar to the one of March 16 (see Fig. 5.10, p. 73). For the second day of filming, the setup was realigned, checking the parallelism of the optics with the magnet axis in height and distance. A second disk with pointer was attached to the first one and aligned for the third and last day of filming. The optics were checked again and so the best possible alignment was provided.

6.2.2 Study of Systematic Errors in the Alignment

The only significant error in the alignment results from the limits on the precision of the surveyors' measurements. The uncertainty is always better than 0.006°. The crosshairs were checked for accuracy by the geometers and no deviation of the central point could be observed. On the third day of filming (September 28), a superposition of several alignment pictures, in which the sphere with the wires was turned gradually (see Fig. 6.4) shows this as well: The crossing point of the wires does not change its position, which proves that it is well centered within the sphere.

6.2.3 Data Taking

Several attempts to film the Sun in Fall 2005 were made. On three days (September 23, 24 and 28) the Sun was eventually observable and successfully filmed. All filming sessions were done using the filming mode of the tracking software, i.e. a correction for atmospheric refraction was applied. During the first two days, the weather conditions were excellent and the Sun could be seen through the hole in the trees (see Fig. 5.1), while on the third day, when the alignment was best, it was indeed sunny, but the Sun was most of the time partly hidden behind the trees.

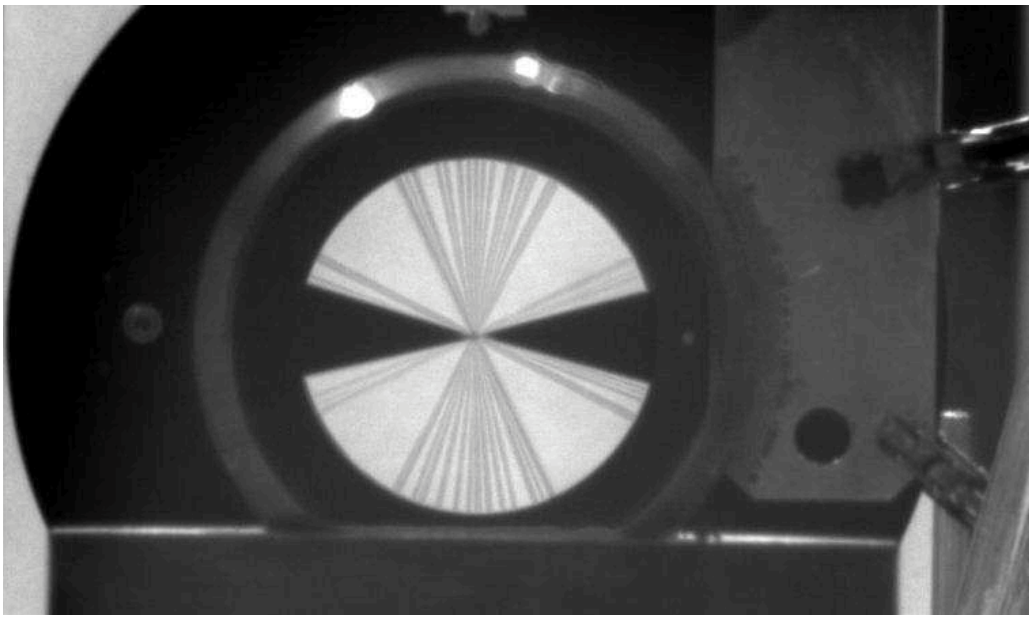

Figure 6.4: Superposition of several alignment pictures, in which the sphere with the crosshairs was gradually turned. The high precision can be appreciated by the fact that the crossing point of the wires stays in the same position for all pictures.

The magnet was almost under working conditions: As a compensation for the still unmounted TPC and its shielding a counterweight of 1.2 tons was installed. During the days of filming the magnet was in the process of being cooled down. Some of the occurring vibrations noticeable by hand might have resulted from this. However, they could not be observed as a disturbance in the pictures taken during alignment and filming the Sun.

6.3 Analysis

6.3.1 The First Day of Filming (23.09.2005)

Study of Systematics

The systematic error for the data of the first day is a combination of four different uncertainties:

- Uncertainty of the surveyors' measurements
- Error due to misalignment visible in pictures, i.e. the error of the shift made to correct data for the visible misalignment
- Uncertainty because the focus setting was changed
- Errors resulting from the analysis of the pictures with the Matlab routine

As mentioned before (Sect. 6.2.2), the uncertainty of the alignment by the surveyors is less than 0.006° for measured angles.
Due to the visible misalignment in the pictures, a shift of the data points had to be performed in the same way as done in Spring 2005. In x- and y-direction, it is 0.139° and 0.015° respectively. The error on this shift, resulting from the reading accuracy of the alignment pictures, is rather large: 0.077° and 0.015° for x- and y-direction respectively, since unfortunately the alignment images are blurred due to the lighting conditions.
Furthermore, from changing the focus setting, a contribution to the error of 0.02° results. Since the setting was only changed very rarely, this cannot be seen as a statistical variation but has to be considered as a systematic error (cp. frequent changes of focus in Spring 2005 during filming in tracking mode, Sect. 5.3.2).
For the determination of the observed center with the Matlab routine, the error of the Median is calculated by the program. It is different for every picture, but always smaller than 0.01° (typically around 0.003° in x and 0.006° in y-direction).
The total error combining all these uncertainties is thus approximately 0.0804° for the x-coordinate and 0.0276° for the y-direction.

Observations

Two different focus settings have been used for September 23: 30 m and Infinity. As can be seen in Figure 6.5, where only the errors for one setting are shown, the observed points of the solar center for the 30 m focus setting are spread more than those for the focus to Infinity. However within the errors they are all compatible. Infinity 1 and Infinity 2 denote the same focus setting, but the automatic function of the ST-7 to take pictures subsequently had to be restarted. Maybe the optics have also been touched in the course of doing so, thus causing a slight shift.
Averaging over the obtained points leads to the following values:

$$\begin{aligned}
\bar{x}_{30\mathrm{m}} &= -0.0242^\circ \pm 0.0005^\circ(\mathrm{stat.}) \pm 0.0803^\circ(\mathrm{syst.}),\\
\bar{y}_{30\mathrm{m}} &= -0.0063^\circ \pm 0.0005^\circ(\mathrm{stat.}) \pm 0.0274^\circ(\mathrm{syst.});\\
\bar{x}_{\mathrm{Infinity1}} &= -0.0360^\circ \pm 0.0002^\circ(\mathrm{stat.}) \pm 0.0804^\circ(\mathrm{syst.}),\\
\bar{y}_{\mathrm{Infinity1}} &= -0.0188^\circ \pm 0.0002^\circ(\mathrm{stat.}) \pm 0.0274^\circ(\mathrm{syst.});\\
\bar{x}_{\mathrm{Infinity2}} &= -0.0230^\circ \pm 0.0008^\circ(\mathrm{stat.}) \pm 0.0804^\circ(\mathrm{syst.}),\\
\bar{y}_{\mathrm{Infinity2}} &= -0.0177^\circ \pm 0.0009^\circ(\mathrm{stat.}) \pm 0.0274^\circ(\mathrm{syst.}).
\end{aligned}$$

In Figure 6.6, these values are plotted in comparison with the reference point. Furthermore, the acceptance region of the magnet and the circles for 10% as well as 20% of the solar diameter are plotted. The mean value of all observed points of this day can be calculated as:

$$\begin{aligned}
\bar{x}_{23.9.05} &= -0.026^\circ \pm 0.001^\circ(\mathrm{stat.}) \pm 0.080^\circ(\mathrm{syst.}),\\
\bar{y}_{23.9.05} &= -0.011^\circ \pm 0.001^\circ(\mathrm{stat.}) \pm 0.027^\circ(\mathrm{syst.}).
\end{aligned}$$

As in Spring 2005, the observed points are slightly too low and a bit too much to the left. The deviation is well within the error, but nevertheless it indicates that the magnet is

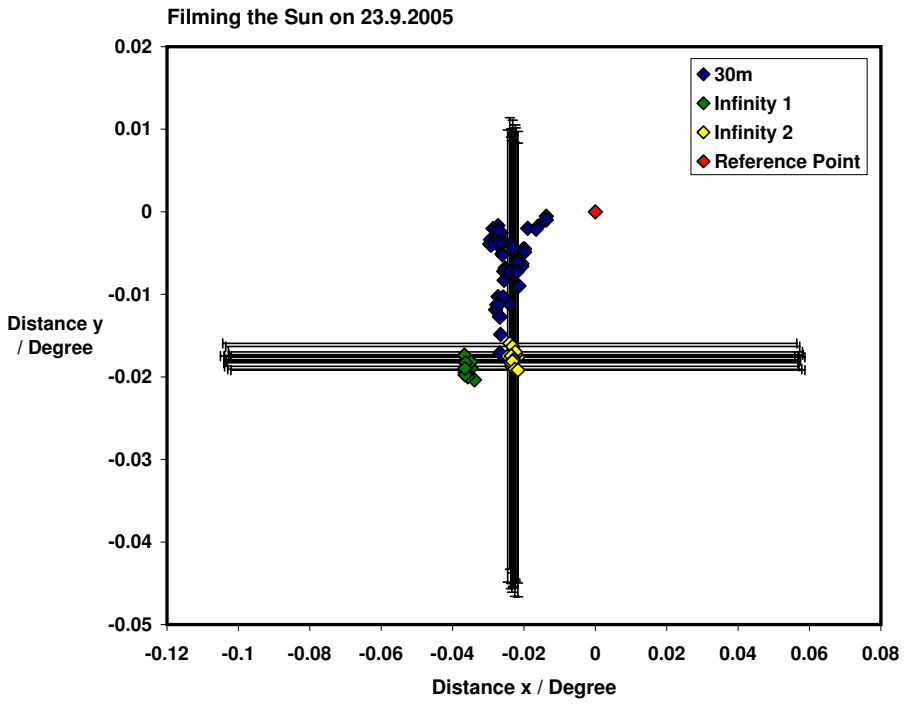

Figure 6.5: Distances in x- and y-direction of the observed solar center from the reference point on September 23. The reference point was chosen to be the origin of the coordinate system. To provide a better overview, the systematic errors are included for one focus setting only.

pointing a bit to the upper right of the solar central point. Since the filming setup has been changed and everything had been installed newly after Spring, this effect should not result from the filming setup. Also the condition of the magnet cannot be the cause, because in September a counterweight to compensate for the missing TPC and its shielding was in place. In any case, within the precision of tracking and filming, the magnet is pointing to the solar center.

6.3.2 The Second Day of Filming (24.09.2005)

Study of Systematics

Basically, the same systematic errors as for the previous day have to be considered. A shift in coordinates was however not necessary, since no difference between the tip of the pointer and the crosshairs was observable. Nevertheless, there is an error on the determination of a shift from the reading accuracy of the alignment pictures, which is 0.0206° for the x-coordinate and 0.0077° for the y-direction. However, these uncertainties are much smaller than for the previous day, due to the fact that the alignment pictures were clear and sharp. The error for the Matlab analysis here is again smaller than 0.01°, however typically around 0.004° for x and 0.003° for the y-direction. Combining all errors gives uncertainties of the order $\mathcal{O}(0.031°)$ for x and $\mathcal{O}(0.030°)$ for y.

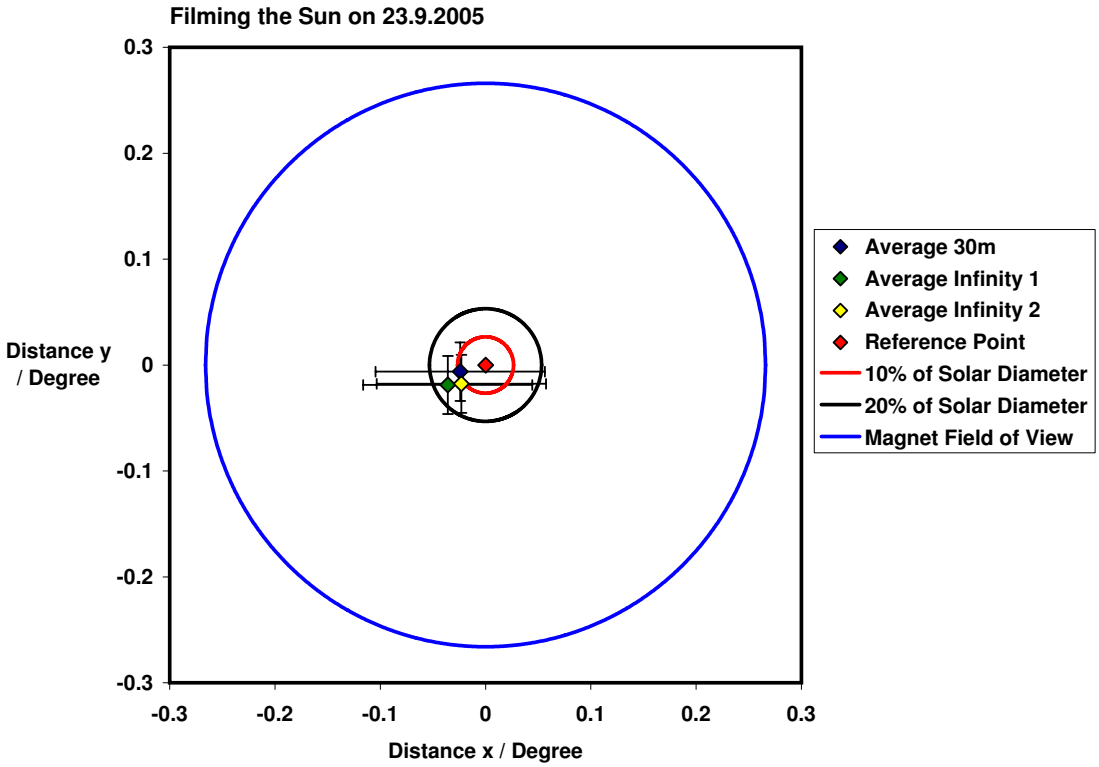

Figure 6.6: Average of the distances in x- and y-direction of the observed solar center from the reference point on September 23. The data points were averaged per focus setting. The acceptance region of the magnet as well as disks of 10% and 20% of the solar diameter are included in the plot.

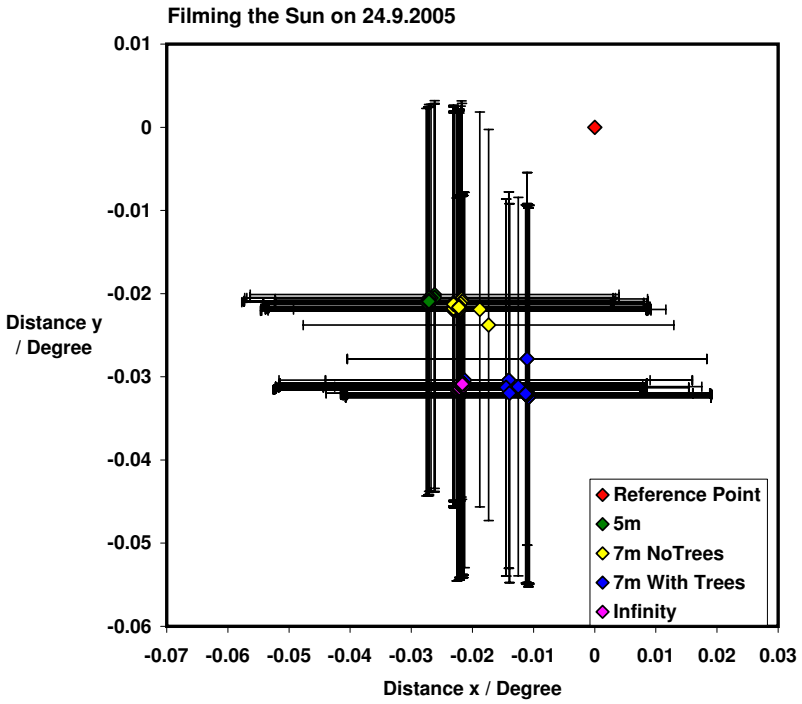

Figure 6.7: Observed distances in x- and y-direction of the solar center from the reference point on September 24. The systematic errors are included.

Observations

The focus settings used on the second day of filming were 5 m, 7 m and Infinity. For the analysis the pictures taken with a focus setting of 7 m were sorted in two groups (trees visible inside the solar disk and no branches disturbing the view) in order to adjust the Matlab routine to obtain more accurate fits. Also for this day, the observed points are lower and more to the left side of the expected solar center (see Fig. 6.7), but still well within the acceptable region. Averaging the points of each focus setting and plotting them together with disks of 10% and 20% of the solar diameter as well as the magnet acceptance region (see Fig. 6.8), one obtains the following mean values with the according statistical and systematic errors:

$$
\begin{aligned}
\bar{x}_{\mathrm{5m}} &= -0.0269^\circ \pm 0.0002^\circ(\mathrm{stat.}) \pm 0.0302^\circ(\mathrm{syst.}),\\
\bar{y}_{\mathrm{5m}} &= -0.0207^\circ \pm 0.0001^\circ(\mathrm{stat.}) \pm 0.0233^\circ(\mathrm{syst.});\\
\bar{x}_{\mathrm{7m,\ NoTrees}} &= -0.0223^\circ \pm 0.0002^\circ(\mathrm{stat.}) \pm 0.0312^\circ(\mathrm{syst.}),\\
\bar{y}_{\mathrm{7m,\ NoTrees}} &= -0.0217^\circ \pm 0.0001^\circ(\mathrm{stat.}) \pm 0.0237^\circ(\mathrm{syst.});\\
\bar{x}_{\mathrm{7m,\ WithTrees}} &= -0.0121^\circ \pm 0.0004^\circ(\mathrm{stat.}) \pm 0.0300^\circ(\mathrm{syst.}),\\
\bar{y}_{\mathrm{7m,\ WithTrees}} &= -0.0315^\circ \pm 0.0003^\circ(\mathrm{stat.}) \pm 0.0227^\circ(\mathrm{syst.});\\
\bar{x}_{\mathrm{Infinity}} &= -0.0219^\circ \pm 0.0001^\circ(\mathrm{stat.}) \pm 0.0300^\circ(\mathrm{syst.}),\\
\bar{y}_{\mathrm{Infinity}} &= -0.0312^\circ \pm 0.0001^\circ(\mathrm{stat.}) \pm 0.0230^\circ(\mathrm{syst.}).
\end{aligned}
$$

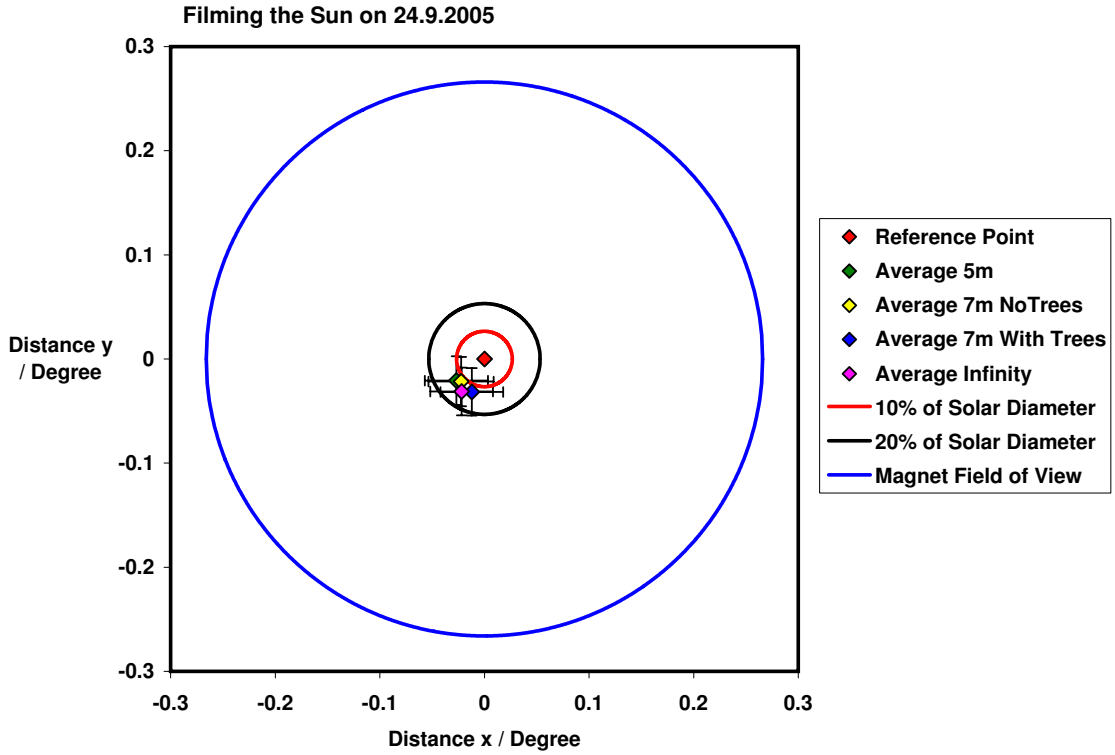

Figure 6.8: Average (per focus setting) of the observed distances in x- and y-direction of the solar center from the reference point on September 24. The acceptance region of the magnet as well as disks of 10% and 20% of the solar diameter are plotted, too.

The mean value of all observed points of this day can be calculated as:

$$\bar{x}_{24.9.05} = -0.020^\circ \pm 0.001^\circ(\text{stat.}) \pm 0.030^\circ(\text{syst.}),$$
$$\bar{y}_{24.9.05} = -0.027^\circ \pm 0.001^\circ(\text{stat.}) \pm 0.023^\circ(\text{syst.}).$$

As for September 23, also for this day of filming, the observed points agree with the expected pointing position within the given tracking accuracy of 0.02° and the calculated errors, and thus the magnet is pointing to the Sun.
Although the systematic error on September 23 was larger due to known reasons, we combine the results of filming for September 23 and 24. However, this mean value does not really reflect the achievable precision of the filming system. The result of the combination of both days is:

$$\bar{x}_{23\&24.9.05} = -0.023^\circ \pm 0.001^\circ(\text{stat.}) \pm 0.054^\circ(\text{syst.}),$$
$$\bar{y}_{23\&24.9.05} = -0.019^\circ \pm 0.001^\circ(\text{stat.}) \pm 0.025^\circ(\text{syst.}).$$

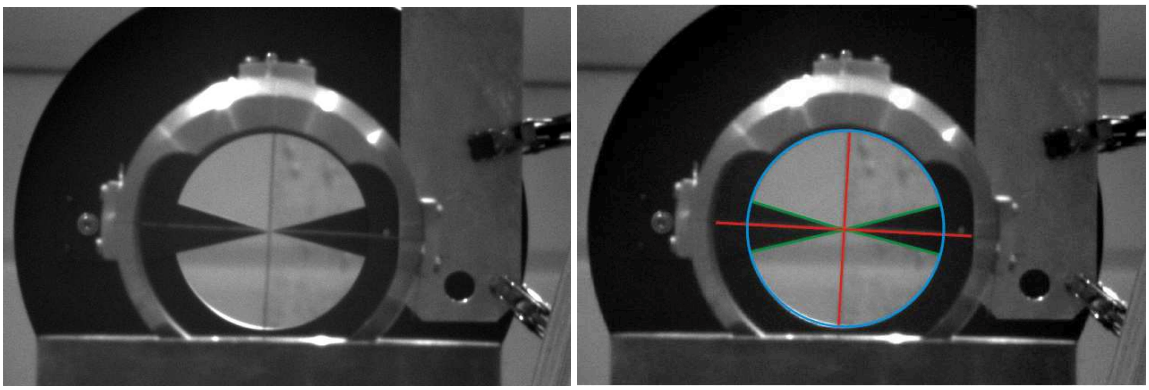

Figure 6.9: Left Image: Alignment picture taken on September 28. The two pointers and the crosshairs are in line. Right Image: For reference in filming pictures the pointers and the crosshairs were marked in green and red respectively. The blue circle denotes the area in which a full view of the Sun is possible in order to later check in the filming pictures if parts of the solar disk were cut off.

6.3.3 The Third Day of Filming (28.09.2005)

The third day of filming differs from the others in several ways. Firstly, the double pointer was used and thus the position of the reference point was easier to determine. In addition to this, the alignment for this day was better than for the previous days, not demanding a shift of data points to compensate for a visible misalignment. Moreover, sharp alignment pictures reduced the error on the determination of the misalignment. A further distinguishing feature was that the Sun was partly hidden behind the trees instead of being completely observable. Thus a different method of analyzing the pictures was required.

Study of Systematics

The most precise alignment of the solar filming in Fall 2005 was achieved for the last day of filming, when using the double pointer (see Fig. 6.9). No change of focus was done after the alignment was accomplished and checked by the surveyor. This happened at a focus setting between 5 and 7 m, such that crosshairs as well as pointer could be seen simultaneously as sharp as possible. No shifts in x and y due to a change of focus can occur, however at the expense of getting a slightly blurred image of the Sun, due to the fact that it is out of focus. The remaining sources of systematic errors can thus be summarized as:

- Uncertainty of the surveyors' measurements
- Error in checking for visible misalignment (No misalignment observable)
- Errors resulting from the analysis of the pictures with the Matlab routine
- Uncertainty from processing the images (Adding several pictures to compensate for disturbing branches)

As usual the uncertainty of the surveyors' measurements is given as less than 0.006° for measured angles.

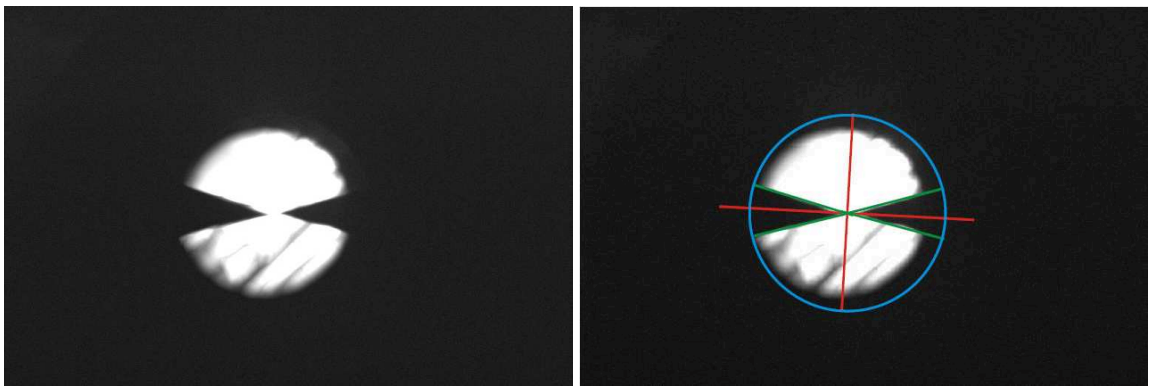

Figure 6.10: Left Image: Superposition of about 75 pictures taken during filming on September 28. Right Image: For reference the crosshairs, the pointers and the circle, within which a full view of the Sun is possible (i.e no disturbances due to disk or sphere occur), are added in the picture.

When checking for a visible misalignment in the pictures, the error in both x- and y-direction is less than two pixels, i.e. $< 0.0052°$.
From using the Matlab routine an uncertainty of about $0.0150°$ results, due to the choice of the reference point and the fit of the circle.
From processing the pictures an error of not more than $0.0077°$ contributes to the total systematic error, which can thus be calulated to be less than $0.019°$.

Observations

Due to the fact, that trees were considerably obstructing the view of the Sun, it was not possible to use single pictures in order to obtain the observed solar centers by tracing the boundaries and fitting the appropriate circles with the Matlab routine. Instead, about 75 pictures were superimposed. By requiring that only the brighter parts of each image are shown in the combined picture, one is able to eliminate branches obstructing the view of the solar disk. However, the obtained image of the solar disk does not show an exactly circular shape (see Fig. 6.10). Furthermore, the right pointer seems to be smaller than the left one. This is an effect from superimposing the pictures due to reflections. By using the references obtained from Fig. 6.9, this latter problem can be solved (see right image in Fig. 6.10).
The observed distance of the solar center in the superimposed picture from the reference point obtained by a Matlab fit on the combined image is:

$$x_{28.9.2005} = -0.014° \pm 0.019°(\text{syst.}),$$
$$y_{28.9.2005} = -0.004° \pm 0.019°(\text{syst.}).$$

Once more, this shows that the magnet is pointing to the center of the Sun. The observed point is slightly to the left of the expected center and (hardly noticeable) too low. However, within the given precision of the filming system and the accuracy of the tracking, everything looks perfect.

6.3.4 General Problems and Additional Tests

Shifts of the Picture

After the alignment on the 27th September for the third day of filming, no part of the setup was touched or moved anymore, except for the filterholder. Nevertheless, when rechecking the alignment directly before starting to film in the morning of September 28, the whole picture appeared shifted. However, the setup was still parallel to the magnet axis, which could be seen in the alignment pictures. So the whole system must have moved parallel over night or while putting the filterholder in place. In any case, this did not influence the analysis.
Tests on the following days did not show the same effect again. Probably the weight of the filter holder shifted the image without changing the alignment.

Influence of the Filterholder

In some pictures taken with the filter holder in place, parts of the image cannot be seen. The pictures look as if they suffer from a vignetting effect, i.e the outer parts of the pictures are dark. This happened already before any filter is inserted into the filter holder, thus excluding the plastic frame of the filter itself as a possible cause for the effect. Since at any time the sphere, the crosshairs and the Sun are completely within the accessible part of the pictures, no problems can result from this effect.

6.4 Results and Conclusions

The improved system of March 2005 was used for the solar filming in Fall 2005. The new camera was placed on a novel and more rigid support allowing easier alignment by possible movements in various directions. Thus, no vibration effects could be observed in the pictures. Furthermore the analysis was automatized allowing faster processing of the obtained images of the Sun.
All three days of filming showed that, within the given precision of the filming system, the magnet was always pointing to the solar center. None the less, as already noticed in March, the observed solar centers are a little bit too low and too much to the left with respect to the expectation, thus indicating that the magnet is pointing too high and slightly too much to the right. This cannot result from the missing weight of the TPC and its shielding, since a counterweight was installed in the Fall of 2005. Neither is a systematic error of the filming setup likely to be responsible for this discrepancy, because the entire system was completely reinstalled in Fall 2005. Maybe the software for steering the magnet is slightly ahead in calculating and tracking the solar position (about 10 s).
Overall, the precision of the filming system was further improved to match the accuracy of the tracking itself. While for the first day of filming the precision was not as high as it could have been (about 0.080° for the x-coordinate and 0.028° for the y-direction) due to insufficient alignment pictures, it was improved for the second day, thus being of the order $\mathcal{O}(0.03°)$ for both coordinates. With the best alignment on the third day, however, the

precision of the tracking system could be matched by achieving an accuracy of better than 0.02°. The results obtained for the first two days of filming were:

$$\bar{x}_{23.9.05} = -0.026^\circ \pm 0.001^\circ(\text{stat.}) \pm 0.080^\circ(\text{syst.}),$$
$$\bar{y}_{23.9.05} = -0.011^\circ \pm 0.001^\circ(\text{stat.}) \pm 0.027^\circ(\text{syst.});$$

$$\bar{x}_{24.9.05} = -0.020^\circ \pm 0.001^\circ(\text{stat.}) \pm 0.030^\circ(\text{syst.}),$$
$$\bar{y}_{24.9.05} = -0.027^\circ \pm 0.001^\circ(\text{stat.}) \pm 0.023^\circ(\text{syst.}).$$

For the third day (September 28), a superposition of several pictures was used, since branches were obstructing the view of the Sun. This lead to the following result:

$$x_{28.9.2005} = -0.014^\circ \pm 0.019^\circ(\text{syst.}),$$
$$y_{28.9.2005} = -0.004^\circ \pm 0.019^\circ(\text{syst.}).$$

All in all, it is possible to say that within the desired precision, the CAST magnet is pointing to the center of the Sun. Nevertheless, continuing the optical crosschecks is highly recommendable to consistently provide information on possible changes in the tracking behavior of the magnet.

6.5 Future Improvements

6.5.1 Setup

For optimizing the quality of the pictures, the Taylor-Hobson sphere with the crosshairs should be blackened from the outside (as it is from the inside), in order to avoid as much reflections as possible.
Furthermore, the pointer was only clamped to its support and thus it was difficult to move and adjust it for the alignment. Maybe the Rexroth profiles used for the support of the optical system can be utilized here as well. This should not be difficult to accomplish, but it needs to be designed.
A new double pointer might be useful. It should not consist of two disks screwed together, but rather of one disk with two pointers attached. Thus, a mismatch of the tips in the z-direction can be avoided, although this does not influence the alignment of the filming. However, for a better visual appearance of the center with the same focus setting it would, however, be recommendable.
The surveyors' cup must be attached to the vertical profile holding the console for the camera. Then, the filming system and the surveyors' cup can be moved simultaneously, allowing for both the camera and the cup used for alignment of pointer and crosshairs are in line.

6.5.2 Alignment

A possible way to align the camera more exactly with the magnet axis, as suggested in a recent collaboration meeting, is to use the same system as the CCD detector group utilizes in order to align the telescope [119]. For this purpose a laser beam is aligned with the magnet by using a theodolite. It is then sent through the tube V1 and its image can be observed on the CCD chip, thus providing information on where a potential axion signal could be found within the sensitive area. The same principle can be employed for the camera, but a new mounting for the laser and the theodolite would be necessary, because the optical axis of the filming setup is higher than the tube V1, which is used to align the telescope of the CCD detector [120].

6.5.3 Alternative Crosschecking Methods

In addition to the filming of the Sun, other independent crosschecks have been suggested. These might be necessary, if recent calculations about an apparent discrepancy of the galactic coordinates turn out to be true [121]. It seems as if there was a difference between the galactic coordinates in the logfiles of the CAST experiment and the theoretical ones calculated for the Sun. According to the mentioned discussion, the latitude shows deviations from theory of up to $\pm 1^\circ$. For the galactic longitude the maximum deviation might be as large as 2°. The deviations are minimal around the vernal and the autumnal equinox, i.e. at the time when filming is possible, and thus these calculations can unfortunately not be checked by filming the Sun. A solution could be to film stars instead of the Sun, which would allow crosschecks at virtually any time of the year. Unlike the Sun, some stars should always be visible through the window of the experimental hall. Maybe this observations of the nightly sky can be done using the ST-7. Otherwise a special star tracker[2] offered by the LLNL[3] might be applied to crosscheck the accuracy of the tracking system. At the moment, observations of stars are almost impossible due to emergency lighting in the experimental area, which cannot be turned off.
It should be mentioned that if the azimuth and the height above the horizon are considered, the difference between the logged coordinates and the theoretical ones is well within the tracking precision, i.e. no discrepancy as for galactical coordinates is observable. So, maybe there is just a misunderstanding in interpreting the data in the logfiles and the observed apparent deviations in the galactic coordinates turn out to be not significant after all.

[2]This star tracker is a combination of a telescope and a special software, which enables the exact determination of a location by comparing observed stars with a star catalog.
[3]Lawrence Livermore National Laboratory

Chapter 7

Summary

The CERN Axion Solar Telescope (CAST) searches for solar axions by employing the Primakoff effect. A superconducting magnet, which is able to follow the Sun, provides the magnetic field for the axion-to-photon conversion.
In this thesis an optical crosscheck (Solar Filming) of the tracking system steering the magnet is described in detail. The improvements of the already existing system to film the Sun and the analysis of the solar images obtained during the solar filming in March and September 2005 are the main objective of this work. Since a high pointing accuracy of the tracking system is necessary for detecting axions, a high precision of the filming setup was essential to be able to make conclusive statements on whether the CAST magnet is pointing to the solar core. The precision of the system used to film the Sun until March 2005, was about 0.05°. This accuracy, however, did only include the accuracy of the alignment. No further errors were initially taken into account.

The former filming setup consisted of a small telescope and a webcam. This was substituted by a CCD camera and appropriate optics (ST-7 from SBIG with Olympus lenses) resulting in a much better resolution. A complete system to mount the camera was designed and installed at the experimental site. This includes a new carrier constructed of Bosch Rexroth Systems and attached to the left side of the magnet as well as an inclinable platform and a 3D-support for the camera, in order to be able to align it precisely with the magnet axis. A novel method to assure that the optical axis is indeed parallel with the magnet pipe was applied, making use of two different targets: A Taylor-Hobson sphere with wires crossing its center and a pointer. They were aligned with the magnet and then the camera was placed such that both targets could be seen in line. Several additional changes were made concerning, for example, the filters used to film the Sun. The advantages of the final setup are its simultaneous stability and flexibility. Since the system is built to be as rigid as possible, it is able to damp occurring vibrations, while at the same time it is quite movable, thus facilitating the alignment by adjusting it to the desired position.

The filming in Spring 2005 was primarily seen as an opportunity to test and improve the new system, since the magnet was not in its usual operating condition. Nonetheless,

the Sun could be filmed on three days and the images were analyzed. In Fall 2005, data were successfully taken on three days. While the analysis of the images taken in March was still performed by visual judgment, it was automatized for the measurements in September 2005 by using a Matlab routine, which is able to determine the observed solar center in the pictures.

In Spring 2005, the images taken in filming mode, i.e. with correction for atmospheric refraction applied when following the Sun, were able to show that the CAST magnet is pointing to the center of the Sun within statistical and systematic uncertainties of always less than 0.029°. The average distances between observed and expected solar center, i.e. the point where the magnet is aiming at, for Spring were:

$$\begin{aligned} \bar{x}_{\text{Spring 2005}} &= -0.018^\circ \pm 0.002^\circ(\text{stat.}) \pm 0.026^\circ(\text{syst.}), \\ \bar{y}_{\text{Spring 2005}} &= -0.020^\circ \pm 0.001^\circ(\text{stat.}) \pm 0.028^\circ(\text{syst.}). \end{aligned}$$

Considering the core of the Sun from which most axions are emerging (0.054°-0.108°) and the magnet acceptance region (about 0.532°), the desired tracking accuracy (always better than 0.02°) for CAST is thus confirmed.
A direct check of the tracking software, i.e. without using the filming mode to correct for refraction but filming in the usual tracking mode to follow the Sun, had a precision of the order $\mathcal{O}(0.03^\circ)$. Images taken while filming in tracking mode, showed that the change of the observed refraction during tracking was smaller than expected, however compatible with theory within the errors. A slight drift in the x coordinate, which is expected to stay the same, was observed during this filming in tracking mode, indicating a movement of the magnet from a little too right to a little too left in the tracking. But within the error of the solar filming, the magnet was pointing at the solar center.

For Fall 2005, the precision was typically around 0.027°. Due to blurred alignment pictures, the worst case limited the precision to 0.081°, while an accuracy better than 0.019° could be achieved at best, and thus the precision was further improved in comparison with Spring 2005. The results for the first two days can be summarized as:

$$\begin{aligned} \bar{x}_{23.9.05} &= -0.026^\circ \pm 0.001^\circ(\text{stat.}) \pm 0.080^\circ(\text{syst.}), \\ \bar{y}_{23.9.05} &= -0.011^\circ \pm 0.001^\circ(\text{stat.}) \pm 0.027^\circ(\text{syst.}); \end{aligned}$$

$$\begin{aligned} \bar{x}_{24.9.05} &= -0.020^\circ \pm 0.001^\circ(\text{stat.}) \pm 0.030^\circ(\text{syst.}), \\ \bar{y}_{24.9.05} &= -0.027^\circ \pm 0.001^\circ(\text{stat.}) \pm 0.023^\circ(\text{syst.}). \end{aligned}$$

For the third day, a superposition of several pictures was used, since branches were obstructing the view of the Sun, resulting in:

$$\begin{aligned} x_{28.9.05} &= -0.014^\circ \pm 0.019^\circ(\text{syst.}), \\ y_{28.9.05} &= -0.004^\circ \pm 0.019^\circ(\text{syst.}). \end{aligned}$$

Thus, CAST is pointing to the solar center within the precision of the filming setup, which is able to match the accuracy of the tracking system.
Nevertheless, it should be mentioned that all observed points in March as well as in September 2005 were lower and more to left side than expected. This indicates that the magnet is pointing slightly too high and a bit too much to the right, thus being about 10 s ahead in time when tracking. Since this apparent discrepancy is of the order $\mathcal{O}(0.02^\circ)$, it is within the errors of tracking and filming.

Since most uncertainties originate from the alignment and the changing of the focus setting during filming causing shifts of the image, alternative crosschecking methods should be considered for the future.
A first step could be simply to change the alignment procedure of the present filming setup by using a laser as it is utilized to bring the telescope of the CCD in line with the magnet bore. This could improve the alignment and make changing the focus setting unnecessary.
A different approach might be to use either the ST-7 or a special star tracker in order to film stars instead of the Sun. This would allow to constantly crosscheck the magnet movement, since different stars would be observable through the window of the experimental hall at virtually any time of the year, while for the Sun this opportunity is only given twice per annum.

With the completion of CAST's first phase, the existing limits on the coupling constant $g_{a\gamma}$ have already been improved by a factor of 5 using the data obtained in 2003 with no observable signal above background. Further improvements are expected from the 2004 data analysis. At the moment, CAST is being prepared for its second phase. The experiment will extend the axion mass range, which will enable it to enter the theoretical axion regions as the first laboratory experiment. CAST is pointing at the Sun and ready to explore new shores, or as Christopher Columbus once supposedly said:

> Following the light of the Sun, we left the Old World.

Appendix A

Setup for Spring 2005

In this part, technical drawings of the ST-7 CCD camera from SBIG can be found: Dimensions are given in Figure A.1 and information concerning the focal plane are to be found in Figure A.2.
The 3D-support for the ST-7, which was designed and constructed at the mechanical workshop of the Albert-Ludwigs-Universität Freiburg, is shown in Figure A.3.
The 3D-support of the camera was too high to use the optical axis for the best view as determined with the old setup in Fall 2004. Thus, it was necessary to construct a platform situated lower than the original one. It was screwed to the carrier holding the old platform and can be seen in Figure A.4.

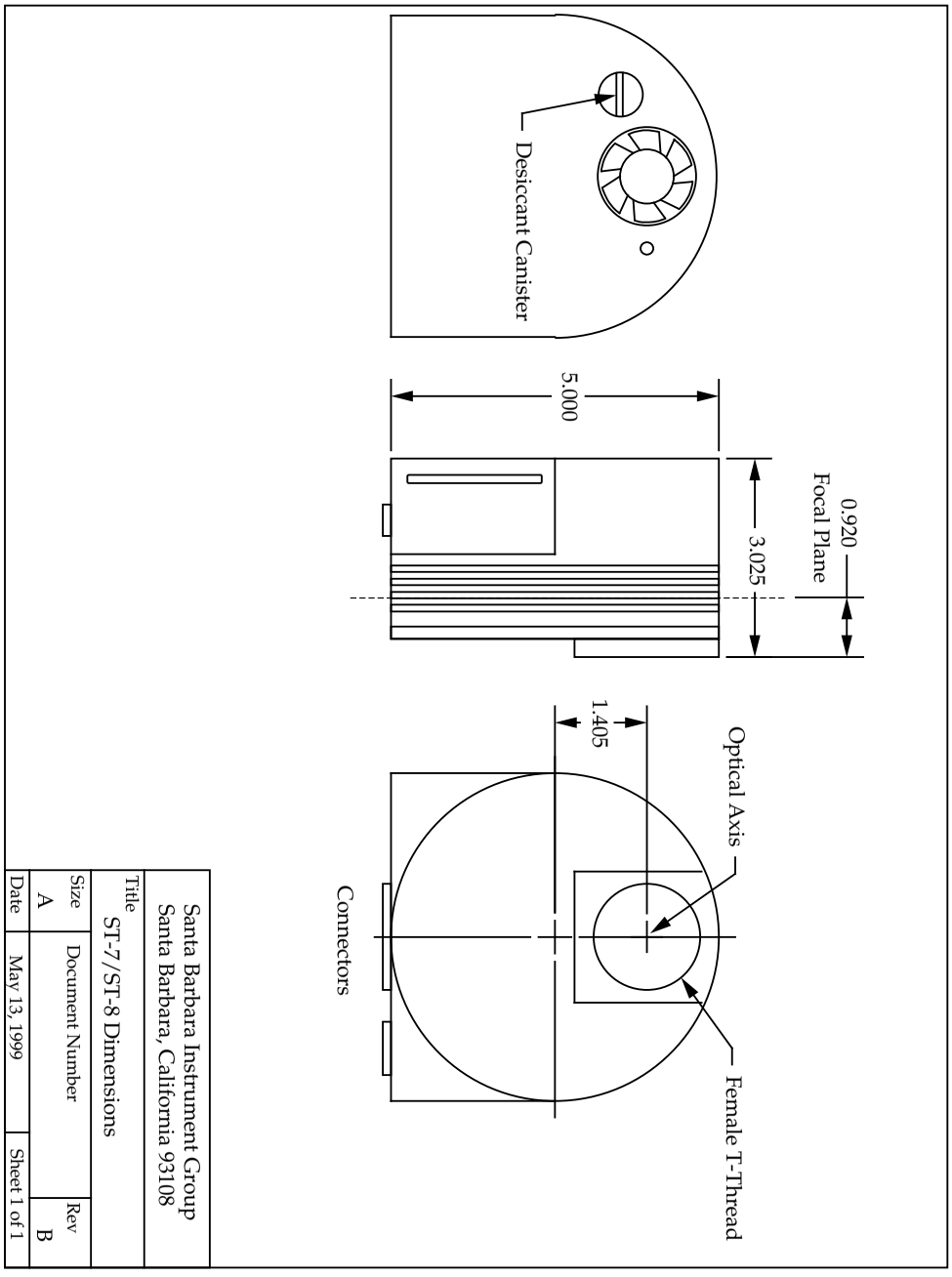

Figure A.1: Dimensions of the ST-7 from SBIG. If not denoted otherwise the dimensions are given in inch. The figure was taken from [122].

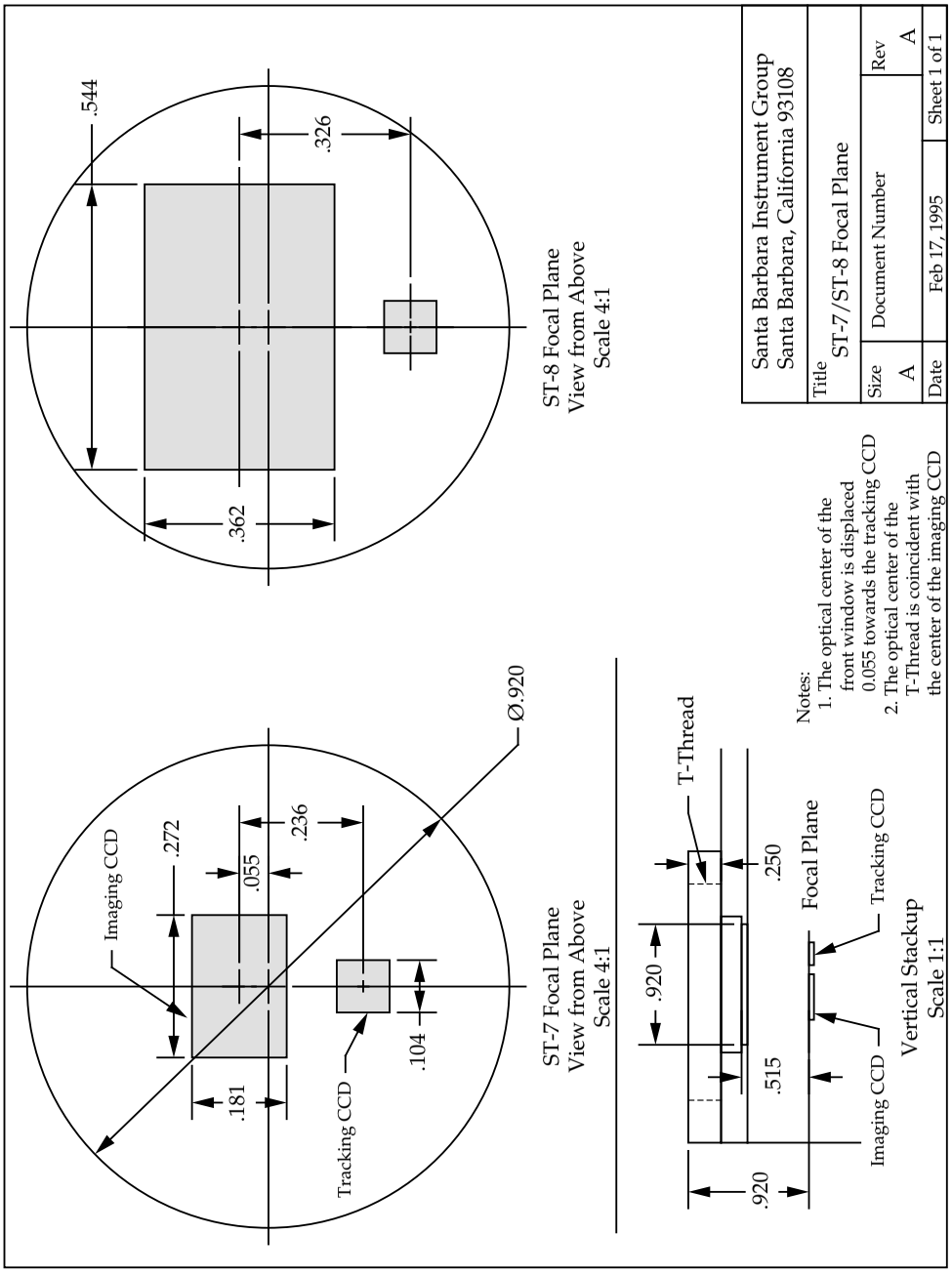

Figure A.2: Technical drawing of the ST-7 with dimensions concerning its focal plane. If not denoted otherwise the dimensions are given in inch. For further details see [122].

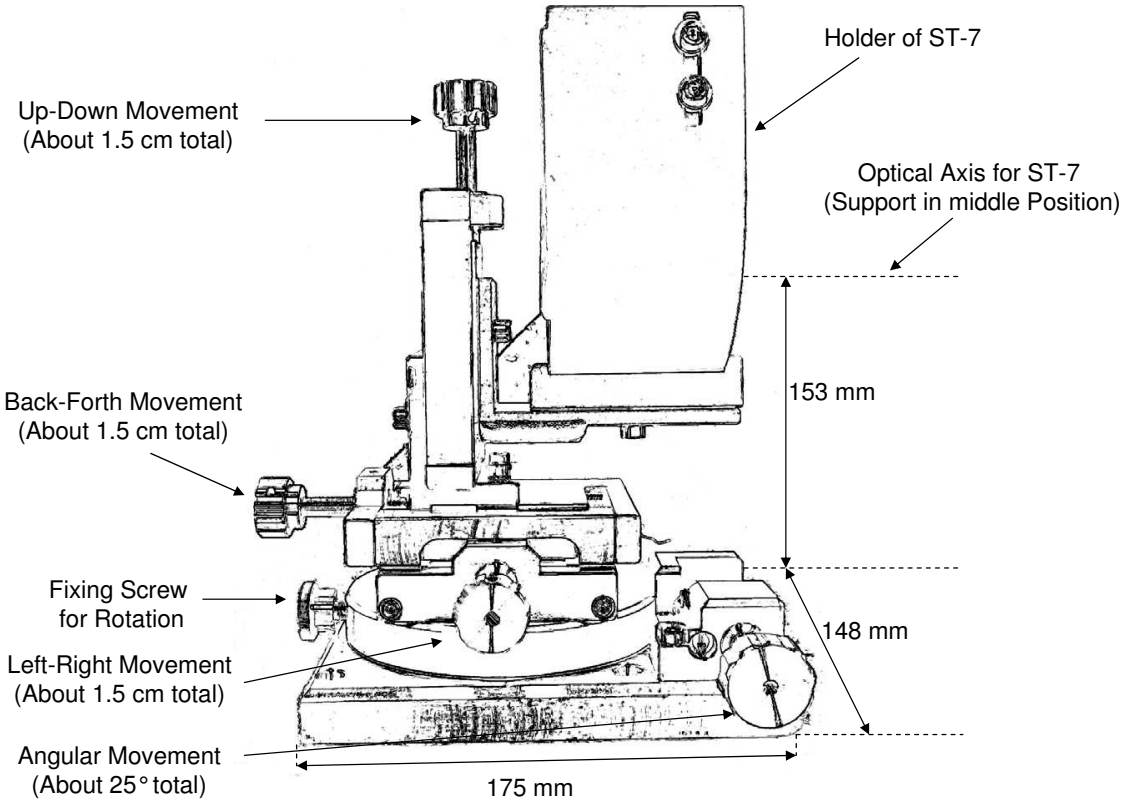

Figure A.3: Dimensions and functions of the 3D-support for the ST-7. It was constructed at the mechanical workshop of the Albert-Ludwigs-Universität Freiburg.

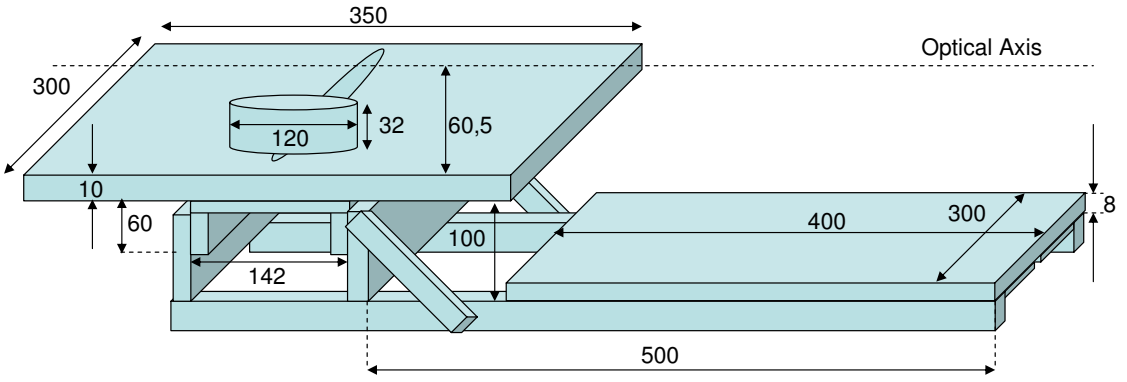

Figure A.4: The platform used in Spring 2005 (lower right) was attached to the carrier (left in image) on the Jura side of the magnet, which supported the old platform. Dimensions are given in Millimeter. The platform was constructed at the mechanical workshop of the Albert-Ludwigs-Universität Freiburg.

Appendix B

Setup for Fall 2005

For Fall 2005, a new platform was constructed as shown in Figure B.1. It is more rigid than the one built in March 2005, in order to damp occurring vibrations. At the same time, it was made to be more flexible allowing movement in various directions, such that the alignment was simplified. To accomplish both goals simultaneously, a construction of Bosch Rexroth Modular Profile Systems was used. A console is fixed to a vertical profile connecting the two horizontal profiles, which are in turn attached to the magnet. The vertical connection can be moved left and right along the horizontal ones, while in addition to this, it is possible to adjust the height of the console along the vertical profile. In order to bring the camera and the optics into a position parallel to the magnet axis, a tiltable platform is mounted on the console. On top of this whole construction, the 3D-support can be screwed and used for the fine-adjustment by allowing movements in x, y and z-direction as well as rotations around the vertical axis.
For safety reasons, a platform with a railing was originally installed on one side of the magnet. It was meant to prevent people from falling off the magnet while filming. Because the railing was obstructing the movement of the newly designed Bosch Rexroth construction, the safety platform and its railing had to be substituted. The dimensions of both old and new platform with railing can be seen in Figure B.2.

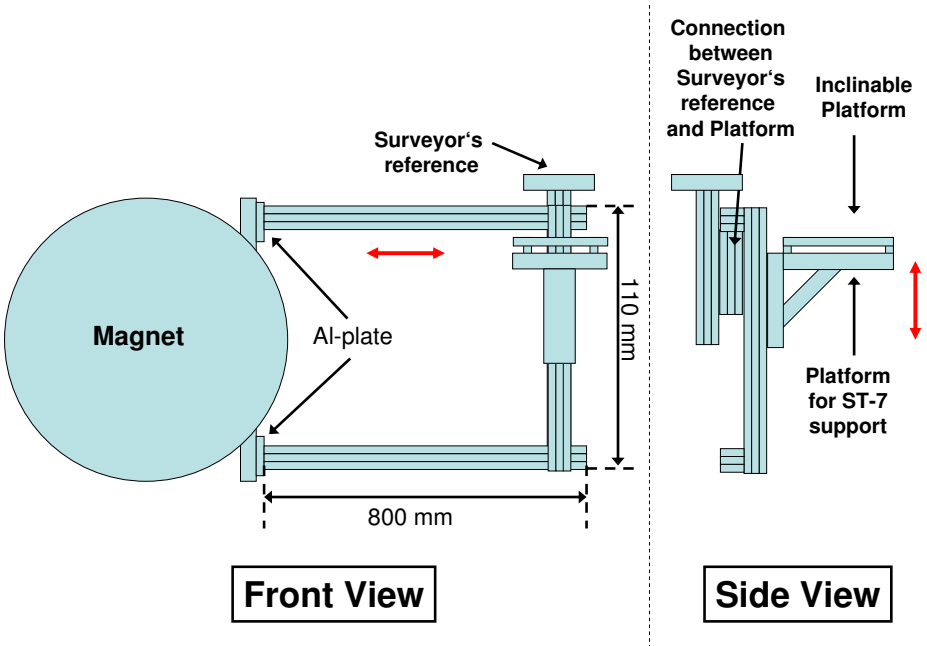

Figure B.1: Carrier and platform constructed using Bosch Rexroth Modular Profile Systems at the mechanical workshop of the Albert-Ludwigs-Universität Freiburg. A console is attached to the vertical profile connecting the two horizontal ones. On this console a tiltable platform is mounted. When the 3D-support is screwed on top of it, the camera can be aligned with the magnet.

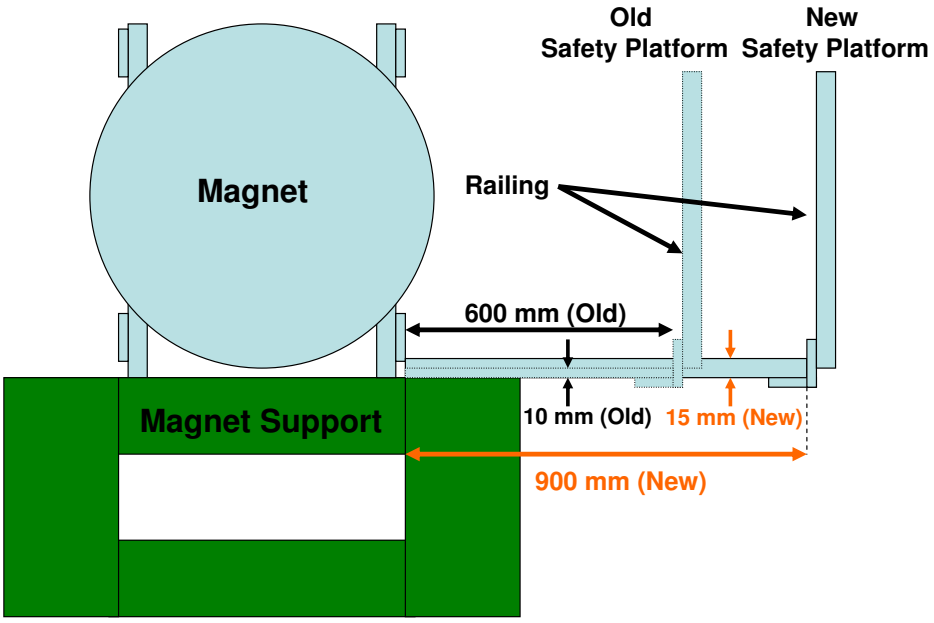

Figure B.2: Old and new safety platform built at the mechanical workshop of the Albert-Ludwigs-Universität Freiburg. It was necessary to change the safety platform, in order to allow the movement of the vertical profile holding the console along the horizontal ones: the old railing was in the way.

Appendix C

Matlab-Scripts

The following *Matlab* routines can be used to process the pictures taken with the ST-7. It is assumed that the images were acquired in the autograb mode, which means that the ST-7 automatically takes consecutive pictures and saves them under a given name attaching the number of the picture. For example, the 128th picture taken is named sun128.tif.

The first program (RotateAll.m) rotates the pictures. This is done because the ST-7 is mounted upside-down and it is just easier for visual crosschecks to have them in the correct orientation. After rotating, the files are saved under their old name with the extension *Rotated* attached to it, e.g. sun128Rotated.tif.
The second routine (Filming.m) is the actual program to extract the observed solar center and its distance from the expected one. It uses the rotated pictures created with RotateAll.m and saves all results (pictures with fit as well as data) to files.
AddData.m reads in all data files and creates an Excel file for spreadsheet analysis. Other formats can be used as well.

RotatedAll.m

```
for i=0:9  %3rd number
   try
   for j=0:9  %2nd number
      try
      for k=0:9  %1st number
         try

         name='E:\Filming\sun';          %%%Source directory for raw pictures
         name=strcat(name,int2str(k));
         name=strcat(name,int2str(j));
         name=strcat(name,int2str(i));
         name=strcat(name,'.tif');
         name;                           %%% Name of source file complete

         RGB = imread(name);             %%% Read sourcefile
         %figure, imshow(RGB);           %%% Show source picture
         B= imrotate(RGB,180);           %%% Rotate source file = output file
         %figure, imshow(B);             %%% Show rotated file

         name2='E:\Filming\sun';         %%%Creating new name
         name2=strcat(name2,int2str(k));
         name2=strcat(name2,int2str(j));
         name2=strcat(name2,int2str(i));
         name2=strcat(name2,'Rotated','.tif');
         name2;

         imwrite(B,name2)                %%% Save rotated file
         catch
            continue
         end
      end
      catch
         continue
      end
   end
   catch
      continue
   end
end
```

Filming.m

```
%%%%%%%%%%%%%%%%%%%%%%%%%%%%%%%%%%%%%%%%%%%%%%%%%%%%%%%%%%%%%%%%%%%%%%%
%%%%%%%%%%%%%%%%%%%    Loop to call all pics   %%%%%%%%%%%%%%%%%%%%%%%
%%%%%%%%%%%%%%%%%%%%%%%%%%%%%%%%%%%%%%%%%%%%%%%%%%%%%%%%%%%%%%%%%%%%%%%
for i=0:9  %3rd number
   try
   for j=0:9  %2nd number
      try
      for k=0:4  %1st number
         try
         name='E:\Filming\sun';          %%% Source directory of rotated pics containing autograbbed
         name=strcat(name,int2str(k));   %%% pictures of type sun001Rotated.tif
         name=strcat(name,int2str(j));
         name=strcat(name,int2str(i));
         name=strcat(name,'Rotated','.tif');
         name;                           %%%name is now the complete name of the source file.
         RGB = imread(name);             %%% Read image and display it
         figure,imshow(RGB);

         %%%%%%%%%%%%%%%%%%%%%%%%%%%%%%%%%%%%%%%%%%%%%%%%%%%%%%%%%%%%%%%%%%%%%%%
         %%%%%%%%%%%%%%%%%%%    Median filter  %%%%%%%%%%%%%%%%%%%%%%%%%%%%%
         %%%%%%%%%%%%%%%%%%%%%%%%%%%%%%%%%%%%%%%%%%%%%%%%%%%%%%%%%%%%%%%%%%%%%%%
         RGB_median = medfilt2(RGB,[3 3]);

         %%%%%%%%%%%%%%%%%%%%%%%%%%%%%%%%%%%%%%%%%%%%%%%%%%%%%%%%%%%%%%%%%%%%%%%
         %%%%%%%%%%%%%%%%%%%  IMOPEN  %%%%%%%%%%%%%%%%%%%%%%%%%%%%%%%%%%%%%%%
         %%%%%%%%%%%%%%%%%%%%%%%%%%%%%%%%%%%%%%%%%%%%%%%%%%%%%%%%%%%%%%%%%%%%%%%
         se = strel('disk',3);           %%%Remove objects having radius less then 3 pixels by opening
                                         %%% it with the disk-shaped structuring element created above.
         RGB_opened = imopen(RGB_median,se);

         %%%%%%%%%%%%%%%%%%%%%%%%%%%%%%%%%%%%%%%%%%%%%%%%%%%%%%%%%%%%%%%%%%%%%%%
         %%%%%%%%%%%%%%%%%%%  IMCLOSE %%%%%%%%%%%%%%%%%%%%%%%%%%%%%%%%%%%%%%%
         %%%%%%%%%%%%%%%%%%%%%%%%%%%%%%%%%%%%%%%%%%%%%%%%%%%%%%%%%%%%%%%%%%%%%%%
         see = strel('disk',2);    %%%Perform a morphological close operation on the image
         RGB_closed = imclose(RGB_opened,see);
         threshold = graythresh(RGB_closed);
         BW = im2bw(RGB_closed,threshold);%%%Convert image to Black and White
         imshow(BW);
         g = imshow(RGB);      %%%Show Original picture
         hold on;              %%%and wait for further additions to it

         %%%%%%%%%%%%%%%%%%%%%%%%%%%%%%%%%%%%%%%%%%%%%%%%%%%%%%%%%%%%%%%%%%%%%%%
         %%%%%%%%%%%%%%%%%% Tracing the Boundary%%%%%%%%%%%%%%%%%%%%%%%%%%%%%
         %%%%%%%%%%%%%%%%%%%%%%%%%%%%%%%%%%%%%%%%%%%%%%%%%%%%%%%%%%%%%%%%%%%%%%%
         for n =1:80

            %%%%%%%%%%%%%%%%%%%%
            %%%Choose column and row to start%%
            %%%%%%%%%%%%%%%%%%%%
            dim = size(BW);      %%%Array dimension
            col = round(dim(2)/2)-60+(n*2);%%%Choose start column
            row = min(find(BW(:,col)));%%%Take minimum of index from array BW whole row for
                                       %%% column col

            connectivity = 8;     %%%Specifies the connectivity to use when tracing the boundary
            num_points  = 100;%%%Maximum number of boundary pixels to extract

            try
            contour1 = bwtraceboundary(BW, [row, col], 'N', connectivity, num_points);
            catch                                    %%% N denotes the starting direction, here: North
               continue
            end
               [...]
            try
            contour8=bwtraceboundary(BW,[row4,col4],'S',connectivity, num_points,'counterclockwise');
            catch
               continue
            end

            contour=[contour1;contour2;contour3;contour4;contour5; contour6;contour7;contour8];
                                                     %%%Clockwise and counterclockwise
            plot(contour(:,2),contour(:,1),'r','LineWidth',1);
```

```
%%%%%%%%%%%%%%%%%%%%%%%%%%%%%%%%%%%%%%%%%%%%%%%%
%%%%%%%%%%%%%%     Median of center of circle     %%%%%%%%%%%%%%%%%
%%%%%%%%%%%%%%%%%%%%%%%%%%%%%%%%%%%%%%%%%%%%%%%%

%%%%%%%%%%%%
%%%x coordinate %%
%%%%%%%%%%%%
xcenter2=[];               %%%Empty new array
ende=size(xcenter);    %%%Dimension of xcenter
   for m=1:ende(2)
      if xcenter(1,m)~=0
      xcenter2(size(xcenter2,2)+1)=xcenter(m);
      end
   end
xcenter=xcenter2;
sx1 =std(xcenter2);     %%%Standard deviation
sx2=1.253*sx1;          %%%Median error
sx3=sx2*9.27/3600;    %%%Transformation from pixels into degrees
mxcenter=median(xcenter2);   %%%Median xcenter

%%%%%%%%%%%%
%%% y coordinate %%
%%%%%%%%%%%%
ycenter2=[];               %%%Empty new array
ende=size(ycenter);    %%%Dimension of xcenter
   for m=1:ende(2)
      if ycenter(1,m)~=0
      ycenter2(size(ycenter2,2)+1)=ycenter(m);
      end
   end
ycenter=ycenter2;
sy1 =std(ycenter2);     %%%Standard deviation
sy2=1.253*sy1;          %%%Median error
sy3=sy2*9.27/3600;    %%%Transformation from pixels into degrees
mycenter=median(ycenter2);   %%%Median xcenter

%%%%%%%%%%%%%%%%%%%%%%%%%%%%%%%%%%%%%%%%%%%%%%%%
%%%%%%  Distance between observed Sun center and reference (pixel) %%%%%%%%%
%%%%%%%%%%%%%%%%%%%%%%%%%%%%%%%%%%%%%%%%%%%%%%%%
referencex=246;                        %%% x coordinate from alignment picture
referencey=285;                        %%% y coordinate from alignment picture
mdistancex=mxcenter-referencex;            %%%Distance of observed center
mdistancey=referencey-mycenter;            %%%and reference point in x, y

%%%%%%%%%%%%%%%%%%%%%%%%%%%%%%%%%%%%%%%%%%%%%%%%
%%%%%%% Distance between observed Sun center and reference (degree) %%%%%%%%
%%%%%%%%%%%%%%%%%%%%%%%%%%%%%%%%%%%%%%%%%%%%%%%%
distancedegreex=9.27*mdistancex/3600;  %%%9.27 is the FoV of one pixel of the ST7 in arcsec
distancedegreey=9.27*mdistancey/3600;  %%% and the factor 1/3600 for conversion to degree

%%%%%%%%%%%%%%%%%%%%%%%%%%%%%%%%%%%%%%%%%%%%%%%%
%%%%%%%%%%%% Plotting the Median Circle and its center %%%%%%%%%%%%%%
%%%%%%%%%%%%%%%%%%%%%%%%%%%%%%%%%%%%%%%%%%%%%%%%
figure,imshow(RGB)
hold on;
plot(mxcenter,mycenter,'mx','LineWidth',2);              %%%Display the Median calculated center
theta = 0:0.01:2*pi;                                                %%%Plot the entire circle

%%%Use parametric representation of the circle to obtain coordinates of points on the circle:
Xfit = mradius*cos(theta) + mxcenter;
Yfit = mradius*sin(theta) + mycenter;
plot(Xfit, Yfit,'m','LineWidth',1);

%%%Messages to plot in Image
message1 = sprintf('The radius is %2.0f pixels.', mradius);
message2 = sprintf('The x coordinate of center is %2.0f pixels.', mxcenter);
message3 = sprintf('The y coordinate of center is  %2.0f pixels.', mycenter);
message4 = sprintf('The distance in x of expected center and observed center is %2.0f pixels,
    i.e. %2.3f degree.', mdistancex, distancedegreex);
message5 = sprintf('The distance in y of expected center and observed center is %2.0f pixels,
    i.e. %2.3f degree.', mdistancey, distancedegreey);
text(15,15,message1,'Color','y','FontWeight','bold','FontSize',8);
text(15,30,message2,'Color','y','FontWeight','bold','FontSize',8);
text(15,45,message3,'Color','y','FontWeight','bold','FontSize',8);
text(15,60,message4,'Color','y','FontWeight','bold','FontSize',8);
text(15,75,message5,'Color','y','FontWeight','bold','FontSize',8);
```

```
   %%%%%%%%%%%%%%%%%%%%%%%%%%%%%%%%%%%%%%%%%%%%%%%
   %%%%%%%%%%%%%%     Fit the Image  %%%%%%%%%%%%%%%%%%%%%%%
   %%%%%%%%%%%%%%%%%%%%%%%%%%%%%%%%%%%%%%%%%%%%%%%
   x = contour(:,2);
   y = contour(:,1);
   abc=[x y ones(length(x),1)]\[-(x.^2+y.^2)];%%%Solve for
                                              %%%parameters
                                              %%%a, b, and c
   a = abc(1); b = abc(2); c = abc(3);

   %%%%%%%%%%%%%%%%%%%%%%%%%%%%%%
     %%% Calculate the location of the center and the radius %
   %%%%%%%%%%%%%%%%%%%%%%%%%%%%%%
   xc = -a/2;
   yc = -b/2;
   radius  =  sqrt((xc^2+yc^2)-c);
   try
      if (radius > 100)& ~(radius > 106)       %%%Excluding too small and too large radii
         format short
         r(n) = [radius];
         xcenter(n) = [xc];
         ycenter(n) = [yc];
      elseif (radius <= 100)
       error('Radius unreasonable (too small)!')
      elseif (radius >= 106)
       error('Radius unreasonable (too large)!')
      end
   catch
      continue
   end
end

%%%%%%%%%%%%%%%%%%%%%%%%%%%%%%%%%%%%%%%%%%%%%%%%
%%%%%%%%%% Save TracePic as TIF, EPS and JPG %%%%%%%%%%%%%%%%%%
%%%%%%%%%%%%%%%%%%%%%%%%%%%%%%%%%%%%%%%%%%%%%%%%
name02='E:\Filming\sun';           %%%Set name for traced output file as tif
name02=strcat(name02,int2str(k));
name02=strcat(name02,int2str(j));
name02=strcat(name02,int2str(i));
name02=strcat(name02,'EditedRotatedTrace.tif');
name02;
saveas(gcf,name02,'tif');
name03='E:\Filming\sun';           %%%Set name for traced output file as eps
name03=strcat(name03,int2str(k));
name03=strcat(name03,int2str(j));
name03=strcat(name03,int2str(i));
name03=strcat(name03,'EditedRotatedTrace.eps');
name03;
saveas(gcf,name03,'eps');
name04='E:\Filming\sun';           %%%Set name for traced output file as jpg
name04=strcat(name04,int2str(k));
name04=strcat(name04,int2str(j));
name04=strcat(name04,int2str(i));
name04=strcat(name04,'EditedRotatedTrace.jpg');
name04;
saveas(gcf,name04,'jpg');

%%%%%%%%%%%%%%%%%%%%%%%%%%%%%%%%%%%%%%%%%%%%%%%%
%%%%%%%%%%%%%  Median of Radius %%%%%%%%%%%%%%%%%%%%%%%%
%%%%%%%%%%%%%%%%%%%%%%%%%%%%%%%%%%%%%%%%%%%%%%%%
r2=[];                                %%%Empty new array
ende=size(r);                         %%%Dimension of radius
for m=1:ende(2)
      if r(1,m)~=0
      r2(size(r2,2)+1)=r(m);
      end
end
r=r2;
mradius=median(r2);   %%%Median: When there is an odd number of numbers, the median
                       %%% is simply the middle number. When there is an even number
                       %%% of numbers, the median is the mean of the two middle numbers
```

```
        %%%Save FitPic as TIF, EPS and JPG
        name2='E:\Filming\sun';%%%Set name for fitted output file as tif
        name2=strcat(name2,int2str(k));
        name2=strcat(name2,int2str(j));
        name2=strcat(name2,int2str(i));
        name2=strcat(name2,'EditedRotatedFit.tif');
        name2;
        saveas(gcf,name2,'tif');
        name3='E:\Filming\sun';%%%Set name for fitted output file as eps
        name3=strcat(name3,int2str(k));
        name3=strcat(name3,int2str(j));
        name3=strcat(name3,int2str(i));
        name3=strcat(name3,'EditedRotatedFit.eps');
        name3;
        saveas(gcf,name3,'eps');
        name4='E:\Filming\sun';%%%Set name for fitted output file as jpg
        name4=strcat(name4,int2str(k));
        name4=strcat(name4,int2str(j));
        name4=strcat(name4,int2str(i));
        name4=strcat(name4,'EditedRotatedFit.jpg');
        name4;
        saveas(gcf,name4,'jpg');

        %%%Save Radius and Center, distances and errors
        name5='E:\Filming\sun';%%%Set name for data output file
        name5=strcat(name5,int2str(k));
        name5=strcat(name5,int2str(j));
        name5=strcat(name5,int2str(i));
        name5=strcat(name5,'DataRotated');
        name5;
        save(name5,'mradius','mxcenter','mycenter','mdistancex','mdistancey',
        'distancedegreex','distancedegreey','sx3','sy3','-ASCII')
        catch
            continue
        end
    end
    catch
        continue
    end
  end
  catch
    continue
  end
end
```

AddData.m

```
b=[];
for i=0:9  %3rd number                    %%%  Iteration over all Pics
  try
  for j=0:9  %2nd number
    try
    for k=0:5  %1st number
      try

        name1='E:\Filming\sun';%%% Set name for Data file to be read
        name1=strcat(name1,int2str(k));
        name1=strcat(name1,int2str(j));
        name1=strcat(name1,int2str(i));
        name1=strcat(name1,'DataRotated');
        name1;

        fid = fopen(name1);     %%%Open File to be read
        C = textscan(fid, '%f %f %f %f %f %f %f');
        C{1};
        c = C{1}';          %%%Transpone to 1 line with three columns


        B=[b;c];      %%%Definition of B: Take Matrix b and add the vector c (=line)
        b=B;          %%%Set new b as B such that in the next iteration a new line c is added

        fclose(fid);

        catch
          continue
        end
    end
    catch
      continue
    end
  end
  catch
    continue
  end
end
B
xlswrite('E:\Filming\sunRotated, B)       %%%Write B to xls-file
```

List of Figures

List of Tables

Bibliography

[1] J. H. Christenson, J. W. Cronin, V. L. Fitch, and R. Turlay, *Evidence for the 2 pi Decay of the K_2^0 Meson*, Phys. Rev. Lett. **13** (1964) 138-140.

[2] U. von Rauchhaupt, *Nobelpreis:"Meine Instinkte sind mathematisch"*, Frankfurter Allgemeine Sonntagszeitung **41** (10.10.2004) 67.

[3] T. Dafni, *A Search for Solar Axions with the MICROMEGAS Detector in CAST*, PhD Thesis, Technische Universität Darmstadt, Germany, (2005).

[4] T.-P. Cheng and L.-F. Li, *Gauge theory of elementary particle physics*, Oxford University Press, Oxford (2000).

[5] D. S. Kinion, *First Results from a Multiple-Microwave-Cavity Search for Dark-Matter Axions*, PhD Thesis, University of California, Davis, (2001).

[6] B. Povh, K. Rith, C. Scholz and F. Zetsche, *Teilchen und Kerne*, Springer-Verlag, Berlin (1997).

[7] C. Quigg, *Gauge Theories of the Strong, Weak, and Electromagnetic Interactions*, Frontiers in Physics, Vol. 56, Addison-Wesley Publishing Company, Reading, Massachusetts (1983).

[8] S. Eidelman *et al.*, *Review of Particle Physics. Particle Data Group*, Phys. Lett. B **592** (2004) 1.

[9] G. t' Hooft, *Symmetry Breaking through Bell-Jackiw Anomalies*, Phys. Rev. Lett. **37** (1976) 8.

[10] G. t' Hooft, *Computation Of The Quantum Effects Due To A Four-Dimensional Pseudoparticle*, Phys. Rev. D **14** (1976) 3432 [Erratum-ibid. D **18** (1978) 2199].

[11] H. V. Klapdor-Kleingrothaus and K. Zuber, *Particle Astrophysics*, Institute of Physics Publishing, Bristol and Philadelphia (1997).

[12] R. D. Peccei, *CP-Violation Advanced Series in High Energy Physics*, Vol 3 ed, C. Jarlskog, World Scientific, Singapore (1989).

[13] J. E. Kim, *Light Pseudoscalars, Particle Physics and Cosmology*, Phys. Rep.**150** (1987) 1.

[14] R. Crewther *et al.*, *Chiral Estimate Of The Electric Dipole Moment Of The Neutron In Quantum Chromodynamics*, Phys. Lett. B **88** (1979) 123.

[15] N. F. Ramsey, *Electric Dipole Moment Of The Neutron*, Ann. Rev. Nucl. Part. Phys. **40** (1990) 1.

[16] J. M. Pendlebury, *Fundamental Physics With Ultracold Neutrons*, Ann. Rev. Nucl. Part. Phys. **43** (1993) 687.

[17] R. D. Peccei and H. R. Quinn, *CP Conservation In The Presence Of Pseudoparticles*, Phys. Rev. Lett. **38** (1977) 1440.

[18] S. Weinberg, *A New Light Boson?*, Phys. Rev. Lett. **40** (1978) 223.

[19] F. Wilczek, *Problem Of Strong P And T Invariance In The Presence Of Instantons*, Phys. Rev. Lett. **40** (1978) 279.

[20] F. Wilczek, *Asymptotic Freedom: From Paradox To Paradigm*, [arXiv:hep-ph/0502113].

[21] R. N. Mohapatra and A. Rašin , *Simple Supersymmetric Solution to the Strong CP Problem*, Phys. Rev. Lett. **76** (1996) 3490.

[22] G. G. Raffelt, *Stars as Laboratories for Fundamental Physics*, University of Chicago Press, Chicago/London (1996).

[23] W. A. Bardeen and S.-H. H. Tye, *Current Algebra Applied To Properties Of The Light Higgs Boson*, Phys. Lett. B **74** (1978) 229.

[24] J. Gasser and H. Leutwyler, *Quark Masses*, Phys. Rep. **87** (1982) 77.

[25] K. Böcker, *Impact of Hadronic Axions on Black Hole Accretion Discs and Neutron Stars*, Diplomarbeit, München (1999).

[26] H. Leutwyler, *The ratios of the light quark masses*, Phys. Lett. B **378** (1996) 313.

[27] M. Srednicki, *Axion Couplings to Matter. I. CP-conserving parts*, Nucl. Phys. B **260** (1985) 689.

[28] D. B. Kaplan, *Opening the Axion Window*, Nucl. Phys. B **260** (1985) 215.

[29] J. Ellis and M. Karliner, *Determination of α_s and the nucleon spin decomposition unsing recent polarized structure function data*, Phys. Lett. B, **341** (1995) 397.

[30] J. E. Kim, *Weak Interaction Singlet and CP Invariance*, Phys. Rev. Lett. **43** (1979) 103.

[31] M. A. Shifman, A. I. Vainshtein, V. I. Zakharov, *Can Confinement Ensure Natural CP Invariance of Strong Interactions?*, Nucl. Phys. B **166** (1980) 493.

[32] A. R. Zhitnitskiĭ, *On Possible Suppression Of The Axion Hadron Interactions.*, Sov. J. Nucl. Phys. **31** (1980) 260.

[33] M. Dine, W Fischler, M. Srednicki, *A Simple Solution To The Strong CP Problem With A Harmless Axion*, Phys. Lett. B **104** (1981) 199.

[34] M. S. Turner, *Windows on the Axion*, Phys. Rep. **197** (1990) 67.

[35] M. S. Turner, *Early-Universe Thermal Production of Not-So-Invisible Axions*, Phys. Rev. Lett. **59** (1987) 2489, [Errata-ibid. **60** (1988) 1101].

[36] J. Preskill, M. Wise, and F. Wilczek, *Cosmology of the Invisible Axion*, Phys. Lett. B **120** (1983) 127.

[37] L. Abbott and P. Sikivie, *A Cosmological Bound On The Invisible Axion*, Phys. Lett. B **120** (1983) 133.

[38] M. Dine and W. Fischler, *The Not-So-Harmless Axion*, Phys. Lett. B **120** (1983) 137.

[39] R. L. Davis, *Cosmic Axions from Cosmic Strings*, Phys. Lett. B **180** (1986) 225.

[40] Private Communication with Dr. G. Raffelt, November 2005.

[41] H.-T. Janka *et al.*, *Nucleon Spin Fluctuations and the Supernova Emission of Neutrinos and Axions*, Phys. Rev. Lett. **76** (1996) 2621.

[42] G. Raffelt, *Axions*, Space Science Rev. **100** (2002) 153.

[43] M. S. Turner, *Axions from SN1987A*, Phys. Rev. Lett. **60** (1988) 1797.

[44] A. Burrows *et al.*, *Axions and SN 1987A: Axion trapping*, Phys. Rev. D **42** (1990) 3297.

[45] J. Engel *et al.*, *Emission and detectability of hadronic axions from SN 1987A*, Phys. Rev. Lett. **65** (1990) 960.

[46] M. S. Turner and F. Wilczek, *Inflationary Axion Cosmology*, Phys. Rev. Lett. **66** (1991) 5.

[47] E. P. S. Shellard and R. A. Battye, *Cosmic Axions*, (1998) [arXiv:astro-ph/9802216].

[48] R. A. Battye and E. P. S. Shellard, *Axion String Constraints*, Phys. Rev. Lett. **73** (1994) 2954 [Erratum ibid. **76** (1996) 2203].

[49] D. Harari and P. Sikivie, *On the Evolution of Global Strings in the Early Universe*, Phys. Lett. B **195** (1987) 361.

[50] G. Raffelt, *Particle Physics from Stars*, (1999) [arXiv:hep-ph/9903472].

[51] H. Cheng, *The strong CP problem revisited*, Phys. Rep **158** (1988) 1.

[52] P. Sikivie, *Experimental Tests of the "invisible" Axion*, Phys. Rev. Lett. **51** (1983) 1415 [Erratum ibid. **52** (1984) 695].

[53] W. Wuensch *et al.*, *Results of a laboratory search for cosmic axions and other weakly coupled light particles*, Phys. Rev. D **40** (1989) 3153.

[54] C. Hagmann *et al.*, *Results from a search for cosmic axions*, Phys. Rev. D **42** (1990) 1297.

[55] C. Hagmann *et al.*, *Results from a High-Sensitivity Search for Cosmic Axions*, Phys. Rev. Lett. **80** (1998) 2043.

[56] S. J. Asztalos *et al.*, *Improved rf cavity search for halo axions*, Phys. Rev. D **69** (2004) 011101.

[57] M. Mück, J. B. Kycia, and J. Clarke, *Superconducting Quantum Interference Device as a Near-Quantum-Limited-Amplifier at* 0.5 *GHz*, Appl. Phys. Lett. **78** (2001) 967.

[58] K. Yamamoto *et al.*, *The Rydberg atom cavity axion search*, Invited talk presented at the Dark2000, Heidelberg, Germany,10-15 July, (2000), [arXiv:hep-ex/0101200].

[59] M. T. Ressell, *Limits to the radiative decay of the axion*, Phys. Rev. D **44** (1991) 3001.

[60] M. A. Bershady, M. T. Ressell, and M. S. Turner, *Telescope search for a 3-eV to 8-eV axion*, Phys. Rev. Lett. **66** (1991) 1398.

[61] B. D. Blout *et al.*, *A radio telescope search for axions*, Astrophys. J. **546** (2001) 825.

[62] K. Zioutas, *Die Suche nach Solaren Axionen mit CAST*, Seminar Talk, Albert-Ludwigs-Universität Freiburg, Germany (2004).

[63] K. van Bibber *et al.*, *Proposed experiment to produce and detect light pseudoscalars*, Phys. Rev. Lett. **59** (1987) 759.

[64] R. Cameron *et al.*, *Search for nearly massless, weakly coupled particles by optical techniques*, Phys. Rev. D **47** (1993) 3707.

[65] F. Hoogeveen and T. Ziegenhagen, *Production and detection of light bosons using optical resonators*, Nucl. Phys. B **358** (1991) 3.

[66] G. Ruoso *et al.*, *Search for photon regeneration in a magnetic field*, Z. Phys. **56** (1992) 505.

[67] Y. Semertzidis *et al.*, *Limits on the production of light scalar and pseudoscalar particles*, Phys. Rev. Lett. **64** (1990) 2988.

[68] K. Zioutas *et al.*, *A Decommissioned LHC Model Magnet as an Axion Telescop*, Nucl. Instr. a. Meth in Phys. A **425** (1999) 480.

[69] K. Zioutas *et al.*, *First Results from the CERN Axion Solar Telescope (CAST)*, Phys. Rev. Lett. **94** (2005) 121301, [arXiv:hep-ex/0411033].

[70] G. G. Raffelt, *Axions: Recent Searches and New Limits*, (2005), [arXiv:hep-ph/0504152].

[71] E. A. Paschos and K. Zioutas, *A Proposal for Solar Axion Detection via Bragg Scattering*, Phys. Lett. B **323** (1994) 367.

[72] R. J. Creswick *et al.*, *Theory of the Direct Detection of Solar Axions by Coherent Primakoff Conversion in germanium Detectors*, Phys. Lett. B **427** (1998) 235, [arXiv:hep-ph/9708210].

[73] F. T. Avignone III *et al.* [SOLAX Collaboration], *Experimental Search for Solar Axions via Coherent Primakoff Conversion in a Germanium Spectrometer*, Phys. Rev. Lett. **81** (1998) 5068, [arXiv:astro-ph/9708008].

[74] A. Morales *et al.* [COSME Collaboration], *Particle Dark Matter and Solar Axion Searches with a Small Germanium Detector at the Canfranc Underground Laboratory*, Astropart. Phys. **16** (2002) 325, [arXiv:hep-ex/0101037].

[75] R. Bernabei *et al.*, *Search for Solar Axions by Primakoff Effect in NaI Crystals*, Phys. Lett. B **515** (2001) 6.

[76] S. Cebrián *et al.*, *Prospects of Solar Axion Searches with Crystal Detectors*, Astropart. Phys. **10** (1999) 397, [arXiv:astro-ph/9811359].

[77] K. Van Bibber, P. M. McIntyre, D. E. Morris, and G. G. Raffelt, *Design for a Practical Laboratory Detector for Solar Axions*, Phys. Rev. D. **39** (1989) 2089.

[78] D. M. Lazarus *et al.*, *Search for Solar Axions*, Phys. Rev. Lett. **69** (1992) 2333.

[79] S. Moriyama *et al.*, *Direct Search for Solar Axions by Using Strong Magnetic Field and X-Ray Detectors*, Phys. Lett. B **434** (1998) 147, [arXiv:hep-ex/9805026].

[80] I. G. Irastorza, *Direct Searches for Dark Matter Particles: WIMPS and Axions*, (2005) [arXiv:hep-ex/0509004].

[81] H. Primakoff, *Photo-Production of Neutral Mesons in Nuclear Electric Fields and the Mean Life of Neutral Meson*, Phys. Rev. **81** (1951) 899.

[82] L. Di Lella, A. Pilaftsis, G. Raffelt, and K. Zioutas, *Search for solar Kaluza-Klein axions in theories of low-scale quantum gravity*, Phys. Rev. D **62** (1989) 125011.

[83] J. N. Bahcall, W. F. Huebner, S. H. Lubow, P. D. Parker, and R. K. Ulrich, *Standard Solar Models and the Uncertainties in Predicted Capture Rates of Solar Neutrinos*, Rev. Mod. Phys. **54** (1982) 767.

[84] J. N. Bahcall and M. H. Pinsonneault, *What do we (not) know theoretically about solar neutrino fluxes?*, Phys. Rev. Lett. **92** (2004) 121301, [arXiv:astro-ph/0402114].

[85] Figure courtesy of Donghwa Kang.

[86] P. D. Serpico and G. G. Raffelt, *New Calculations of Solar Axion Flux*, Internal CAST Report (12 January 2005).

[87] Private communication with Donghwa Kang, Freiburg, November 2005.

[88] G. G. Raffelt and L. Stodolsky, *Mixing of the Photon with Low-Mass Particles*, Phys. Rev. D **37** (1988) 1237.

[89] Figure courtesy of Dr. Biljana Lakić.

[90] NOVAS (Naval Observatory Vector Astrometry Subroutines), http://www.usno.navy.mil/, http://aa.usno.navy.mil/software/

[91] JPL, (Jet Propulsion Laboratory's HORIZONS System), http://ssd.jpl.nasa.gov/horizons.html, see also: http://ssd.jpl.nasa.gov/.

[92] O. Montenbruck, *Grundlagen der Epemeridenrechnung*, Elsevier GmbH, Spektrum Akademischer Verlag, Heidelberg, Germany, 7th edition, (2005). Also available in English: O. Montenbruck, *Practical Ephemeris Calculations*, Springer-Verlag, Heidelberg, Germany, (1989).

[93] http://www.analemma.com/

[94] Figure courtesy of Thomas Papaevangelou.

[95] M. Bona *et al.*, *Performance of the first CERN - INFN* 10 *m long superconducting dipole prototype for the LHC*, CERN-AT-94-26-MA, 4th European Particle Accelerator Conference (EPAC 94), London, England, (27 Jun - 1 Jul 1994).

[96] K. Barth *et al.*, *Commissioning and first operation of the cryogenics for the CERN Axion Solar Telescope (CAST)*, AIP Conference Proceeding **710** (2004) 168.

[97] J. I. Collar, 5th CAST Collaboration Meeting, CERN, Geneva, Switzerland, March 2001.

[98] J. I. Collar, 11th CAST Collaboration Meeting, CERN, Geneva, Switzerland, July 2002.

[99] J. I. Collar, 12th CAST Collaboration Meeting, Halkidiki, Greece, September 2002.

[100] Figure courtesy of the TPC detector group, Universidad de Zaragoza, Spain.

[101] S. Andriamonje *et al.*, *A Micromegas detector for the CAST experiment*, NIM A **518** (2004) 252.

[102] J. Altmann *et al.*, *X-Ray Optics, Instruments, and Mission*, (1998), Proceedings of SPIE, edited by R. B. Hoover and A. B. Walker, (1999), p.350;
J. W. Egle *et al.*,*ibid.*, p.359; P. Friedrich *et al.*, *ibid.*, p.369.

[103] P. Friedrich *et al.*, *X-Ray Optics, Instruments, and Mission*, (1998), Proceedings of SPIE edited by R. B. Hoover and A. B. Walker, (1999), p.369.

[104] L. Strüder *et al.*, *The European Photon Imaging Camera on XXM-Newton: The pn-CCD camera*, Astronomy and Astrophysics **365**, L18, (2001) DOI:10.1051/0004-6361:20000066.

[105] J. W. Egle, J. Altmann, and H. Schwarz, *X-Ray Optics, Instruments, and Mission II*, (1999), Proceedings of SPIE 3766, edited by R. B. Hoover and A. B. Walker, (1999).

[106] Private communication with Dr. Markus Kuster in November 2005.

[107] C. A. Eleftheriadis *et al.*, *Simulation of the X-Ray Telescope in the CAST Experiment at CERN*, 8th CAST Collaboration Meeting, Darmstadt, Germany, December 2001.

[108] H. Wolter, *Mirror systems with glancing incidence on image-producing optics for X-rays*, Ann. Phys. Leipzig **10** (1952) 94.

[109] M. Kuster *et al.*, *The X-Ray Mirror Telescope and the pn-CCD Detector of CAST*, Proceedings of SPIE 5500, 139, (2004).

[110] Figure courtesy of David W. Miller, University of Chicago, USA.

[111] MeteoSwiss, http://www.meteoswiss.ch/en/Forecasts/Observations/IndexObservations.shtml

[112] http://cast.web.cern.ch/CAST/edited_tracking.mov

[113] Private communication with Dr. Biljana Lakić.

[114] Santa Barbara Instrument Group, *Operating Manual CCD Camera Models ST-7XE, ST-8XE, ST-9XE, ST-10XE, ST-10XME and ST-2000XM With High Speed USB Interface*, http://www.sbig.com/pdffiles/USBmanRev14.pdf. Further information can be found on http://www.sbig.com.

[115] Figure courtesy of Dr. Markus Kuster.

[116] ftp://ssd.jpl.nasa.gov/pub/ssd/Horizons_doc.pdf, 44.

[117] http://www.boschrexroth.com

[118] http://www.mathworks.com/products/demos/image/radius_tape/ipexradius.html.

[119] M. Kuster, *Telescope Alignment*, 21th CAST Collaboration Meeting, CERN, Geneva, Switzerland, May 2004.

[120] Private communication with Dr. Markus Kuster, Geneva, September 2005.

[121] M. Kuster, *Status pn-CCD*, 26th CAST Collaboration Meeting, CERN, Geneva, Switzerland, September 2005.

[122] http://www.sbig.com/sbwhtmls/online.htm, see also ST-7 Manual at http://www.sbig.com/sbwhtmls/softpage.htm

Acknowledgements

The last 18 months have been an incredible experience and first of all, I would like to thank Professor Dr. Kay Königsmann for giving me the opportunity to join his group and the CAST experiment by supporting my work on this diploma thesis.
I am sincerely indebted to Dr. Jürgen Franz, who acted as my advisor and was always there to answer all my questions and help me in solving whichever problems I came across. I am indeed grateful for the opportunity to learn from him and for the trust he had in me.

For discussions, suggestions and support, the whole Freiburg team should be rewarded. Thanks to you all for the help and also for the fun we had: Dr. Horst Fischer, Dr. Fritz-Herbert Heinsius, Dr. Andreas Mutter, Dr. Frank Nerling, Dr. Christian Schill, Dr. Eric Weise, Sonja Hedicke, Florian Hermann, Martin Frhr. von Hodenberg, Donghee Kang, Oliver Kilias, Dominik Setter, Sebastian Trippel, and Anselm Vossen. Special thanks go to Donghwa Kang for always patiently answering all of my questions.
Thanks to Khalil Rehmani, Gisela Mössner and especially Rainer Fastner for the support at Freiburg and CERN. I also deeply appreciate the work of the mechanic workshop team in Freiburg, especially Gerhard Heine did a fantastic job. For installations at CERN together with Rainer Fastner, I would like to thank Ralf Schlegel.
Very helpful were Christoph Keller, who got me started with Matlab, and everybody proof-reading this thesis. Special thanks go to Andreas Hüther.

When it comes to CAST, I want to thank Professor Dr. Konstantin Zioutas for his support at CERN. I am deeply indebted to Thomas Papaevangelou and to Dr. Theopisti Dafni, whose PhD thesis was so very helpful. Thanks to Martyn Davenport, Jean-Noël Joux and his team from the EST division at CERN, Dr. Markus Kuster, Dr. Biljana Lakić, Cristina Rosso, Jaime Ruz Armendáriz and the whole CAST collaboration for their help and support. Special thanks go to everybody who got up early for the solar filming. I honestly appreciated this and by no means took it for granted. But you must admit that it was also some fun sometimes, wasn't it?

Thanks to the friends, who kept an eye on me and my feet on the ground, cared for me and always managed to put a smile on my face: Kathrin Reiter, Stefan Meckler, Florian Clement, Martina Reiff, Marlene Mahn and Steffen Weber.

I am indebted to my father, Manfred Vogel, his wife Roswita and to my brothers and

sisters Konstantin, Sophia and Maximilian. Vielen Dank meiner lieben Oma Ida Kramer.

Thank you Jaime for showing me how important it is to never say never. It may change lives. At least it changed mine.

I feel very lucky and indeed proud to have been accompanied and supported in all situations of my life by my family and therefore my sincerest appreciation and my utmost respect belong to my mother Veronika Straub, her husband Franz-Josef Straub and my dear brother Mario Straub.
I would not be who I am without my family and my friends. My love and gratitude belongs to them.

Erklärung

Diese Arbeit ist von mir selbstständig verfasst worden, und ich habe keine anderen als die angegebenen Quellen und Hilfsmittel benutzt.

Julia Vogel, Dezember 2005